Optimisation of vessel-selective magnetic resonance perfusion imaging and angiography



Eleanor Berry

Jesus College

University of Oxford

A thesis submitted for the degree of

Doctor of Philosophy in Clinical Neurosciences

Sunday 7^{th} August 2016

Acknowledgements

I would firstly like to thank my supervisors, Professor Peter Jezzard and Dr Thomas Okell, for their unfailing support. They have always helped me produce the best work possible. In particular a huge thanks goes to Tom. Without his help, guidance and general unwavering patience with questions, drafts and more questions there just wouldn't have been a thesis.

I am very grateful for the generous funding received from the Engineering and Physical Sciences Research Council that supported me through my DPhil in the first instance. I would then like to thank both the Nuffield Department for Clinical Neurosciences and Jesus College Oxford for the financial support I received to make it through the final few months. Funding from The Dunhill Medical Trust and the Royal Academy of Engineering also supported the work in this thesis.

Thanks goes to my family for having me to stay while writing the bulk of this thesis, for keeping me as relaxed as possible and appropriately caffeinated. I would also like to mention the whole fMRIB Physics group for helping by being subjects, responsible extra people in the scan room, providing advice on presentations and just great lunch chat. I am particularly grateful to Dr James Meakin for providing multi-phase PCASL data used in this thesis.

Finally, my DPhil experience would have been much the poorer without the fMRIB Physics girls I started with. I'm not sure I can imagine the next stage of my work life without you nearby, but I hope we can have many a reunion to reminisce over the glory days of our gingerbread scanner.

Abstract

The diagnosis and treatment of cerebrovascular disease, such as stroke and vascular lesions in the brain, requires knowledge of the status of brain tissue and cerebral arteries. Perfusion imaging and angiography offer information on blood flow to the tissue and through the brain-feeding arteries. A variety of imaging modalities exist to assess brain haemodynamics, including measures of cerebral blood flow and other parameters, however many of these are invasive and/or involve the use of contrast agents toxic to certain patient populations.

One non-invasive magnetic resonance imaging alternative for perfusion imaging and angiography, which also provides vessel specific blood flow information, is vessel-encoded pseudocontinuous arterial spin labelling (VEPCASL). VEPCASL uses the blood as an endogenous tracer and can magnetically label the blood from different arteries of interest. The combination of VEPCASL with different imaging strategies can provide a map of the vascular perfusion territories in the brain, or dynamic information on blood flow through the cerebral arteries.

The work in this thesis seeks to optimise and develop the encoding process of VEPCASL and accompanying angiographic readouts. Firstly, a rapid and automated method for calculating a minimal number of signal-to-noise ratio (SNR) efficient encodings, for any number and arrangement of vessels, was developed. Its use resulted in improved SNR in perfusion territories fed by more complicated vessel arrangements in the labelling plane. The labelling efficiency of VEPCASL, and its non-vessel-selective equivalent, PCASL, is affected by the presence of magnetic field inhomogeneities in the labelling

plane. Consequently, a correction for phase offsets was introduced into the calculation of the optimised encodings. These encodings enabled the recovery of SNR in perfusion territories for PCASL and VEPCASL when phase offsets were present at the labelled arteries.

As current VEPCASL angiography methods are relatively slow to acquire, an accelerated readout was developed to acquire two-dimensional vessel-selective dynamic angiograms in approximately one minute. A radial k-space trajectory was found to offer the best vessel definition and SNR. Three-dimensional (3D) angiograms provide the most detailed view of the cerebral vasculature for use in diagnosis and treatment of cerebrovascular disease. A 3D radial readout was optimised to acquire vessel-selective dynamic angiograms. These angiograms offer information on the structure of the vascular tree and how it is fed by the major arteries in the neck.

The techniques developed here aim to increase the clinical viability and applicability of VEPCASL perfusion imaging and angiography. It is hoped that the techniques herein could be used in patient populations to add to and improve the diagnostic information available.

Contents

1 Introduction **1**

1.1 Motivation 1

1.1.1 Using perfusion imaging and angiography to detect and treat cerebrovascular disease 1

1.1.2 The challenges of imaging the cerebral vasculature and its perfusion territories 3

1.2 Thesis outline 4

2 Background **6**

2.1 Principles of magnetic resonance imaging 6

2.1.1 Nuclear magnetisation 6

2.1.2 Basis of MRI: gradients and k-space 9

2.1.3 The Bloch equation in an effective field 12

2.2 Arterial spin labelling 12

2.2.1 Pulsed arterial spin labelling 14

2.2.2 Continuous arterial spin labelling 15

2.2.3 Pseudocontinuous arterial spin labelling 15

2.2.4 Vessel-encoded pseudocontinuous arterial spin labelling 17

2.3 ASL perfusion imaging acquisition strategies 19

2.4 ASL angiography acquisition strategies 20

2.4.1 Single line methods 21

2.4.2 k-space trajectories 22

2.4.3 Non-Cartesian trajectory reconstruction strategies 25

2.5 Summary 27

3 Current methods in cerebral perfusion imaging and angiography 28

3.1 Perfusion imaging 28

3.1.1 Non-magnetic resonance based perfusion imaging 29

3.1.2 MR perfusion imaging with exogenous contrast agents 30

3.1.3 MR perfusion imaging with arterial spin labelling 30

3.1.4 Vessel-selective perfusion imaging with arterial spin labelling . . . 32

3.2 Angiography 35

3.2.1 Non-magnetic resonance based angiography 36

3.2.2 MR angiography with exogenous contrast agents 37

3.2.3 MR angiography with endogenous contrast agents 38

3.2.4 MR angiography with arterial spin labelling 39

3.2.5 Vessel-selective angiography with arterial spin labelling 40

3.3 Conclusions 41

4 An optimised encoding scheme for planning vessel-encoded arterial spin labelling 42

4.1 Labelling efficiency of unipolar VEPCASL 43

4.2 Theory 45

4.2.1 Encoding matrices 45

4.2.2 Generating an optimised encoding scheme 47

4.3 Methods of evaluation 50

4.3.1 Simulations 52

4.3.2 Subject scans 52

4.3.3 Subject scans analysis 54

4.4 Results 55

4.4.1 Simulations 55

4.4.2 Subject scans: four vessels 57

4.4.3 Subject scans: more than four vessels 58

4.5 Discussion and conclusions 60

5 An optimised encoding scheme with off-resonance correction 65

5.1 Theory . . . 67

5.2 Methods of evaluation . . . 69

5.2.1 Choice of ideal encoding scheme . . . 69

5.2.2 Simulations . . . 72

5.2.3 Phantom scans . . . 73

5.2.4 Subject scans . . . 74

5.2.5 Subject scans analysis . . . 77

5.3 Results . . . 78

5.3.1 Simulations . . . 78

5.3.2 Phantom scans . . . 81

5.3.3 Subject scans . . . 82

5.4 Discussion and conclusions . . . 88

6 Time-efficient vessel-selective dynamic angiography 93

6.1 Sequence implementation . . . 94

6.1.1 Radial k-space trajectory . . . 94

6.1.2 Radial image reconstruction . . . 96

6.2 Comparison of readout schemes . . . 101

6.3 Comparison of Cartesian and radial VEPCASL dynamic angiograms . . . 105

6.3.1 Subject scans . . . 105

6.3.2 Results . . . 108

6.4 Discussion . . . 112

6.5 Conclusions . . . 114

7 Vessel-selective three-dimensional dynamic angiography 116

7.1 Sequence development . . . 117

7.1.1 Radial k-space trajectory . . . 117

7.1.2 Radial image reconstruction . . . 118

7.2 Comparison of readout schemes . . . 121

7.3 Sequence optimisation . . . 126

7.3.1 Signal attenuation . . . 127
7.3.2 Undersampling factor . . . 134
7.4 Dynamic 3D VEPCASL subject scans . . . 136
7.4.1 Methods . . . 137
7.4.2 Results . . . 138
7.4.3 Discussion . . . 140
7.5 General discussion . . . 143
7.6 Conclusions . . . 146

8 Summary and future work **147**
8.1 Summary of results . . . 147
8.1.1 Optimisation of VEPCASL encoding . . . 147
8.1.2 Development of dynamic vessel-selective angiography . . . 148
8.2 Future work . . . 150

Bibliography **153**

Chapter 1

Introduction

Cerebrovascular disease can disrupt the haemodynamics of the brain [1]. Consequently, knowledge of the movement of blood through the vascular tree and its delivery to tissue can provide vital information for patient diagnosis and treatment [2]. Perfusion imaging affords information on blood flow to brain tissue and on tissue condition [1]. Cerebral angiography on the other hand allows the study of blood vessels and flow in the neck and brain, leading to knowledge of the status of intracranial arteries. The purpose of this thesis is to detail the development and optimisation of magnetic resonance imaging (MRI) techniques that provide information on tissue perfusion and blood vessels in the brain.

1.1 Motivation

1.1.1 Using perfusion imaging and angiography to detect and treat cerebrovascular disease

Stroke is typified by impediment to the blood supply of the brain, resulting in a swift reduction in brain functionality [3]. Ischaemic stroke occurs as a result of occluded vessels and accounts for the vast majority of strokes [4]. Perfusion imaging and angiography contribute in a variety of ways to the management of ischaemic stroke patients.

Typically perfusion imaging, performed via computed tomography (CT) or MRI, is used to identify tissue that may still be viable [5]. This involves the identification of the un-

salvageable core of an infarct and surrounding tissue that has experienced a reduction in blood supply but may yet be recoverable – the ischaemic penumbra. Angiograms can be acquired using a range of modalities and are important in the identification of occluded vessels following an acute stroke.

Of particular interest in the diagnosis and treatment of ischaemic stroke patients are imaging modalities that can be performed in an acute setting and provide some information on collateral circulation in the brain. Collateral circulation is a result of smaller connecting vessels that stabilise blood flow in the brain when a primary blood supply fails [2]. Poor collateral circulation is linked to rapid infarct growth in stroke patients [6] and the level of collateral circulation may be a predictor of how successful a treatment will be [7]. An understanding of collateral circulation can therefore aid and expand the treatment of ischaemic injury, acute stroke and other cerebrovascular disorders [2]. Vessel-selective perfusion imaging and angiography enable the study of collateral circulation in the brain [8], as can whole brain perfusion to a certain extent [7]. However, only vessel-selective methods are able to identify the feeding arteries of any collateral flow and, as a normal appearing map of cerebral blood flow in the brain can result if there is efficient collateral flow, non-vessel-selective imaging may not always be able to pick up the presence of disease.

In general, angiograms are used to locate any stenoses, occlusions or aneurysms and aid in assessing vessel status in the brain [4]. Three-dimensional (3D) angiography in particular has been shown to be of benefit in diagnosis of, and surgical planning for, cerebral aneurysms, as a detailed view of the arteries from all directions can be generated [9, 10]. Vessel-selective angiography has a range of further applications. In particular, it allows the dominant feeding vessels for arteriovenous malformations (AVMs) and other lesions to be identified, potentially assisting in diagnosis and treatment of these [11]. AVMs are a type of lesion made up of blood vessels, the arterial and venous systems are directly connected through them, and they carry a significant risk of haemorrhage [12].

1.1.2 The challenges of imaging the cerebral vasculature and its perfusion territories

Whilst there are a plethora of imaging modalities capable of perfusion imaging and angiography (Chapter 3) there are particular challenges that come with each. Many common perfusion imaging techniques require either ionising radiation, such as computed tomography (CT), or the administration of a contrast agent, e.g. dynamic susceptibility contrast MRI. Gadolinium based contrast agents are typically used, which have been linked to nephrogenic systemic fibrosis in patients with poor renal function, so are not suitable for all subjects [13]. Additionally, it is difficult to acquire any information on collateral flow in the brain from the majority of perfusion imaging techniques and the MRI methods that provide this information vary in their efficacy and applicability (Section 3.1.4).

Similarly to perfusion imaging, many established angiography techniques require the use of ionising radiation, such as x-ray digital subtraction angiography (DSA) and CT angiography. However, the use of ionising radiation methods is often not appropriate for serial imaging, such as to monitor treatment progression. Popular MRI methods also require use of a contrast agent, typically gadolinium based. X-ray DSA is considered to be the gold standard for imaging the cerebral vasculature, and, unlike CT techniques, can provide vessel specific information. The technique requires catheter insertion for delivery of contrast, however, that can result in serious neurological complications [5, 14]. If knowledge of the feeding arteries for different parts of the cerebral vasculature is desired x-ray DSA, and single vessel-selective MRI methods (Section 3.2.5), can provide information on the vascular network of each artery. Only information about one artery at a time can be acquired so, unless the artery of interest is known, this necessitates multiple scans and is somewhat time inefficient.

To avoid ionising radiation, and excluding patients who are incompatible with contrast agents used, non-invasive MRI methods are an ideal option for perfusion imaging and angiography. Perfusion imaging can be performed using arterial spin labelling (ASL) MRI. It is possible to identify the ischaemic penumbra by looking at the perfusion/diffusion mismatch between ASL and diffusion-weighted MRI [15]. ASL based perfusion imaging can

also provide information on the different vascular territories in the brain, as it can be manipulated to label only specific arteries of interest. Current methods, however, are limited to small numbers of vessels or struggle to be either signal-to-noise (SNR) ratio or time efficient (Section 3.1.4). Pseudocontinuous ASL (PCASL) has become the recommended ASL choice for perfusion imaging (Section 2.2.3) [16] and is also the basis for vessel specific imaging – vessel-encoded PCASL (VEPCASL). However, the presence of magnetic field inhomogeneities negatively impacts on the inversion efficiency of these methods, and may not always be remedied by standard shimming [17].

There are multiple magnetic resonance angiography (MRA) techniques that use blood as an endogenous contrast agent (Sections 3.2.3-3.2.5). ASL methods, however, offer the best opportunity to map the cerebral vasculature in terms of the networks of different feeding arteries, either in the neck or higher up in the brain. Current ASL options, where time-resolved information on multiple vessels is desired, suffer somewhat from lengthy scan times that make them difficult to apply in patient populations. Additionally, there are currently few ways of acquiring time-resolved 3D angiograms with vessel specific information, which would offer the most detailed view of the vasculature for diagnosis and treatment of cerebrovascular disease.

The work in this thesis aims to mitigate some of the issues present in vessel-selective PCASL based perfusion imaging and angiography. Firstly by improving the ability to efficiently extract information on more than four vessels, regardless of the presence of B_0 inhomogeneities. Secondly, developing accelerated angiography acquisitions that improve the clinical viability of vessel-selective scans and, finally, the optimisation of 3D vessel-selective angiography.

1.2 Thesis outline

The following chapters are loosely divided into three parts. Chapters 2 and 3 outline the background theory and existing perfusion imaging and angiography acquisition methods pertinent to later chapters. Chapters 4 and 5 focus on the optimisation of vessel encoding

by VEPCASL, in order to allow minimal numbers of optimised encodings to be acquired for any number of vessels, applicable to both perfusion imaging and angiography. Chapter 5 details the incorporation of a correction for B_0 inhomogeneities that is also effective for PCASL imaging. Chapters 6 and 7 detail the development of two and three-dimensional VEPCASL angiography respectively. Chapter 6 aims to assess the best readout strategy to speed up the acquisition time of time-resolved two-dimensional vessel-selective angiograms to within two minutes. Chapter 7 looks at the optimisation of a protocol to acquire 3D time-resolved VEPCASL angiograms. A summary of the key findings and potential future work arising from this work can be found in Chapter 8.

Chapter 2

Background

The focus of this chapter is a discussion and summary of the main techniques work in this thesis is based on. A brief summary of relevant magnetic resonance imaging (MRI) theory (Section 2.1) is followed by an overview of arterial spin labelling (Section 2.2) and the range of readout options for arterial spin labelling perfusion imaging (Section 2.3) and angiography (Section 2.4).

2.1 Principles of magnetic resonance imaging

The signal in MRI is a result of the effect of an externally applied magnetic field on nuclei within a subject. Here we focus on hydrogen nuclei, or protons, found in water in the body. The use of magnetic fields to firstly generate signal (Section 2.1.1) and secondly manipulate this signal to image internal body structures (Section 2.1.2) is summarised in this section. The material discussed here was taken from the literature [18–22], which contains more complete discussions if needed.

2.1.1 Nuclear magnetisation

Classically in MRI hydrogen nuclei, or 'spins', in the main magnetic field, B_0, of the scanner are modelled as a collection of spinning charged particles with their own magnetic dipole moments, $\boldsymbol{\mu}$. Quantum mechanically, and due to the Zeeman effect of the magnetic

field, the energy of these spins is discretised (split into levels). Protons have spin $^1/_2$ and so have two energy levels: $E_1 = \frac{\gamma\hbar}{2}B_0$, $E_2 = -\frac{\gamma\hbar}{2}B_0$, where γ is the gyromagnetic ratio of the nucleus and $\hbar$ is Planck's constant divided by 2π.

Spins in the lower energy state (E_2) have a component of $\boldsymbol{\mu}$ parallel to B_0 and spins in the higher state (E_1) have an antiparallel component. By convention B_0 is oriented along the z-axis. The difference in the populations (N_1 and N_2) of the energy states, at a given temperature, T, can be calculated according to the Boltzmann equation:

$$\frac{N_1}{N_2} = e^{-\frac{\Delta E}{kT}} \tag{2.1}$$

where k is Boltzmann's constant and $\Delta E = E_1 - E_2$. There are more spins parallel with B_0 than antiparallel, so when the dipole moments are summed there is a resultant magnetisation parallel to B_0. The components of $\boldsymbol{\mu}$ perpendicular to the direction of B_0 are randomly distributed and cancel each other out. If an external magnetic field is not applied to the sample the spins point in random directions and there is no resultant magnetisation.

A number of approximations can be made to Equation 2.1 to yield the magnitude of the resultant proton magnetisation, M. At room temperature and magnetic field strengths used clinically both $kT \gg \Delta E$ and $N_1 \approx N_2 \approx \frac{N}{2}$, where N is the total number of spins. Additionally, the magnitude of the dipole moment for all protons is the same. Combining a first order approximation of Equation 2.1 with the above approximations:

$$M = \Delta N\mu = (N_2 - N_1)\mu = \frac{N\gamma\hbar}{2kT}B_0\mu \tag{2.2}$$

The vast numbers of hydrogen nuclei in the body make M measureable.

The dipole moments of the spins are never fully aligned with the magnetic field however. In a rotating frame of reference M_0 will align with B_0, but the individual spin dipole moments will not. When additional fields to B_0 are added, if these are not aligned with B_0, the resultant magnetisation will feel the effect of a torque from the resultant B-field and will precess around the resultant field. This is shown by the Bloch equation, generalised for any magnetic field $\boldsymbol{B}$:

$$\frac{d\boldsymbol{M}}{dt} = \boldsymbol{M} \times \gamma\boldsymbol{B} \tag{2.3}$$

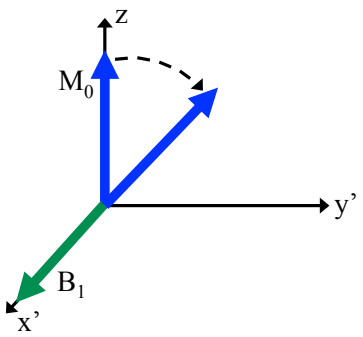


Figure 2.1: In a rotating frame of reference the equilibrium magnetisation M_0 precesses around the applied excitation magnetic field B_1.

The angular frequency, $\boldsymbol{\omega}$, of the precession is given by the Larmor equation, notably the same frequency required to move spins between energy states:

$$\boldsymbol{\omega} = \gamma \boldsymbol{B} \tag{2.4}$$

In a rotating reference frame (rotating about the z-axis at the Larmor frequency ω_0 associated with the constant magnetic field B_0) the resultant, or equilibrium, magnetisation M_0 is a stationary vector along B_0. In this reference frame, in order to measure the magnetisation it must be excited to generate some component in the transverse, x-y, plane. If a circularly polarised magnetic field, oscillating at the Larmor frequency in the laboratory frame, is introduced into the system in the transverse plane it appears as a static magnetic field, B_1, in the transverse plane of the rotating frame. This frequency is typically in the radio-frequency range and B_1 is known as an RF pulse. In the rotating reference frame, when B_1 is applied along one axis M_0 precesses around it towards the transverse plane (Figure 2.1). The duration and amplitude of the B_1 pulse dictate the flip angle of this motion, or excitation.

In the laboratory reference frame, once the B_1 pulse is stopped, a transverse component of the magnetisation (M_{xy}) will rotate around B_0 at the Larmor frequency. This rotating magnetisation induces an electromotive force (emf) in a RF receiver coil placed near (or around) the subject. It is this induced emf, proportional to the magnetisation, which forms the basis of MRI.

After the application of B_1 any remaining longitudinal magnetisation (M_z) relaxes back towards a value of M_0 and the transverse magnetisation decays away. The relaxation times for the longitudinal and transverse components is different, as their relaxation occurs due to different interactions, and these two times vary between tissues and across field strengths. T_1 is the time constant governing the spin-lattice, or longitudinal, relaxation while T_2 is the time constant that dictates the spin-spin, or transverse, relaxation. The overall magnetisation being a combination of M_z and M_{xy}, and being unable to exceed the magnitude of M_0, $T_2 \leq T_1$. If inhomogeneities are present in the magnetic field the transverse magnetisation will appear to decay faster. This decay is covered by the time constant T_2^*.

If the Bloch equation is moved into the rotating frame, and time evolution of the magnetisation added, the resulting equation is:

$$\frac{d\boldsymbol{M'}}{dt} = \boldsymbol{M'} \times \gamma \boldsymbol{B'} - \frac{1}{T_2} \begin{pmatrix} M'_x \\ M'_y \\ 0 \end{pmatrix} + \frac{1}{T_1} \begin{pmatrix} 0 \\ 0 \\ M_0 - M_z \end{pmatrix} \tag{2.5}$$

Primes denote variables observed in the rotating frame and $\boldsymbol{B'}$ constitutes magnetic fields applied other than the main magnetic field B_0.

2.1.2 Basis of MRI: gradients and k-space

To identify spins in different locations it is necessary to give them different resonant frequencies. This is known as spatial encoding and is performed by applying additional magnetic field gradients that make $\boldsymbol{B'}$, and consequently $\boldsymbol{\omega'}$ (Equation 2.4), dependent on position. The gradients apply magnetic fields parallel to B_0; the orientations of the gradients describe the direction in which the strength of the resulting B_z varies. Gradients are designed so that at the magnet isocentre there is no contribution to the magnetic field from the gradients. The resultant magnetic field at position $\boldsymbol{r}$ in a three-dimensional (3D) Cartesian coordinate system during application of a gradient $\boldsymbol{G} = (G_x, G_y, G_z)$ is therefore:

$$B_z(\boldsymbol{r}) = B_0 + \boldsymbol{G} \cdot \boldsymbol{r} \tag{2.6}$$

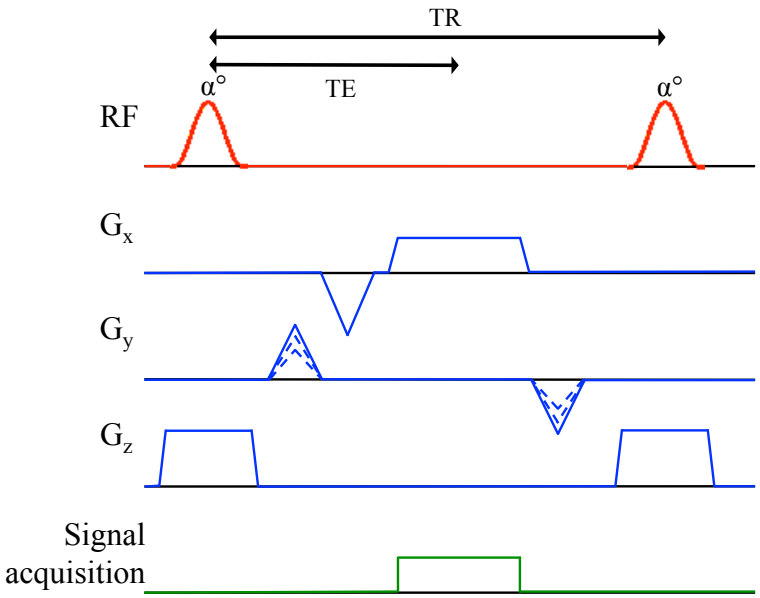


Figure 2.2: Basic pulse sequence diagram. Slice/slab selection occurs when G_z and the α° RF excitation pulse are played out together. The strength of G_y changes each time the sequence is repeated in order to spatially encode different rows of frequencies. Signal acquisition occurs during the readout (G_x) gradient. The repetition time (TR) is the time between excitation pulses, whilst the echo time (TE) is the time between the centre of the RF pulse and the centre of the signal acquisition.

The slice selection gradient (e.g. G_z) is applied to selectively excite a slice, or slab. For example, G_z varies the magnetic field in the z-direction so only a single x-y plane resonates at a given frequency. Thus when an RF pulse is applied at that frequency in the presence of the slice selection gradient (Figure 2.2), only magnetisation within a single plane will be excited. The location of the plane can be altered by varying the frequency of the applied RF pulse. To selectively excite a slice/slab with a certain width, Δz, an RF pulse must be used that excites a small range of frequencies, $\Delta\omega$.

In order to build up an image of the selected slice two further gradients are applied to achieve spatial localisation of points in the transverse plane. The frequency encoding, or readout, gradient (e.g. G_x) is applied during signal acquisition to encode positions (pixels, or voxels in three-dimensions) along, for example, the x-axis, i.e. each point along the line has its own resonant frequency. The total signal measured is the sum of all the pixel frequencies in the selected slice; the magnitude of these signals is determined by the magnetisation in each pixel. The second gradient is the phase encoding gradient (e.g. G_y),

applied prior to the readout gradient to encode points along the y-axis. When the phase encoding gradient is switched off the entire slice goes back to resonating at ω_0 but the rows along the y-axis are now at different phases. G_y is applied at regular time intervals, at different strengths, to encode each row one after the other (Figure 2.2). An image can then be constructed by Fourier transform of the data. The acquisition of different signal frequencies and how they are reconstructed into an image is best described by the k-space formalism.

k-space

The measured MR signal is proportional to the net transverse magnetisation and its phase. The mathematical description of MRI is simplified by the use of the k-space formalism, within which the transverse magnetisation is represented by complex numbers: $M_{xy} = M_x + iM_y$.

For an applied gradient $\boldsymbol{G}(t)$ the phase of the spins at a position $\boldsymbol{r}$ at time t is given by:

$$\phi(\boldsymbol{r}, t) = \int_0^t \boldsymbol{\omega}(t)dt = \int_0^t \gamma \boldsymbol{B}(t)dt = \int_0^t \gamma \boldsymbol{G}(t) \cdot \boldsymbol{r}dt \tag{2.7}$$

Consequently, the resultant signal in the presence of G_x and G_y is:

$$S(t) \propto \iint M_{xy}(x, y)e^{-i\gamma x \int G_x dt} e^{-i\gamma y \int G_y dt} dxdy \tag{2.8}$$

The k-space formalism allows a simplification of Equation 2.8:

$$S(k_x, k_y) \propto \iint M_{xy}(x, y)e^{-ik_x x} e^{-ik_y y} dxdy \tag{2.9}$$

where $k_x = \gamma \int G_x dt$ and $k_y = \gamma \int G_y dt$. Using this convention we can identify S as being the 2D Fourier Transform of M_{xy}, with k_x and k_y representing the spatial frequency which has been imposed on the magnetisation by the action of the gradients. Position in k-space is therefore proportional to the accumulated area of the gradient waveforms and the way in which the sequence moves through k-space is free to be determined (Section 2.4.2). The k-space formalism can be generalised to three-dimensions to fully encode voxels within an excited 3D slab.

2.1.3 The Bloch equation in an effective field

To model the effects of a given MRI sequence all the applied magnetic fields can be included in the Bloch equation (Equation 2.5). This encompasses RF pulses, gradients and other magnetic fields present along the longitudinal axis due to magnetic field inhomogeneities. The cumulative result is an effective magnetic field, $\boldsymbol{B_{eff}}$, in the rotating frame of reference, made up of three components:

1. RF field

$$\boldsymbol{B_1} = B_1 \begin{pmatrix} \cos\phi_1 \\ -\sin\phi_1 \\ 0 \end{pmatrix} \tag{2.10}$$

   B_1 is the magnitude of the RF field and ϕ_1 its phase. The RF field is on-resonance here

2. Gradient field

$$\boldsymbol{B_G} = \begin{pmatrix} 0 \\ 0 \\ \boldsymbol{G \cdot r} \end{pmatrix} \tag{2.11}$$

   $\boldsymbol{G}$ is the vector representing the gradients while $\boldsymbol{r}$ is the position of the magnetisation

3. Off-resonance effects

$$\boldsymbol{B_{OR}} = \begin{pmatrix} 0 \\ 0 \\ \frac{\omega_{OR}}{\gamma} \end{pmatrix} \tag{2.12}$$

2.2 Arterial spin labelling

Arterial spin labelling (ASL) uses the blood as an endogenous contrast agent. The magnetisation of blood flowing into the brain is inverted using RF pulses; it is magnetically labelled. After a delay, so labelled blood can move through the vasculature of interest and/or perfuse into the brain tissue, an image is acquired. A control image, where no labelling has occurred, is also acquired. The subtraction of these two images leaves only signal from labelled blood, signal from static tissue is subtracted out [16]. The T_1 relaxation time of blood at the imaging field strength dictates the lifetime of the blood as a tracer.

As a result the delay between labelling and acquisition (the post labelling delay, or PLD) is a trade off between ensuring labelled blood has had time to reach the vessels of interest, or brain tissue, and avoiding the loss of signal through increased relaxation of the longitudinal magnetisation.

The signal difference measured in a single ASL perfusion acquisition is small – on the order of 1% of the brain tissue signal [23] – so multiple measurements are typically required to boost the signal-to-noise ratio (SNR) through averaging. If the control and labelled images are similarly acquired, i.e. the off-resonance and magnetisation transfer (MT) effects of the label and control acquisitions are the same, then the ASL difference signal in the perfused tissue is related to the cerebral blood flow (CBF) [24].

The MR signal measured here comes from the magnetisation of hydrogen spins in "free" water; the labelling pulses are tuned to the resonance frequency of these spins in the labelling slab. MT effects occur when the magnetisation of hydrogen nuclei bound to macromolecules present in the imaging slice is saturated [25]. Free water spins in the imaging region would see an off-resonance labelling pulse and remain unaffected, however the varied nature of macromolecules means the labelling pulse will be on-resonance for some of them. Magnetisation can then be exchanged between the free water and macromolecule bound spins, resulting in a change in the free water, or static tissue, signal in the imaging region [25]. Consequently, additional differences between the control and label acquisitions not due to perfusion will occur if MT effects are not considered.

For perfusion imaging, in the general ASL kinetic model described by Buxton *et al.* [24] it is assumed that water, and so labelled blood, is rapidly exchanged between the capillaries and brain tissue. The ASL signal is a function of the measurement time, with a period of no signal before the labelled blood arrives, followed by an accumulation of labelled blood water and then signal decay. The ASL signal can only be considered proportional to the CBF if the PLD is long enough for the entire labelled bolus of blood to have reached the tissue. The ideal PLD for perfusion imaging varies depending on the subject and/or the arteries being labelled, due to differences in blood velocity, but is on the order of 1800 ms [16].

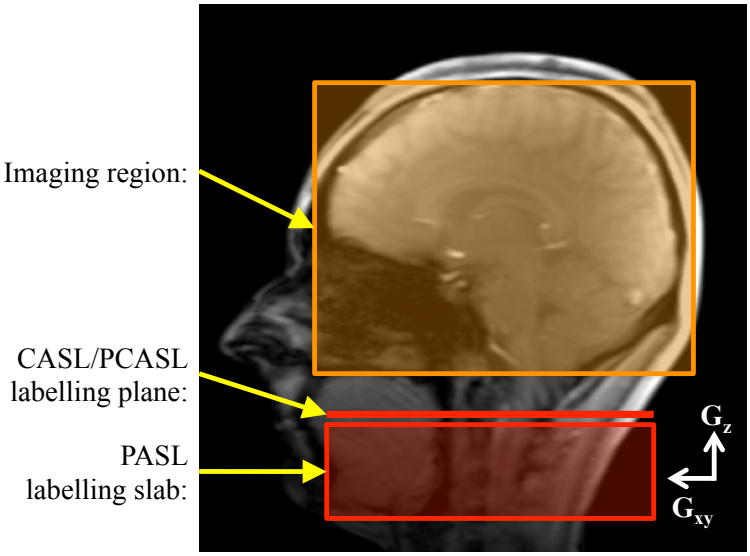


Figure 2.3: A labelling slab and plane are shown in red at typical locations to label the main brain-feeding arteries in the neck (right and left internal carotid arteries and right and left vertebral arteries). The directions of the longitudinal (z) and transverse (xy) gradients are also shown relative to the labelling slab/plane locations.

2.2.1 Pulsed arterial spin labelling

Pulsed arterial spin labelling (PASL) applies, in general, a single 180° RF labelling pulse across a slab containing the vessels below, and supplying blood to, the imaging region (Figure 2.3). The blood magnetisation is thus inverted and left to flow into the brain tissue prior to imaging. As mentioned above, the control acquisition must take care to recreate the effects of labelling on the static tissue to ensure the subtraction image is a true reflection of the CBF.

PASL does not require any additional hardware to implement on a clinical scanner and, due to the minimal usage of RF pulses to invert blood magnetisation, the specific absorption rate (SAR) of PASL sequences is typically low. It is possible to invert blood relatively close to the imaging region, however the profile of the inversion pulses is not perfect, necessitating a gap of 1-2 cm [26]. The time taken for the labelled blood to travel to the imaging region is therefore increased. This leads to a reduction in acquisition efficiency and extra time for T_1 relaxation of the magnetisation, resulting in a reduction in the acquired ASL signal.

2.2.2 Continuous arterial spin labelling

The second major approach to ASL is continuous ASL (CASL). The technique adiabatically inverts blood flowing through a labelling plane (Figure 2.3) by applying a continuous RF pulse alongside a gradient in the direction of blood flow [26]. The blood magnetisation sees a slowly changing gradient term as it moves through the labelling plane; the effective field the magnetisation sees is inverted and so the magnetisation, which precesses about the effective field, is also inverted. The RF pulse typically has low amplitude and is applied for a few seconds. Theoretically the longer steady-state labelling of CASL results in a higher SNR versus PASL [27], however, the particular version of CASL used has a considerable effect on the labelling efficiency, which can range from 70-96% [23].

The labelling process in CASL produces a bolus of tagged blood whose temporal length is the same as the RF pulse duration. However, MT effects are much more difficult to resolve for CASL, as opposed to PASL. A variety of solutions have been suggested. Initially continuous labelling was applied above the imaging slice during the control acquisition, but it is not possible to extend this method to multi-slice imaging [23]. Other options include using a modulated RF pulse during the control acquisition to prevent inversion of inflowing blood [28]. This technique has a higher SAR than PASL and is therefore not possible at higher field strengths. The use of separate labelling and imaging coils has also been suggested, as a coil directly at the labelling plane would allow labelling only of the region close to it and so avoid MT effects [23]. Unfortunately this necessitates additional hardware that is not always available.

2.2.3 Pseudocontinuous arterial spin labelling

In an effort to increase labelling efficiency and reduce MT effects, and to capitalise on the SNR advantage of CASL over PASL, pseudocontinuous ASL (PCASL) was developed. PCASL works by applying a train of RF pulses and (typically z) gradients, which affect the magnetisation of blood flowing through a defined labelling plane [29] (Figure 2.3). PCASL works similarly to CASL; the magnetisation of the blood is adiabatically inverted

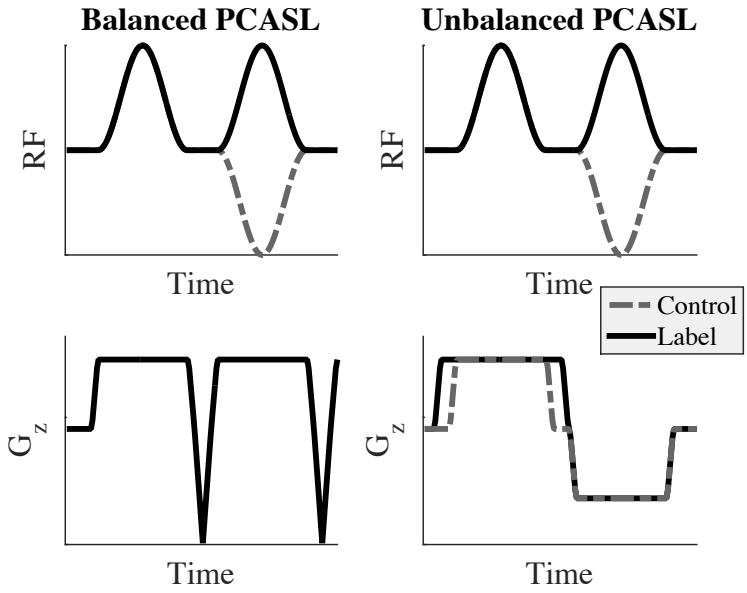


Figure 2.4: The sequence diagrams for balanced and unbalanced PCASL. The mean G_z gradient during balanced PCASL $\neq 0$. Mean G_z gradient during unbalanced PCASL $\neq 0$ during the labelling cycle and $= 0$ in the control case.

as it follows the steady-state position of the magnetisation. Breaking the continuous RF pulse train into a string of pulses improves the labelling efficiency for the same power deposited in CASL [27]. The PCASL control state consists of the same pulse train, except the phase of every other RF pulse is alternated between zero and 180°, so the magnetisation is not affected significantly. The spacing of the RF pulses should be kept to a minimum to avoid sensitivity to magnetic field inhomogeneity: typically peak-to-peak spacings of 1 ms or less can be achieved [16]. Values for the flip angle of the RF pulse – or their mean B_1 – vary but are typically close to 20° [30, 31].

Different versions of PCASL are possible by varying the z gradients applied during the labelling pulse train. Unbalanced PCASL [32] uses different z gradients for the labelling and control cases, whereas balanced PCASL [30] applies the same gradients in both cases (Figure 2.4). The two methods are very similar, however the unbalanced method is more sensitive to eddy current artefacts, whilst the balanced method is more sensitive to off-resonance effects [27]. Typical the z gradients have an amplitude of about 10 mT/m during RF pulses and a mean strength of 1 mT/m.

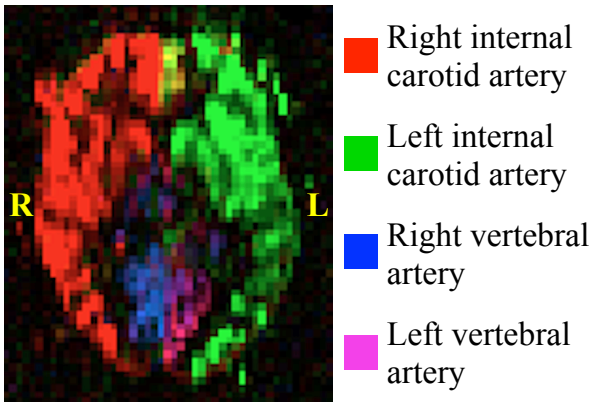


Figure 2.5: Perfusion territories of the four main brain-feeding arteries, acquired following VEPCASL with a labelling plane in the neck.

2.2.4 Vessel-encoded pseudocontinuous arterial spin labelling

Vessel-encoded PCASL (VEPCASL) is based on balanced PCASL. The pulse sequence is modified such that the labelling efficiency varies periodically across the labelling plane, so multiple vessels of interest can be labelled at once [30]. By combining information from multiple scans, in which different combinations of vessels are labelled, individual vascular territories can be extracted (Figure 2.5).

VEPCASL takes advantage of the space between pulses in the PCASL train to insert additional transverse gradients. These gradient 'blips' create a phase shift between different locations in the labelling plane. The phase of the RF pulses can then be modulated to place these locations in a controlled or labelled state [30]. The result is an inversion, or labelling efficiency, curve that varies approximately sinusoidally across the labelling plane. The frequency and phase of this encoding function can be adjusted to label and control chosen locations. A perfectly labelled vessel corresponds to the blood longitudinal magnetisation taking a value of -1 (in units of M_0), i.e. perfectly inverted, while a perfectly controlled vessel has a value of +1. Regions in between label and control locations experience an intermediate labelling value (Figure 2.6).

Although the labelling efficiency modulation is approximately sinusoidal, its shape depends on the velocity of the blood, magnetic field inhomogeneities and the choice of transverse gradient size and direction. In bipolar VEPCASL [30] the phase encoding blips alternate

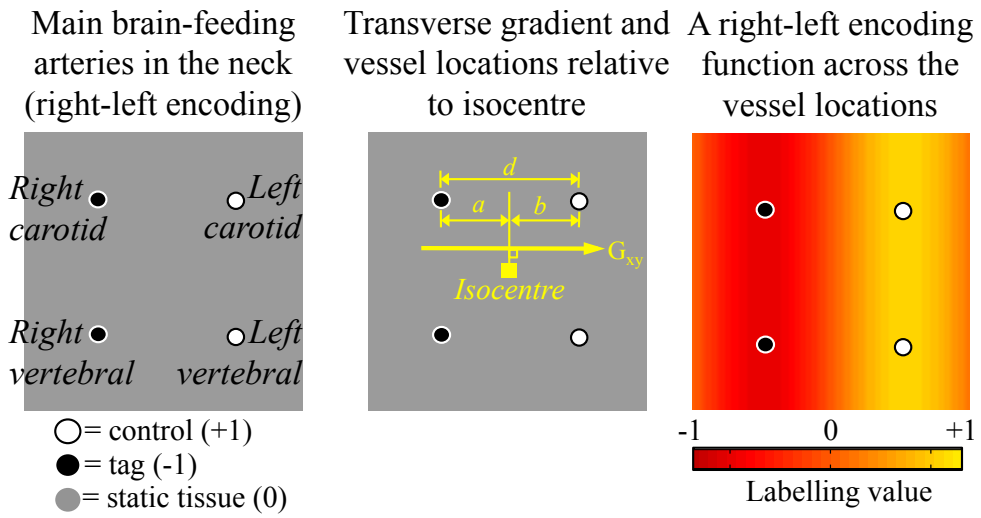


Figure 2.6: A labelling plane showing an idealised version of the four main brain-feeding arteries and the desired encoding; a right-left encoding to label blood in the right hand vessels while simultaneously controlling the left hand vessels. The encoding function has adjustable spatial frequency and phase within the labelling plane.

between positive and negative. In unipolar VEPCASL [33] they are all applied in the same direction (Figure 2.7) and the resulting inversion efficiency function can be represented by a sum of Fourier coefficients. This function is close to a pure sinusoid and off-resonance effects cause a simple shift of the inversion efficiency function, as opposed to a reduction in inversion efficiency as in bipolar VEPCASL [33].

As mentioned above, to keep the RF pulses coherent with spins in the labelling plane their phase needs to be modulated. When no transverse gradients are applied, i.e. all vessels in the labelling plane are to be tagged, the phase is a function of the mean G_z gradient and the RF pulse spacing: $\phi_z = n\gamma\bar{G}_z t z$, where n is the pulse number, γ the gyromagnetic ratio, t the RF pulse spacing and z is the distance of the labelling plane from isocentre. During the control condition π radians is added to the phase of every other pulse to prevent inversion of the magnetisation.

The area of the transverse gradient blips applied during vessel-selective cycles of VEPCASL is equal to $\pi/\gamma d$, where d is the separation distance between the locations (vessels) to be tagged/controlled [30]. When transverse gradients are present, the RF pulse phase is further modulated to keep them coherent with particular locations in the labelling plane.

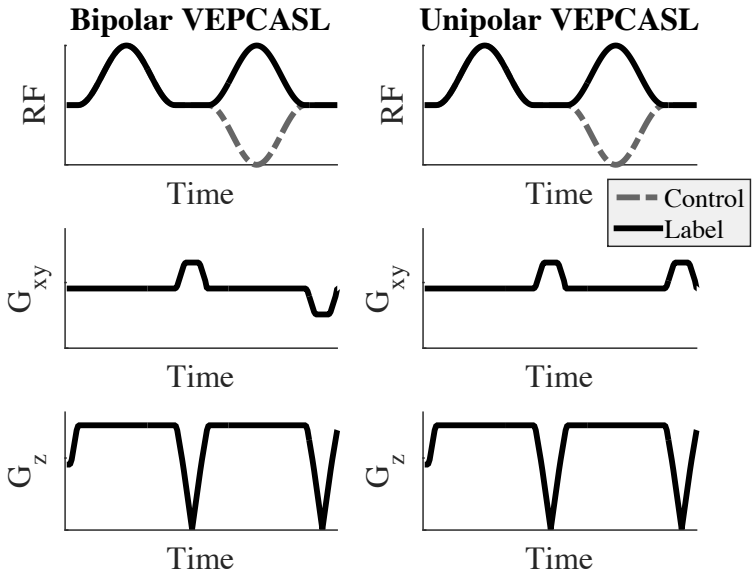


Figure 2.7: Sequence diagrams for bipolar and unipolar VEPCASL.

The phase depends on whether the sign of the phase encoding blips alternates (bipolar VEPCASL) or stays the same (unipolar). From the example in Figure 2.6, to label the right hand vessels and control the left hand, the phase of the nth RF pulse for bipolar VEPCASL is: $\phi_{xyRH} = \phi_z + \frac{(n\%2)\pi a}{d}$, where % is the integer modulus function. Similarly, to control the right hand and label the left hand vessels: $\phi_{xyLH} = \phi_z + \frac{(n\%2)\pi b}{d}$. For unipolar VEPCASL the added phase is no longer zero if it is an even numbered RF pulse: $\phi_{xyRH} = \phi_z + \frac{n\pi a}{d}$, $\phi_{xyLH} = \phi_z + \frac{n\pi b}{d}$.

2.3 ASL perfusion imaging acquisition strategies

Following an ASL magnetisation preparation there are multiple ways of acquiring the signal in the imaging region. Some of the general requirements and most popular readout schemes are summarised below.

Acquisition strategies that provide the optimal SNR for ASL perfusion imaging are 3D segmented readouts [16]. They are both relatively time efficient and often insensitive to magnetic field inhomogeneity. Two such sequences that have been widely adopted are 3D RARE and 3D GRASE acquisitions [34]. RARE (rapid acquisition with relaxation

enhancement) follows an RF excitation pulse with a train of refocusing pulses to acquire multiple RF spin echoes [35]. Multiple lines in k-space can therefore be acquired after each excitation pulse so the total acquisition time can be reduced. 3D RARE sequences acquired as a stack of spirals in k-space have been used for perfusion imaging [36]. GRASE (gradient and spin echo) also uses a train of RF refocusing pulses, but combines these with a train of gradients to refocus a series of both RF spin echoes and gradient echoes [35] and acquire multiple k-space lines after every excitation pulse.

Single-shot 2D readouts are also commonly used for ASL perfusion imaging, in particular echo-planar imaging (EPI) and spiral k-space trajectory acquisitions, both for single slice and multi-slice 3D imaging [30, 37]. EPI uses a train of gradients to refocus a series of gradient echoes and acquire a series of k-space lines after every excitation pulse [35]. Both readouts perform similarly for ASL [16], do not suffer from through-slice blurring and are relatively robust to subject motion, although they have lower SNR than 3D segmented methods [35, 36].

As mentioned in Section 2.2, the ASL signal is much smaller than the brain tissue signal [23]. Physiological fluctuations and subject motion adds to noise (and artefacts) in un-subtracted ASL images, so reducing the static tissue signal whilst maintaining the ASL difference signal increases the ASL SNR [16]. In order to reduce the static brain tissue signal in this way, for any chosen acquisition strategy, saturation and inversion pulses are applied to achieve background suppression within ASL scans. Typically a selective RF saturation pulse is applied to the imaging region prior to the ASL preparation, followed by a series of inversion pulses that affect both the blood and static tissue, although the ASL difference signal is relatively unaffected. This results in the longitudinal magnetisation of the static tissue being close to zero just prior to image acquisition.

2.4 ASL angiography acquisition strategies

If a very short PLD is used then the majority of the labelled blood still resides in the large arteries, so angiographic images can be obtained. Typically, higher spatial and temporal

resolution is required for angiography, resulting in different image acquisition strategies. Similarly to perfusion imaging there are a range of potential readout options for ASL MRA. The single line methods described in Section 2.4.1 can all be combined with the various k-space trajectories discussed in Section 2.4.2 [8, 38–40].

2.4.1 Single line methods

Gradient echo based single line methods, an example of which is seen in Figure 2.2, have commonly been used to acquire ASL angiography data. After RF excitation a single line in k-space is acquired. The structure of the pulse sequence affects the final signal measured and its sensitivity to, for example, inhomogeneities in the imaging plane. Such single line methods must be repeated in order to acquire the whole of k-space. Typically in ASL angiography multiple lines in k-space will be acquired after each ASL magnetisation preparation.

Spoiled gradient echo (SPGR) sequences 'spoil' the transverse magnetisation to ensure that M_{xy} is approximately equal to zero before the next excitation. Spoiling is typically performed by quadratically varying the phase of the applied RF excitation pulses during the acquisition [41]. An additional gradient is also applied to dephase signal from spins at the end of each repetition time (TR) [42]. As a result the transverse magnetisation is approximately equal to zero at the end of each TR. The optimal flip angle for SPGR sequences, assuming perfect spoiling, is defined by the Ernst angle: $\alpha_E = \cos^{-1}(e^{-TR/T_1})$.

Instead of spoiling the transverse magnetisation prior to the next excitation it can be recycled through TR periods, resulting in an increased signal level. Sequences of this kind are known as steady-state free precession (SSFP) acquisitions. Specifically here we are interested in balanced SSFP (bSSFP). When a series of phase coherent excitation pulses and gradients are applied, with a TR similar to or less than the T_2 in the imaging region, a steady-state of the transverse magnetisation will eventually be reached, where the magnetisation will behave in the same way from one TR to the next [41]. In bSSFP acquisitions the transverse magnetisation is not equal to zero before each excitation, resulting in a higher signal level during acquisition versus SPGR.

For bSSFP the total area underneath the gradients on all axes must be zero for each TR. The precession of the transverse magnetisation during the repetition time affects the bSSFP signal. If there are field inhomogeneities in the imaging region they will affect the phase of the magnetisation, which can result in banding artefacts – where there is very little bSSFP signal in bands across the imaging region. To minimise this additional precession, and so the banding artefacts, the TR is kept as short as possible. The flip angle (α) yielding maximum signal in bSSFP scans with a short TR is determined by the T_1 and T_2 [41] $\alpha = \cos^{-1}(\frac{T_1 - T_2}{T_1 + T_2})$.

The time taken for a bSSFP sequence to reach the steady-state regime depends on the exact parameters. In order to quickly reach steady-state a range of preparations has been developed. Mostly simply, a single preparation pulse can be applied with flip angle $\frac{\alpha}{2}$, followed by a time delay of $\frac{\mathrm{TR}}{2}$ before the bSSFP sequence proper starts [43]. This places the magnetisation at its steady state value prior to imaging. However, this only applies to spins that are on-resonance with the applied RF pulse so there will be continued signal fluctuation for a time before the system reaches the steady state [44]. An alternative way to initialise the bSSFP signal is to use a series of RF pulses with linearly varying flip angles, either decreasing [44] or increasing [45], to more gradually bring the transverse magnetisation towards the steady-state [44]. The result is a reduction in artefacts, due to the decrease in signal fluctuations as the system reaches the steady-state faster. bSSFP can be combined with any magnetisation preparation, such as ASL, to produce images with high SNR [43].

2.4.2 k-space trajectories

There are multiple ways to sample k-space. The most common strategy, Cartesian sampling, and an alternative non-Cartesian strategy, radial sampling, are summarised below. Radial sampling is of particular interest for ASL angiography due to its reduced sensitivity to motion artefacts [46] and the nature of artefacts when k-space is undersampled. Certain types of radial trajectory have also been shown to reduce flow artefacts [47].

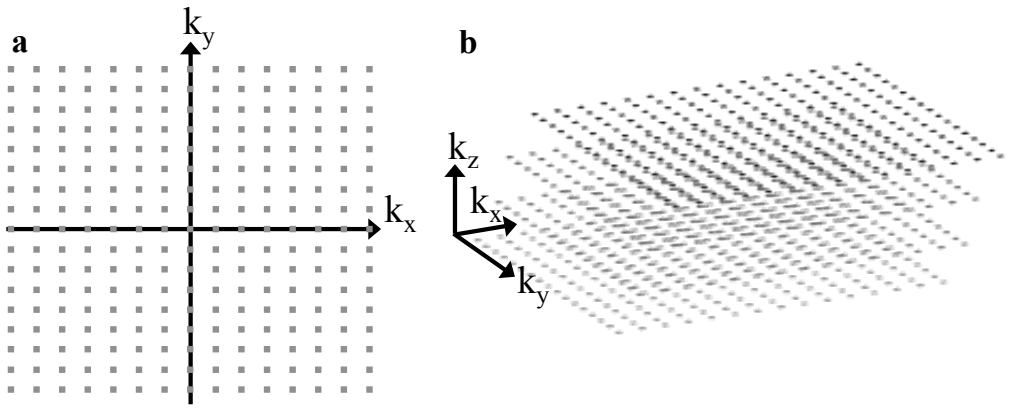


Figure 2.8: Cartesian k-space trajectories in **a**: two dimensions and **b**: three dimensions. The 3D k-space is shown here as a stack of 2D acquisitions.

A Cartesian trajectory samples equally spaced points in the k_x and k_y directions, and k_z for 3D readouts (Figure 2.8). The reconstruction of k-space into an image can be simply performed through a Fourier transform, typically a fast Fourier transform (FFT), of the acquired k-space grid. Cartesian sequences are less sensitive to hardware imperfections, when compared to non-Cartesian trajectories. B_0 inhomogeneities and gradient non-linearity will distort Cartesian-acquired images, while radially acquired images also experience blurring along with distortion [48].

Cartesian acquisitions can be accelerated in various ways, such as only partially acquiring k-space [49] or by undersampling k-space in the phase encode direction (i.e. increasing the distance between lines in k-space in the phase encode direction). With Cartesian trajectories this can introduce artefacts such as Gibbs ringing and aliasing artefacts. Additionally, parallel imaging can be combined with Cartesian trajectories to further reduce scan times, although the images acquired have a lower overall SNR and can suffer from loss in signal at certain points, due to phase cancellation between coils, and be prone to aliasing artefacts [50].

Radial sampling acquires projections, or spokes, across k-space (Figure 2.9). Typically the points along spokes are evenly spaced, which results in denser sampling near the centre of k-space compared to the periphery. The reconstruction of radial images, versus Cartesian, is non-trivial, as a standard FFT cannot be applied to a sampling pattern that does not fall

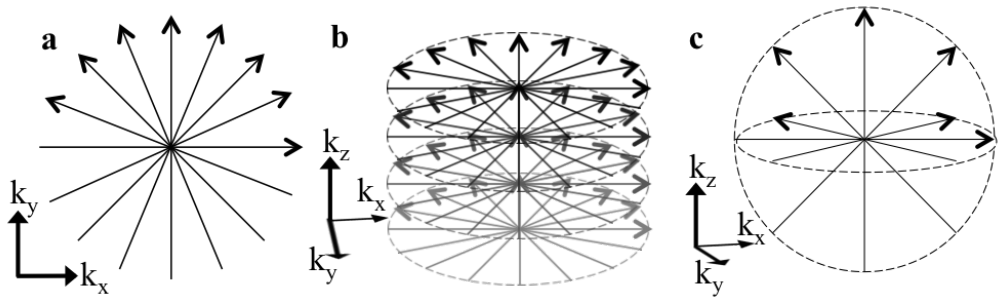


Figure 2.9: Radial k-space trajectories in **a**: two dimensions, **b**: three dimensions as a stack of 2D acquisitions and c: three dimensions in the form of a starburst ('true' 3D radial).

on a rectilinear grid. Additionally, the Nyquist criterion, which describes the necessary number of points that must be acquired to avoid image aliasing [51], is greater for radial imaging. For Cartesian images the Nyquist criterion requires the number of phase-encoding lines, N_{phase}, to equal the desired matrix size in image space: $N_{phase} = \mathrm{FOV}/\Delta x$, where Δx is the voxel size. In order to acquire data with the same FOV and spatial resolution and to satisfy the Nyquist criterion for radial imaging: $N_s = \frac{\pi}{2} N_{phase}$, where N_s is the number of radial spokes [48]. These spokes traverse the entire diameter of k-space (Figure 2.9.a). As a result of acquiring more lines in k-space a fully sampled radial trajectory has a greater overall acquisition time than the equivalent Cartesian trajectory.

The effects of undersampling on radially acquired images are different to Cartesian imaging. When angularly undersampled, i.e. less spokes in k-space are acquired, noise-like "streak" artefacts appear outside a central region around each point in the image. The size of the artefact-free region is a function of the angular sampling density [48] and the magnitude of the artefacts is proportional to the signal in the associated image location. If the majority of signal in the image is concentrated towards its centre then the stronger artefacts will be at the image periphery. Radial trajectories can also be combined with parallel imaging methods [52] but as the undersampling artefacts can be less disruptive than those seen in Cartesian imaging it is not as commonly used.

Radial trajectories can be acquired in three dimensions, either as a stack of stars or as a starburst – 'true' 3D radial imaging (Figures 2.9.b and c). The Nyquist criterion for true 3D radial imaging increases the necessary number of spokes to $N_s = 2\pi(k_{max} \cdot \mathrm{FOV})^2$

[48], where the spokes are acquired across the whole of k-space. Undersampled 3D radial trajectories, where k-space is evenly undersampled, have been used to acquire ASL angiograms [39, 40].

Of benefit to magnetic resonance angiography is the fact that radial k-space sampling has a reduced sensitivity to motion and, for certain radial trajectories acquired using half-spokes, to flow artefacts [48]. Additionally, the undersampling artefacts of radial acquisitions are particularly compatible with angiography: the data is sparse and streak artefacts are at to the edges of images, away from the arteries of interest [53, 54]. However, radial imaging is typically considered less robust than Cartesian sampling, due to a higher degree of sensitivity to hardware flaws and the more complicated reconstruction required. A range of reconstruction possibilities is discussed in the next section.

2.4.3 Non-Cartesian trajectory reconstruction strategies

Methods are discussed here in the context of radial k-space image reconstruction. However, most of the reconstruction strategies discussed are applicable to other non-Cartesian trajectories.

The first MR images were acquired using radial sampling and were reconstructed in a similar way to computed tomography – via filtered backprojection. Filtered backprojection in MRI makes use of the central slice theorem to reconstruct an image by projecting and then summing the one-dimensional FTs of each spoke in k-space (Figure 2.10). A filter is added to each spoke to reduce blurring artefacts in the final images [48]. A highly constrained backprojection algorithm (HYPR) has more recently been developed for time-resolved data [53–55]. HYPR makes use of all the acquired data to better inform the reconstruction of individual time frames. The result is a significant reduction in streak artefacts.

More common than filtered backprojection is gridding, or re-gridding, where non-Cartesian data is interpolated onto a Cartesian grid and a FFT applied to generate an image. The gridding process requires multiple steps [49]:

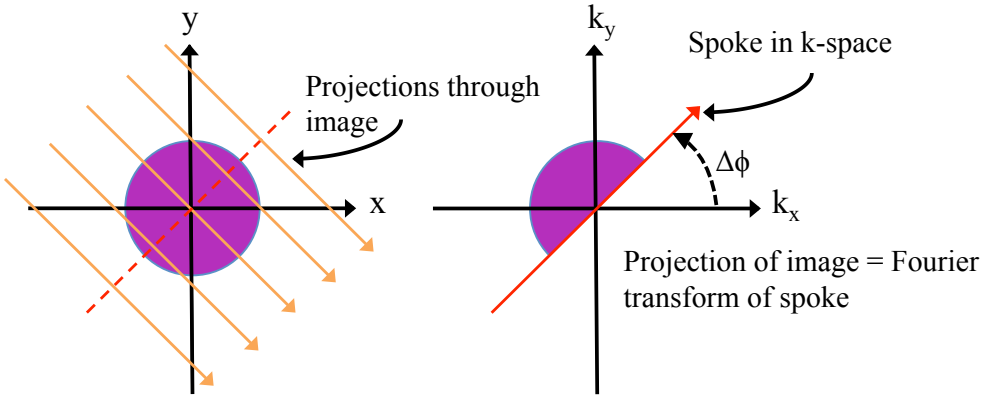


Figure 2.10: The central slice theorem as used in filtered backprojection. Fourier transforms of spokes in k-space can be used to reconstruct an image.

1. Apply density compensation to each point in k-space, to account for variable density of sampling (e.g. radial trajectories are more densely sampled at the centre of k-space so these samples are down-weighted relative to those at the periphery)

2. Interpolate the non-Cartesian k-space data by convolution with a gridding kernel and re-sampling onto a Cartesian grid

3. Apply a FFT

4. De-apodise the image by dividing by the apodisation function (the FT of the convolution kernel)

Density compensation can be performed at the beginning or end of the process. In general it is preferable to perform it at the start, but it may be non-trivial to compute if the trajectory is not a simple one. To minimise the number of calculations, and reduce the computation time required during interpolation, the gridding kernel needs to be a compactly supported function. There is a wide range of kernels, but the optimum is considered to be the Kaiser-Bessel function [49]. The choice of the grid onto which the data is sampled is free to be chosen, but choosing a grid with smaller spacing than the original data reduces overlap artefacts in the images. These artefacts occur as the rectilinear re-sampling of k-space before Fourier transform results in replica images in image space.

Reconstruction of non-Cartesian data could be performed by the discrete direct FT of the

acquired k-space samples, but this is very computationally intensive. Algorithms, known as non-uniform fast Fourier transforms (NUFFT), have been developed to speed up the process. The NUFFT is essentially a more generalised version of gridding; optimised convolution kernels are calculated based on the given samples [56], typically for small regions in k-space. The NUFFT method developed by Fessler and Sutton uses a min-max criterion to choose interpolation that minimises the worst case approximation of the interpolated data to the true image [57]. In this particular method scaling factors, to help compensate for imperfect interpolation, were chosen numerically. NUFFT algorithms are capable of speeding up the gridding process while using interpolation, or convolution kernels, better optimised to the data.

2.5 Summary

The underlying principles important to work detailed later in this thesis have been discussed here. The response of the overall magnetisation in a sample to applied magnetic fields has been described in terms of the Bloch equations and a particular focus was given to the principles behind ASL, as the techniques developed in the following chapters are based around unipolar VEPCASL. The Bloch equations are exploited in Chapter 4 to give a greater understanding of how unipolar VEPCASL inverts the magnetisation of blood flowing through the labelling plane. Different acquisition strategies, suitable for combination with ASL, have also been reviewed. Chapters 6 and 7 combine VEPCASL with radial acquisition strategies and thus require non-standard reconstruction techniques.

The next chapter summarises current methods for perfusion imaging and angiography, specifically related to the investigation of cerebrovascular disease. Specific examples of the ASL methods outlined in Section 2.2 are also detailed.

Chapter 3

Current methods in cerebral perfusion imaging and angiography

There are a variety of perfusion imaging and angiography methods used in clinical settings to gain information on the cerebral vasculature and blood supply to both tissue and lesions. Such information includes measures of cerebral blood flow (CBF), knowledge of collateral circulation in the brain and identification of specific feeding vessels for lesions including arteriovenous malformations. A greater understanding of perfusion across the brain and the cerebral vasculature can inform diagnosis and treatment of a wide range of cerebrovascular diseases. Here, some of the most common techniques used clinically for perfusion imaging and angiography, including their main strengths and weaknesses, are outlined. Both the sections on perfusion imaging (Section 3.1) and angiography (3.2) are broken down in terms of non-magnetic resonance and magnetic resonance (MR) based techniques. MR based methods are further broken down into those using exogenous or endogenous contrast agents, with a particular focus on vessel-selective MRI methods.

3.1 Perfusion imaging

Perfusion imaging provides information on the flow of blood to tissue, with perfusion here defined as the rate of blood delivery to a given tissue mass (or volume [48]). CBF is a measure of steady-state tissue perfusion and, for injected contrast agents, is typically measured in millilitres per 100 grams of tissue per minute. Cerebral blood volume (CBV)

is a measure of how much space blood occupies in a given volume and has typical units of millilitres of blood per 100g of tissue. The mean transit time (MTT) is the average time it takes a given tracer to pass through the tissue. For contrast agents that are not freely diffusible, and remain in the vasculature, the MTT is the ratio of CBV to CBF, measured in minutes. For MRI methods like arterial spin labelling (Section 2.2), where the magnetically labelled water protons are freely diffusible, the MTT will be much longer [48].

There are many imaging modalities that are capable of providing information on perfusion in the brain [58]. However, not all are a viable option in an acute setting, such as positron emission tomography and single photon emission computed tomography [58]. Additionally, if information on any collateral circulation is desired, only certain modalities can provide the necessary information. An increased MTT can be an indicator of collateral flow to an area – as blood tends to flow more slowly in collaterals [7], but techniques that provide information on specific vessels can show the feeding vessels of collateral circulation and blood flow to tissue or lesions of interest [30, 59–65]. The choice of imaging modality will greatly depend on the desired information and equipment available.

3.1.1 Non-magnetic resonance based perfusion imaging

Computed tomography (CT) can provide information on brain haemodynamics via measurement of CBF, CBV and MTT. CT images are built up by looking at the signal attenuation of x-rays through an object of interest from a multitude of angles around it. Attenuation depends on the tissue the x-rays pass through [22]. Measuring perfusion with CT requires use of a contrast agent, typically an iodinated agent administered intravenously [58], in order to image the flow of blood.

CT perfusion imaging provides reproducible and quantitative information, possible in an acute setting in a relatively short time frame. However, the technique requires the use of ionising radiation and the contrast agents are not suitable for individuals with reduced renal function [5]. Additionally, the technique does not provide whole brain [5] or vessel specific information.

3.1.2 MR perfusion imaging with exogenous contrast agents

The most common MR perfusion imaging method performed with an exogenous contrast agent is dynamic susceptibility contrast (DSC) MRI, where a gadolinium based contrast agent is injected into a peripheral vein. Where it is present the contrast agent reduces the T_2^* value, so the bolus of contrast can be tracked by looking at local T_2^* changes; the size of which reflect the amount of contrast [23]. The tracking process results in a time curve of T_2^* changes that can be used to extract useful perfusion parameters, such as CBF and MTT.

DSC-MRI can be used in an acute setting and yields reproducible whole brain results. In an acute stroke setting, when combined with diffusion-weighted (DW) MRI the perfusion/diffusion mismatch is used to identify the ischaemic penumbra [15]. The penumbra is tissue at risk of infarction but which may be salvageable if re-perfused. It is possible to extract quantitative CBF values from DSC-MRI, although it can be difficult and prone to error [23]. DSC-MRI does not provide any vessel specific vascular territory information and gadolinium based contrast agents are associated with nephrogenic systemic fibrosis in subjects with poor renal function and are thus not suitable for all subjects [13].

3.1.3 MR perfusion imaging with arterial spin labelling

Arterial spin labelling (ASL), as described in Section 2.2, can be used to acquire perfusion information completely non-invasively. This is of great benefit in patient populations incompatible with the contrast agents used in x-ray DSA, CT and DSC-MRI. Similarly to DSC-MRI, the perfusion information provided by ASL can be used, with DW-MRI, to identify the ischaemic penumbra following acute stroke. Additionally, following an acute stroke, regions of high ASL signal – seen as hyperperfusion on CBF maps – have been taken as an indication of collateral flow. The increased signal is attributed to slower flow of blood in the collaterals [2]. There are also a range of vessel-selective ASL methods that indicate the feeding vessel supplying each brain region, and so both the presence and source of any collateral circulation. There are multiple ways of performing arterial spin

labelling perfusion imaging and adapting it to be vessel-selective. The major ASL approaches to perfusion imaging are outlined below, followed by an introduction to a range of vessel-selective methods (Section 3.1.4).

A range of pulsed ASL (PASL) sequences (Section 2.2.1) has been developed for perfusion imaging. The Echo-Planar MR Imaging and Signal Targeting with Alternating frequency (EPISTAR) sequence [66] originally labelled blood flowing into the imaging region in the labelling cycle and then 'labelled' above the imaging slice in the control condition. In this way the imaging slice would experience similar off-resonance radio-frequency (RF) effects during the control condition, but no labelled blood would flow into the region of interest. This technique was later adapted so the 'labelling' during the control acquisition was in the same site as the labelling plane but two 180° pulses, each with half the power of the labelling pulse, were applied. As a result blood in the labelling plane is left in a control condition whilst the imaging region is exposed to the same off-resonance RF effects [67].

Following EPISTAR a flow alternating inversion recovery (FAIR) sequence was developed [68, 69]. FAIR applies a non-selective inversion pulse to the entire brain – including both the labelling and imaging planes – in order to label inflowing blood. During the control acquisition a slice selective inversion pulse is applied to the imaging region so it experiences the same magnetisation transfer (MT) effects without generating any labelled inflowing blood.

The labelling bolus for PASL has an unknown temporal width. In order to quantify CBF from PASL acquisitions with only one post-labelling delay time modifications must be made to the sequence. QUantitative Imaging of Perfusion using a Single Subtraction II (QUIPPS II) [70] applies a slab-selective saturation pulse across the labelling slab to cut off the trailing edge of the labelled blood bolus. As a result the temporal width of the bolus is known and CBF can be quantified, as it is directly proportional to the ASL subtraction image (label minus control) signal once all of the labelled blood has reached the tissue.

It is also possible to use continuous ASL (CASL) for perfusion imaging (Section 2.2.2). More recently, however, pseudocontinuous ASL (PCASL) has become the preferred 'continuous' ASL method due to its greater ease of implementation on clinical scanners and

superior SNR to PASL (Section 2.2.3) [16]. The temporal width of the labelled blood bolus is known in PCASL and so CBF can be quantified more easily than with PASL.

3.1.4 Vessel-selective perfusion imaging with arterial spin labelling

Arterial spin labelling has been adapted in a number of ways to produce vessel specific information. These can be broken down into methods that label single vessels, label only the vessels present in a specific slab or label multiple vessels of interest at the same time in a chosen labelling plane.

Single vessel labelling

The labelling of a single vessel using ASL is performed either using localised RF pulses or a combination of gradients that localise one vessel. Davies and Jezzard [60] proposed pencil shaped RF pulses to excite only columns, or evenly shaped volumes, of spins in single arteries. Single artery selective methods that adjust the gradients applied during labelling have focussed on creating a disc-shaped labelling plane around a single vessel. This was initially performed by adding continuously modulating transverse gradients to a CASL pulse train [64]. These gradients precess around the axis of the artery of interest and, if the RF pulse frequency is modulated accordingly, only blood flowing through this artery will be labelled. In a similar way transverse gradients have been applied between the RF pulses in an unbalanced PCASL (Section 2.2.3) pulse train [59]. The direction of the gradients is gradually rotated to leave only a disc-shaped area within the labelling plane where the RF pulses act in a coherent manner and are thus able to invert the blood magnetisation. An analogous method for balanced PCASL (Section 2.2.3) uses pseudo-randomised transverse gradients of varying amplitude and direction to achieve a circular labelling spot [62]. Single artery selective methods are of use if the artery of interest is known. If information about more than one vessel is needed they become time inefficient and often suffer from lower labelling efficiency, and thus SNR, than non-selective ASL [59, 64].

Slab selective vessel labelling

Applying spatially selective RF pulses to invert the magnetisation in specific slabs labels

only blood in vessels in those regions. The right and left-hand circulation in the brain was selectively labelled by Eastwood *et al.* [71] before more complex selection of slabs enabled separation of signal from the right and left internal carotid arteries and posterior circulation in the brain [61, 63, 65]. Although some vessel specific information can be acquired using these methods, due to the tortuous nature of the arteries it can be difficult to ensure that only the vessel of interest lies within the inversion slab, especially when there are more than three or four vessels of interest. As a result these techniques have only been applied to label vessels in the neck.

Vessel-encoding

Vessel-encoded PCASL (VEPCASL), as described in Section 2.2.4, introduces additional transverse gradients into the PCASL pulse train to modulate the inversion efficiency in the labelling plane [30, 33]. This allows the blood flowing through multiple vessels of interest to be labelled concurrently. An encoding scheme specifies which vessels in the labelling plane are to be perfectly labelled, have a magnetisation value of -1, or controlled, a value of +1, during a given cycle. An encoding matrix is the mathematical formalism of an encoding scheme. Ideal encoding schemes are considered to be those whose encoding matrix has an SNR efficiency equal to one [30].

The modulation of the inversion efficiency in the labelling plane is considered to be an encoding function. The calculation of the frequency and phase of the encoding functions satisfying an encoding scheme requires knowledge of the vessel locations in the labelling plane. Typically these coordinates are found by acquiring a time-of-flight (TOF) angiogram, to both select the labelling plane and localise the vessels of interest. With the vessel locations it is possible to empirically choose a set of encoding functions that work relatively well in specific scenarios [37]. For example, in the case of four vessels an ideal encoding can be achieved if the vessels are approximately in a rectangular formation and perpendicular to the labelling plane. However, such a perfectly encoded situation is rarely encountered outside of specific regions in the neck. If there are more than four vessels, achieving ideal encodings becomes increasingly difficult. Computational methods that attempt to find the

most SNR-efficient encodings are also possible [72] but require extra time to calculate that may not be possible in a clinical setting.

VEPCASL can, however, be performed without prior knowledge of the vessel locations by randomly encoding – applying many random encoding functions to the labelling plane and combining the images to get vessel specific information [33]. The random technique removes the need for user selection of vessels but requires the acquisition of more encoding cycles than would otherwise be necessary and also reduces the average SNR efficiency. Planning-free VEPCASL is also possible, where a few fixed encodings are applied and vascular territory information is achieved using a voxel clustering method [73]. The SNR efficiency of this method is vulnerable to the geometry of the vessels being labelled and is only designed to label four vessels in the neck.

An additional confounding factor is the presence of any B_0 inhomogeneities in the labelling plane. Any off-resonance in the labelling plane will affect the applied encodings, either by reducing their SNR efficiency [30] or shifting them away from the vessels of interest [33]. Chapter 4 of this thesis details an alternative, automated, way of calculating the encoding functions for a given ideal encoding scheme. The result is a set of optimised encodings for any number of vessels of interest. Chapter 5 works on incorporating corrections for any off-resonance in the labelling plane into these encodings.

The determination of vascular territories following VEPCASL can be performed in various ways. The simplest method of estimating the contribution of different arteries to the signal in a given voxel is to invert (or pseudo-invert) the encoding matrix [30]. Perfect inversion of the blood magnetisation at the vessels of interest is not always possible though. A more accurate representation of the inversion of the magnetisation at each vessel location, rather than ± 1, can be found and incorporated into the encoding matrix to give a truer representation of the labelling taking place. Relative labelling efficiencies, of vessel-selective scans versus non-selective scans, can be calculated by subtraction of the relevant images and used to more accurately populate the encoding matrix [30]. Alternatively, estimates of the labelling efficiencies at the vessel locations can be determined from the true shape of the applied encoding functions [74].

It is possible to determine the vascular territories without the encoding matrix. Following random encoding, where the vessels were not identified beforehand [33] and the encodings performed in pairs, a cluster based method was used to assign a feeding vessel to each perfusion image voxel and to identify the approximate vessel locations. The theoretical ASL signal was generated for a range of possible vessel locations and frequency offsets for the known encoding functions of each pair of images. The pairs of acquired images were subtracted to produce images with perfusion information. For each voxel in the subtracted images the correlation coefficient with the theoretical signals for each possible vessel location and frequency offset were calculated. The maximum coefficient is used to identify the feeding vessel location and any frequency offsets in the labelling plane. Clusters of these maximum coefficients were manually identified as vessel locations and frequency offsets. An encoding matrix can be constructed from the estimated vessel locations and knowledge of the encoding functions. Matrix inversion analysis can then also be performed to ascertain any voxels fed by more than one vessel.

A final alternative is a Bayesian, maximum *a posteriori* (MAP), method that considers subsets of the encoding matrix to extract vessel specific information [74, 75]. Prior information from the planning of VEPCASL acquisitions, e.g. vessel locations and applied encodings, are incorporated into and inform the results of the analysis. The number of feeding arteries for any given voxel is restricted to increase SNR efficiency and reduce the number of necessary encoding cycles. By looking at subsets of the encoding matrix this technique can deal with poorly conditioned encoding matrices without significant loss of SNR and the MAP method employed ensures computation times remain acceptable (on the order of 1-2 minutes for four vessels).

3.2 Angiography

Angiography provides important information on the cerebral vasculature. Angiograms in general are capable of providing information on vessel structure and collateral flow, by indicating if there is any cross linkage of vessels across the brain. However, it is only

vessel-selective methods that are capable of unambiguously identifying the feeding vessels of any lesions, to aid in treatment planning, and collateral circulation, of interest in the diagnosis and treatment of stroke [2]. Additionally, certain angiographic methods yield knowledge on the flow dynamics in the vasculature. Dynamic angiographic data offers insight into vessel filling, which can help distinguish arterial and venous signals, and transit times of blood through the vasculature, changes in which may be indicative of disease [76]. A variety of methods have been developed to investigate blood vessels in the brain, the most common are described below. Magnetic resonance based methods are separated according to whether they require an exogenous or endogenous contrast agent and, when blood is the endogenous agent, whether arterial spin labelling is the technique used.

3.2.1 Non-magnetic resonance based angiography

The gold standard for imaging the vasculature in the brain and diagnosing cerebrovascular disease is x-ray digital subtraction angiography (DSA). X-ray DSA involves the subtraction of an x-ray image acquired before injection of a radio-opaque contrast agent and one taken afterwards, leaving only signal from the agent in the vascular network [22]. Catheter angiography allows arteries to be individually injected with contrast agent and provide angiograms of networks fed only by specific arteries [77]. The acquired images can be two- or three-dimensional [10] and vessel specific injections can provide information on the feeding vessels of lesions or collateral circulation.

X-ray DSA provides dynamic angiograms with high temporal and spatial resolution [77]. However, the technique comes with certain associated risks. Aside from the use of ionising radiation, x-ray DSA can also result in neurological complications from catheter insertion [5]. Although the complication rate is low in the general population [78] it has been shown to increase substantially in subjects who have a history of vasculopathy [14] and the complications can be very serious, even resulting in death.

CT angiography (CTA), as with CT perfusion imaging, involves the injection of an iodinated contrast agent [79]. It is considered less invasive than x-ray DSA, as the agent is

most commonly administered intravenously. In general CTA generates angiograms with very good spatial resolution quickly [80] and three-dimensional (3D) images can be reconstructed through maximum intensity projection (MIP) or volume rendering techniques [81].

CTA can be more readily available than MR based angiography and, in terms of image quality, can be close to x-ray DSA [5]. CT with a contrast agent is particularly good at identifying haemorrhages [7] but, as mentioned in Section 3.1.1, involves ionising radiation and the use of contrast agents not suitable for all subjects. It is possible to acquire dynamic angiograms in the brain with CTA [82], although the temporal resolution is somewhat limited. However, although intra-arterial injection of contrast agent has been shown to assist in imaging certain tumours and identifying their feeding vessels [83], vessel specific information on the cerebral vasculature is not generally available.

3.2.2 MR angiography with exogenous contrast agents

Magnetic resonance angiography (MRA) is becoming a viable alternative to traditional angiographic methods and so increasingly popular as a clinical tool. Contrast-enhanced MRA (CE MRA) typically involves the injection of a gadolinium based, T_1-shortening contrast agent into the bloodstream, followed by an acquisition scheme that produces images with very bright blood signal and dark static tissue [84]. In most scenarios CE MRA agrees well with both x-ray DSA and CTA [5].

There are a variety of time-resolved CE MRA techniques, of which the time-resolved imaging of contrast kinetics (TRICKS) method is the most prevalent [85]. In certain scenarios CE MRA is thought to be more accurate than non-contrast enhanced MRA [5], although the spatial resolution is very dependent on the chosen technique [80]. Spatial and temporal resolution are often restricted due to the requirement to image the first passage of the bolus, limiting the amount of imaging data that can be acquired. Two- and three-dimensional CE MRA images can be obtained [86]. However, as the contrast agent is administered intravenously it is not possible to acquire vessel specific information to identify the feeding

vessel(s) of lesions or collateral flow. Again, as highlighted in Section 3.1.2, gadolinium based contrast agents have been associated with nephrogenic systemic fibrosis in patients with renal dysfunction [13].

3.2.3 MR angiography with endogenous contrast agents

Non-contrast enhanced magnetic resonance angiography, or MRA using endogenous contrast, is becoming progressively more widespread, as images of similar quality to CE MRA can now be acquired [87]. There are no complications or costs associated with a contrast agent and it is possible to do other types of MR acquisitions without fear of signal contamination by an injected contrast agent. There is a range of techniques that create angiographic contrast without an exogenous agent, of which the most well known are outlined below.

The most common MRA method using an endogenous contrast agent is time-of-flight (TOF) angiography. TOF imaging works by repeatedly exciting the magnetisation in the imaging region using a relatively short TR and large flip angle to saturate its signal; inflowing blood signal is unsaturated and so blood appears bright [87] (Figure 3.1). Two- and three-dimensional imaging is possible with TOF angiography and the cerebral vasculature can be observed in a high level of detail, although vessel-selective information cannot be obtained. In order to prevent significant saturation of the blood signal as it flows through the imaging region the repetition time of TOF sequences is typically longer than that used for CE MRA, resulting in a longer overall acquisition time.

Phase-contrast (PC) MRA applies gradients that change the phase of moving spins but leaves static tissue unchanged. In this way flow-sensitive phase images can be acquired [87], so the dynamics of blood flow in the cerebral vasculature can be imaged. The phase difference due to the additional gradients in PC MRA is proportional to the absolute blood velocity in each voxel along the applied gradient direction. Multiple acquisitions, with different gradient directions applied, generate flow direction information. Two- and three-dimensional acquisitions are possible and knowledge of flow direction in vessels of interest could potentially indicate the feeding vessels for any cerebral collateral circulation or in

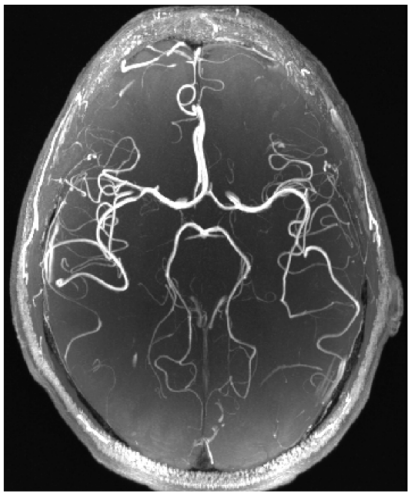


Figure 3.1: An axial 3D TOF maximum intensity projection image of the circle of Willis in a healthy subject, acquired at 3 T

fact lesions. PC MRA, however, has relatively long acquisition times [87] and sensitivity to partial volume effects and pulsatile or non-uniform blood flow, which can lead to image artefacts if not appropriately accounted for [88]. For MRA, the combination of phase contrast imaging and a Vastly undersampled Isotropic Projection Reconstruction (VIPR) [89] has been suggested. VIPR can use the sparse nature of PC images to provide high quality 3D angiograms in a reduced acquisition time.

3.2.4 MR angiography with arterial spin labelling

ASL, combined with a range of readout schemes (Section 2.4), can be used to acquire non-vessel-selective dynamic cerebral angiograms. As with perfusion imaging, a range of ASL techniques can be used for MRA. Dynamic ASL [90], for example, combines FAIR with Fast Low-Angle Shot (FLASH) Look-Locker sampling to acquire time-resolved angiograms that may be able to detect small collateral vessels with low flow not visible to TOF MRA. PCASL, meanwhile, has been used in conjunction with a 3D spoiled gradient echo (SPGR) readout to produce high quality dynamic angiograms [91]. Other time-resolved non-contrast enhanced MRA methods combine ASL with 3D balanced steady-state free precession (bSSFP) readouts, to achieve both high spatial and temporal resolution within the cerebral vasculature [38, 45, 92–94].

PCASL and PASL have been combined into a hybrid magnetisation preparation before being coupled with a variety of sampling strategies to yield dynamic angiograms. This has included 3D undersampled radial acquisition strategies with both spoiled gradient echo (SPGR) [95] and bSSFP readouts [39].

3.2.5 Vessel-selective angiography with arterial spin labelling

Section 3.1.4 describes a range of vessel-selective ASL techniques that can also be used to acquire cerebral angiograms.

Single vessel selection with PCASL, where the gradients are manipulated to leave only a disc-shaped labelling plane around the artery of interest [59], has been combined with a bSSFP readout scheme [96] to produce vessel-selective angiograms. Similarly, an alternative single artery selective technique [62] has recently been combined with a keyhole readout to acquire 3D time-resolved vessel-selective angiograms, labelling three arteries [97]. As for perfusion imaging, these techniques are of benefit when the vessel of interest is known. However, they are not SNR or time-efficient if information about multiple vessels is required. Slab-selective labelling schemes for ASL have also been used to produce dynamic angiograms of the circle of Willis, however they can only provide vessel specific information on a limited number of arteries [98, 99].

VEPCASL is capable of acquiring angiograms of the entire cerebral vasculature, with vessel specific information, without a loss in SNR efficiency as compared to PCASL [30]. Previous works combining VEPCASL with an angiographic readout have used both SPGR [8] and bSSFP readout schemes [100]. Vessel specific information can be separated out using a MAP analysis [75] and a method to quantify blood flow in different arteries with this type of data has also been developed [37]. Acquisitions of dynamic data with VEPCASL have to date had relatively long scan times and/or been limited to two dimensions. To become more clinically viable the acquisition of vessel-selective angiograms needs to be performed in a short time frame, whilst still providing images of high enough quality. Three-dimensional angiograms can further offer analysis of the cerebral vasculature from multiple directions,

to aid the precision of patient diagnosis and treatment [9, 10]. Chapter 6 of this thesis investigates the potential for accelerating acquisition of 2D dynamic VEPCASL angiograms. Chapter 7 meanwhile assesses the possibility of 3D dynamic VEPCASL angiograms.

3.3 Conclusions

Perfusion imaging and angiography in the brain are performed in a myriad of different ways. The work of this thesis, as referenced at the end of Sections 3.1 and 3.2, focuses on the optimisation and development of non-invasive vessel-selective techniques. In particular, the development and automation of ASL techniques to acquire vessel-selective information for any number of vessels, regardless of the presence of B_0 field inhomogeneities (Chapters 4 and 5) and the optimisation of angiographic techniques (Chapters 6 and 7) to increase their clinical viability and desirability. In this way knowledge of the CBF and vascular morphology in the brain can be provided alongside information on collateral flow or blood supply to lesions. An increased variety of diagnostic information would therefore be available.

Chapter 4

An optimised encoding scheme for planning vessel-encoded arterial spin labelling

Perfusion imaging and angiography that provide vessel specific information can be performed in numerous ways across different imaging modalities (Chapter 3). Vessel-encoded pseudocontinuous arterial spin labelling (VEPCASL) offers a completely non-invasive way of acquiring vessel specific information about the entire cerebral vasculature and its perfusion territories. It can be used to identify collateral circulation in the brain, which improves patient outcomes following a stroke [2], and identify feeding arteries to vascular lesions or tumours.

As outlined in Section 3.1.4, there is a range of options for choosing the encoding scheme for a set of vessels. However, there is currently no method for automatically and rapidly calculating a minimal number of SNR-efficient encodings for non-regular arrangements of more than three vessels. In this chapter a rapid optimised encoding scheme (OES) that automates the choice of SNR-efficient encodings, regardless of the number or arrangement of vessels, is described. This work has been published[1].

[1] Berry, E. S. K, Jezzard, P. and Okell, T. W., An optimized encoding scheme for planning vessel-encoded pseudocontinuous arterial spin labeling, Magnetic Resonance in Medicine, 74:1248-1256, 2015

4.1 Labelling efficiency of unipolar VEPCASL

The optimised encoding scheme described in this chapter has been developed for use with unipolar VEPCASL [33]. As described in Section 2.2.4, the transverse gradient 'blips' applied in between the radio-frequency (RF) pulses in the VEPCASL pulse train are all in the same direction. The inversion profile of the magnetisation across the labelling plane, when a control and label encoding are subtracted, is well represented by the sum of three Fourier coefficients [33]:

$$\Delta M_z = 2.092\cos(\theta) - 0.322\cos(3\theta) + 0.053\cos(5\theta) \tag{4.1}$$

where ΔM_z is the difference between the longitudinal magnetisation (M_z) in the label and control cycles. θ refers to the phase across the labelling plane, induced by the VEPCASL pulse train transverse gradients; the phase corresponds to spatial locations in the labelling plane. This equation was reached following Bloch simulations of the magnetisation inversion for a range of velocities, whilst ignoring T_1 decay, and fitting Fourier coefficients to the resulting subtraction curve [33].

In order to more accurately assess the unipolar VEPCASL labelling efficiency, for the specific sequence implementation described in this chapter, the effect of the sequence on the magnetisation of blood flowing through the labelling plane was simulated using the Bloch equations and an effective field method (Section 2.1.3). The magnetisation is modelled as a single spin. The inversion profile of the magnetisation, for phase shifts between $\pm\pi$, was simulated for a range velocities around a typical carotid artery blood velocity of 0.3 m/s [101]. The velocity of the blood has an effect on the shape of the encoding function, as the amount the spins in the blood move between each RF pulse will be affected. Laminar flow was assumed and its effect on the shape of the encoding function taken into account by taking a weighted average over the range of tested velocities [29]. The VEPCASL pulse train is described fully in Section 2.2.4. The parameters and default values of the simulated gradients and RF pulses are similar to those in Okell *et al.* [8] (Table 4.1). T_1 and T_2 values were taken from a study that calculated relaxation times in human blood at a field strength of 3 Tesla [102].

VEPCASL pulse train parameters	
RF pulse type	Gaussian
RF flip angle	20°
RF duration	600 μs
RF separation (peak to peak)	1000 μs
Mean labelling gradient	0.8 mT/m
Gradient amplitude during RF pulses	6 mT/m
Time (dt) between simulated points	10 μs
T_1	1.932 s
T_2	0.275 s

Table 4.1: Parameters used in Bloch equation simulations of the magnetisation inversion during a VEPCASL pulse train.

Figure 4.1 shows the inversion profile of the longitudinal magnetisation of the sequence for a range of average blood velocities. The curves have been corrected for T_1 decay to make them more comparable. The correction applies to the time between the modelled spin crossing the labelling plane and the end of the simulation and normalises the signal to the case of perfect inversion. When perfectly labelled M_z would ideally have a value of -1, and a value of +1 when perfectly controlled.

A typical blood velocity in the carotids is around 0.3 m/s [101, 103]. Figure 4.2 shows the magnetisation inversion profile, following the subtraction of control and label encodings, for the simulated magnetisation (v = 0.3 m/s), the sum of Fourier coefficients [33] and a simple sinusoid. The root mean square difference between the simulated magnetisation inversion curve and the Fourier coefficients is 0.14, and 0.15 between the simulation and a simple sinusoid. The root mean square difference between the Fourier coefficients and the sinusoid is 0.24.

The differences between the simulation results and both the sum of Fourier coefficients and a perfect sinusoid are relatively small. The method developed for calculating encodings, as described in the following section, approximates encoding functions to sinusoids in order to be able to utilise the Fourier transform. The simulations performed here validate this approximation and, as a result, ensure the method remains computationally simple. The simulated inversion efficiency curve has also been incorporated into the analysis of unipolar VEPCASL data for the remainder of this thesis.

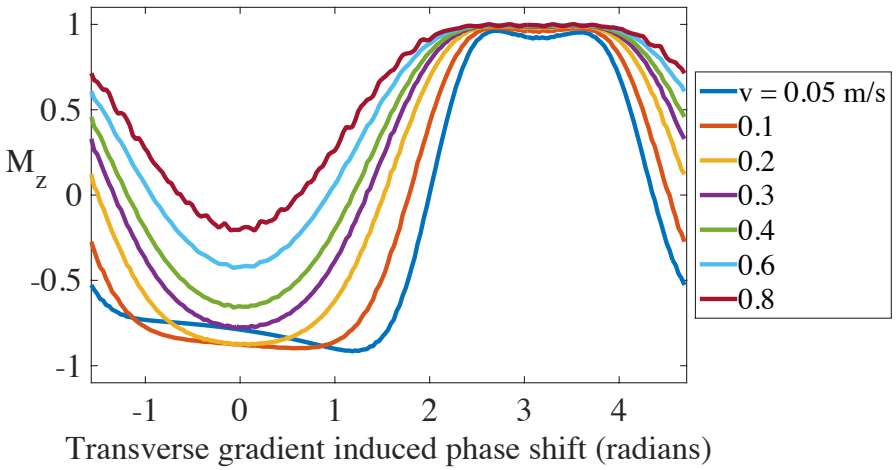


Figure 4.1: Inversion profile of the magnetisation for unipolar VEPCASL across a range of velocities and phase shifts. Phase shifts correspond to spatial locations in the labelling plane.

4.2 Theory

4.2.1 Encoding matrices

The encoding matrix is the mathematical description of an encoding scheme. The columns describe the expected state (between ± 1) of each artery of interest, and static tissue, for every cycle – or row in the matrix – of the encoding scheme. The signal within each voxel is given as:

$$\boldsymbol{y} = \boldsymbol{A} \cdot \boldsymbol{x} \tag{4.2}$$

where $\boldsymbol{y}$ is the vector of measured signal intensities for a given voxel, each component is the signal from a different encoding cycle, $\boldsymbol{A}$ is the encoding matrix and $\boldsymbol{x}$ is the, unknown, vector describing the signal contributions from each vessel plus static tissue [30]. Encoding matrices are preferably full rank and have a low condition number. An example ideal encoding matrix for four vessels in the neck, described by Okell *et al.* [37], is shown below. This particular scheme acquires complementary pairs of encodings that allow the images to be subtracted from each other to give some vascular territory information without further analysis. The columns describe (from left to right) the label/control state of the right internal carotid artery, left internal carotid artery, right vertebral artery, left vertebral artery and static tissue, respectively, for each encoding (or row).

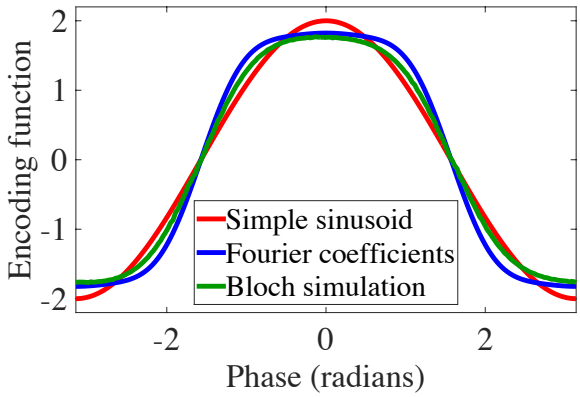


Figure 4.2: A sinusoidal function, the theoretical sum of Fourier coefficients model of unipolar VEPCASL [33] and the inversion profile of the magnetisation simulated using the Bloch equations. The functions show the magnetisation inversion curves following subtraction of control and label encodings.

$$\boldsymbol{A} = \begin{bmatrix} -1 & -1 & -1 & -1 & 1 \\ 1 & 1 & 1 & 1 & 1 \\ -1 & 1 & -1 & 1 & 1 \\ 1 & -1 & 1 & -1 & 1 \\ -1 & -1 & 1 & 1 & 1 \\ 1 & 1 & -1 & -1 & 1 \\ -1 & 1 & 1 & -1 & 1 \\ 1 & -1 & -1 & 1 & 1 \end{bmatrix}$$

The contributions of signal from each artery, and static tissue, in a voxel can be estimated by (pseudo) inverting the encoding matrix and applying this inversion to the measured signals, i.e. $\boldsymbol{x} = \boldsymbol{A}^{+} \cdot \boldsymbol{y}$, where $\boldsymbol{A}^{+}$ is the pseudo-inverted encoding matrix.

Ideal encoding matrices are those whose SNR efficiency is equal to one for all vessels [30], which requires the arteries to be perfectly tagged (-1) and controlled (+1) an equal number of times. The SNR efficiency of an encoding matrix can be calculated using Equation 4.3 [30]:

$$E_i = \frac{SNR_{encoded}}{SNR_{averaging}} = \frac{1/\sqrt{\Sigma_j \boldsymbol{A}_{i,j}^{+2}}}{\sqrt{N}} = \frac{1}{\sqrt{N\Sigma_j \boldsymbol{A}_{i,j}^{+2}}} \tag{4.3}$$

E_i is the SNR efficiency of the ith vessel, N is the number of encodings, j is a given encoding.

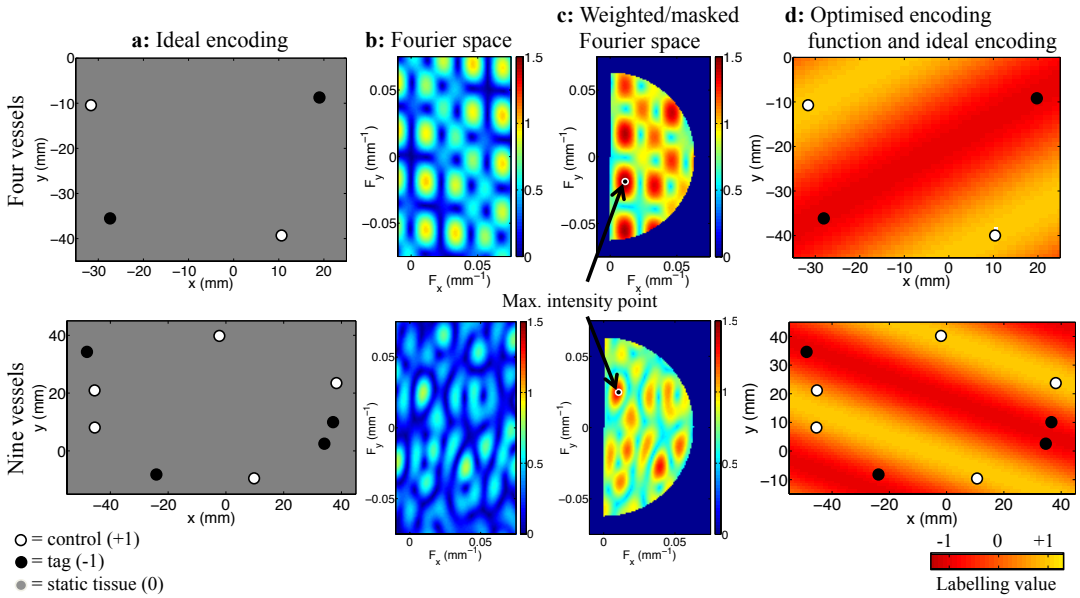


Figure 4.3: OES method for four vessels (top row), representative of the main brain-feeding arteries in the neck, and for nine vessels (bottom row), similar to arteries above the circle of Willis. **a**: Images of ideally encoded vessels of interest, static tissue is set to zero. **b**: Fourier transforms of the zero-padded images. **c**: Weighted and masked Fourier spaces, with the maximum intensity points shown with an arrow. **d**: Optimised encoding functions overlaid on to the ideal encodings.

The columns of matrix $\boldsymbol{A}$ have come from a Hadamard matrix – such a matrix will always have an SNR efficiency of one [30]. The order of a Hadamard matrix must be 1, 2 or a multiple of 4. When the number of vessels of interest (plus static tissue) does not match the order of a possible Hadamard matrix then ideal encodings can be composed of the columns of the Hadamard matrix closest in size to (but greater than) the number of vessels plus one. Consequently, there may be more encodings than are strictly necessary to extract the information about all the vessels. However, these extra encodings give the overall encoding scheme the greatest SNR efficiency.

4.2.2 Generating an optimised encoding scheme

The optimised encoding scheme (OES) method automates the choice of the encoding function used to tag/control the arteries of interest in a given VEPCASL cycle. It relies on defining an ideal encoding scheme and finding real encodings that match these as closely

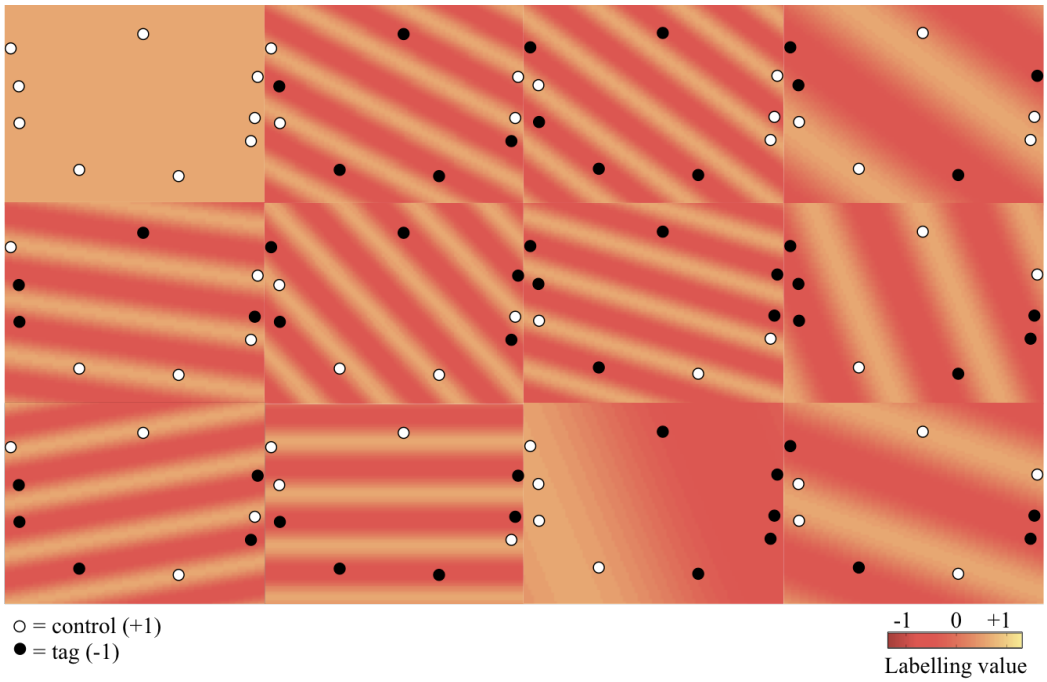


Figure 4.4: All optimised encodings calculated for the ideal Hadamard encodings of a set of nine vessels.

as possible. The method must be run for each cycle of the ideal encoding scheme separately and is structured as follows:

1. Construct an "image" of the vessel locations. Each vessel is represented by ± 1, depending on the ideal encoding (Figure 4.3.a)
2. Zero-pad this "image"
3. Take its Fourier transform (Figure 4.3.b)
4. Weight (Equation 4.4) and mask the resulting Fourier space to up-weight lower spatial frequencies (Figure 4.3.c)
5. Find the maximum intensity in this weighted Fourier space (Figure 4.3.c)

The maximum intensity point in the weighted Fourier space provides the spatial frequency and phase of the optimised encoding function (Figure 4.3.d). Figure 4.4 shows the optimised encodings for each ideal encoding of the nine vessels in the bottom row of Figure 4.3.

The algorithm constructs the image of the vessels from the manual input of the vessel locations. The vessels, represented by ± 1, are placed in a matrix of zeros, at positions corresponding to their physical Cartesian coordinates within the labelling plane. Zero-padding the image increases resolution in Fourier space, allowing the optimal spatial frequency to be identified more precisely. The Fourier transform was chosen for use in this method as it is a close approximation to the true encoding function (Section 4.1) and allows for a mathematically streamlined and computationally fast process for calculating the encodings through Fast Fourier transform algorithms.

Up-weighting lower spatial frequencies while masking higher ones makes the method more robust to gross subject motion. If a chosen encoding function has a low spatial frequency then, should a subject move, the vessels of interest remain close to the desired encoding. The weighting function is present to ensure the algorithm has a tendency to choose lower spatial frequencies where there is a range of encoding functions that give a good match to the desired encoding. Note there is no lower limit on the choice of spatial frequency, since encoding functions with wavelengths much larger than the separation of the vessels cannot give a good match to the desired encoding and will therefore be excluded by the algorithm.

If the vessels of interest are close together a higher spatial frequency is required to efficiently differentiate them. However, if the spatial frequency is too high even a small amount of movement could shift a vessel from a label to a control location, leading to considerable deviation from the desired encoding. In addition, at very high spatial frequencies there may be considerable variation in inversion efficiency across the diameter of a vessel, thereby reducing the average inversion efficiency and causing further deviations from the expected encoding. Consequently the highest frequency encodings are masked out.

The radius of the Fourier space mask is set so the wavelengths of the chosen encoding functions are at least four times the maximum predicted subject motion. The subject motion is chosen according to the population being scanned (Section 4.3). This helps to ensure that, should a subject move, an artery that was intended to be in the tag condition will not be moved into a control condition and vice versa. The mask radius gives control over

the trade-off between SNR efficiency and motion robustness, and can be tailored for each subject group. The mask also removes the redundant symmetric half of Fourier space.

In practice, before the maximum intensity point is identified, the absolute value of the Fourier space is taken, normalised to its maximum value and then weightings are added. The weighting function is based on the position of each point in the Fourier space. For a given point at a distance f from the centre of the Fourier space the weighting w is:

$$w = \left(\frac{1 - {}^{f}/_{f_{max}}}{2} \right) \tag{4.4}$$

where f_{max} is the maximum possible distance of any point from the centre. The coordinates of the maximum intensity point in the normalised weighted and masked Fourier space give the spatial frequency and direction of the optimum encoding function, with phase extracted from the same point in the un-normalised, un-weighted Fourier space.

The OES method implicitly assumes that the periodic labelling efficiency in VEPCASL is sinusoidal. The root mean squared difference between the simulated inversion efficiency of unipolar VEPCASL and a perfect sinusoid is 0.15 and the differences between the two functions at their maxima and minima are small (Figure 4.2), so errors resulting from this assumption are likely to be minimal. However, as mentioned earlier, the inversion efficiency curve simulated using the Bloch equations (Section 4.1) has been incorporated into post-processing of all VEPCASL data, allowing the resulting images to be better decoded into vessel specific maps.

4.3 Methods of evaluation

The OES method was evaluated against two existing encoding methods, standard encoding for four vessels in the neck [37] and random encoding [33], through simulations and scans of healthy volunteers.

Standard method

When labelling the four main brain-feeding arteries in the neck encoding functions calculated as in [37] were used:

- Left-right (according to the magnet coordinate system) encodings tag/control the internal carotid arteries
- Anterior-posterior tag/control at the average internal carotid/vertebral artery positions
- Diagonal encoding tags the right carotid and left vertebral arteries whilst controlling at the average location of the other two vessels, and vice versa.

Random method

The random encodings were taken from those generated by Wong and Guo [33], so a direct comparison can be drawn between the OES method and this existing method. Two non-selective tag/control pairs of encodings were acquired along with 58 pairs of random encodings taken from [33]. A pair refers to the same encoding, phase shifted by 180° (so that a tag location becomes a control location and vice versa).

OES method

When considering four vessels the ideal encoding matrix described by Okell *et al.* [37] is used so the OES and "standard" methods can be directly compared. When considering more than four vessels the columns of a Hadamard matrix are used as the ideal vessel-encoding matrix. The calculations of the optimal encodings were performed in Matlab® (Mathworks™, Natick, Massachusetts, USA). The calculation time for a set of encodings using a standard laptop is short: less than two seconds for four vessels and less than three seconds for nine.

For all OES calculations the image of the vessels was zero-padded to a 1024 x 1024 matrix to give accurate spatial frequencies and phases without unnecessarily increasing the computation time. The expected maximum subject motion was set to 4 mm in all cases, as the predicted motion of healthy volunteers is low. This value results in a Fourier space mask that allows some higher spatial frequencies to be chosen. Consequently, it is possible to differentiate between vessels close together, as would be expected in vessel configurations above the circle of Willis.

4.3.1 Simulations

Simulations were performed in Matlab to test the efficacy of the OES method given variability in the geometry of vessels of interest. Rotations and shifts of vessel geometries were tested. Encoding values at the vessel locations were drawn from the inversion efficiency curve as simulated in Section 4.1 (assuming an average blood velocity of 0.3 m/s), to give a more accurate representation of the encoding matrices. The SNR efficiency was averaged across all vessels to simplify comparison between the different encoding methods.

Four vessel rotation and shifts

Firstly, four vessels, in an arrangement typical of the main brain-feeding arteries in the neck set in a Cartesian coordinate system, were rotated in intervals of 2° up to 90° about the origin. Secondly, each vessel location in this typical arrangement was perturbed by a random distance and direction. The perturbations were chosen randomly from normal distributions (mean = 0) with increasing standard deviation (from 2 to 10 mm).

Above the circle of Willis vessel rotation and shifts

In the same way as for four vessels, a set of nine vessels, representative of the cerebral arteries above the circle of Willis, was rotated in intervals of 2° up to 90° about the origin. Each vessel in this set of nine was then perturbed by a random distance and direction. The perturbations were chosen randomly from normal distributions (mean = 0) with increasing standard deviation (from 2 to 10 mm).

The four vessel simulations compared the SNR efficiencies of the encodings produced by the OES, standard and random methods. The nine vessel simulations only involved the OES and random methods, as there is currently no automatic method for calculating optimal encodings for more than four vessels. All simulations were compared to the theoretical SNR efficiency of the random encoding scheme [33].

4.3.2 Subject scans

Scans were performed on healthy subjects, scanned under a technical development protocol agreed with local ethics and institutional committees. Data were acquired on a 3T TIM

Verio system (Siemens Healthcare, Erlangen, Germany) with a 32-channel head coil. A 3D multislab time-of-flight angiography sequence was performed at the start of each scan to allow selection of a labelling plane and localisation of vessels.

When labelling the four main brain-feeding arteries in the neck, the OES method was compared with the standard and random encoding methods in five healthy subjects (two female, 23-35 years, mean age 26.8 years). The order of application of the different methods was randomised across subjects. To assess whether the OES method yields improved vascular territory images, regardless of the arrangement of vessels, two scenarios were tested:

1. Subject normally aligned in the scanner
2. Subject's head rotated to the left or right ($\sim$10-20°).

When considering more than four vessels above the circle of Willis the OES and random methods were compared for a single subject, to assess whether the OES method leads to more accurate identification of vascular territories.

The VEPCASL labelling scheme was combined with a single-shot echo planar readout to acquire perfusion data. The scanning parameters were the same as those used by Okell *et al.* [37]: tag duration = 1.4 s, voxel size = 3.4 x 3.4 x 5 mm, number of measurements = 120, except a single post-labelling delay of one second was used. The total number of measurements was kept the same for all types of encodings and all numbers of vessels to ensure a fair comparison. Consequently the acquisition time for each type of encoding was the same: 7.18 minutes.

In certain cases images of the encoding functions in the labelling plane were acquired. The readout region was reduced to a single slice and moved to the labelling plane itself. A single measurement was acquired for each encoding, with tag duration = 300 ms, post-labelling delay = 16 ms and repetition time = 500 ms to allow some T_1 recovery. At a "tag" location within the labelling plane static spins experience repeated RF pulses with the same phase leading to a saturated, and therefore low, tissue signal. At a "control" location static tissue experiences RF pulses of alternating sign and therefore a relatively

high signal. This allowed the location of the label/control troughs/peaks of the function to be visually assessed.

4.3.3 Subject scans analysis

Analysis was performed using both encoding matrix inversion (MI) and Bayesian maximum *a posteriori* (MAP) analysis [75] (Section 3.1.4). Images were averaged across all repeats and two different comparisons were made.

Mean SNR of the vascular territory maps

In the vascular territory images obtained through matrix inversion and MAP analysis, voxels considered to be within grey matter were used to calculate the SNR across vascular territories. Grey matter masks applied to the images were created using partial volume maps for each subject, obtained with the FMRIB Software Library tool FAST from T_1 weighted structural images [104]. These grey matter masks were registered to the VEPCASL space using a linear registration [105] and thresholded with a value of 0.5. The SNR for each vascular territory was calculated separately, using only signal voxels in which the given artery was the dominant feeder. The signal across all slices was included. The noise was taken as the standard deviation of a background region-of-interest (ROI) in the unmasked images. The SNR was averaged across all subjects and compared for the three encoding methods. Parallel imaging was used in the acquisition of the perfusion data. As such the choice of a background ROI outside of the regions used to calculate signal will also include noise terms resulting from the parallel imaging and its reconstruction process. However, the SNR values are primarily for internal comparison between the scenarios tested here, as opposed to an absolute measure of SNR.

Relative labelling efficiency maps

When four vessels were encoded relative labelling efficiency maps were calculated by normalising the selectively labelled pairs of images to the non-selectively labelled images, identical to the beta parameter in [30]:

$$\beta = \frac{selective\ tag\ pair\ subtraction}{non\text{-}selective\ tag\ pair\ subtraction} \times mask \tag{4.5}$$

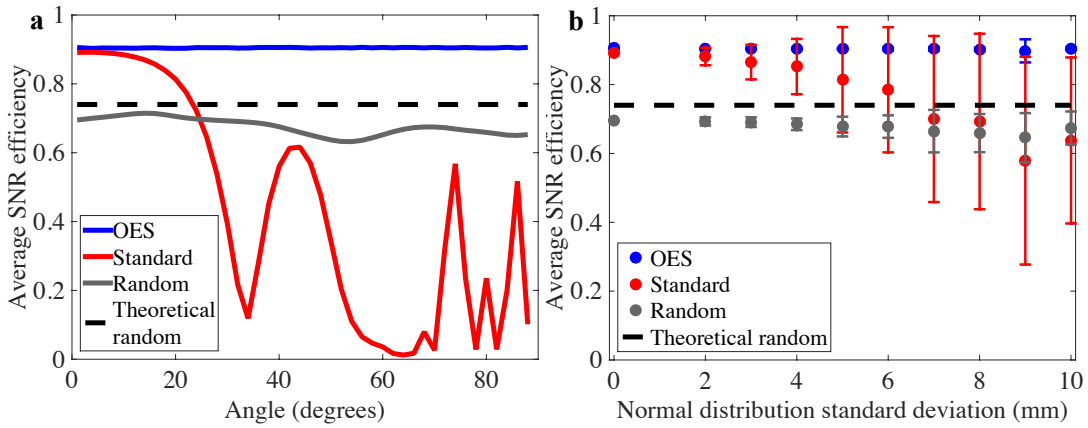


Figure 4.5: Simulated average SNR efficiencies in different scenarios: **a**: four vessels rotated through various angles; **b**: four vessels perturbed by random shifts of increasing magnitude.

The selective tag pair subtraction is, for example, the right-labelled image minus the left-labelled. The non-selective pair subtraction is the non-selective control minus the non-selective tag image. The mask is a rough grey matter mask calculated by thresholding the non-selective subtraction image. Only voxels with signal above the 99^{th} percentile divided by two were retained. The resulting images show how efficiently the vessels were encoded during each VEPCASL cycle.

4.4 Results

4.4.1 Simulations

Four vessel rotation

As the four vessels are rotated, the average SNR efficiency of the OES encodings remains close to the ideal value of one, mean $\pm$ s.d. = 0.905 $\pm$ 0.001 (Figure 4.5.a). The average SNR efficiency of the standard encodings shifts away from the ideal after about a 20° rotation, with a mean $\pm$ s.d. = 0.429 $\pm$ 0.323. The average SNR efficiency of the random encodings is below that of the OES method, mean $\pm$ s.d. = 0.676 $\pm$ 0.025, and close to the theoretical optimal SNR efficiency of random encoding for well-separated vessels (0.74). According to a Mann-Whitney U-test the SNR efficiency of the OES encodings

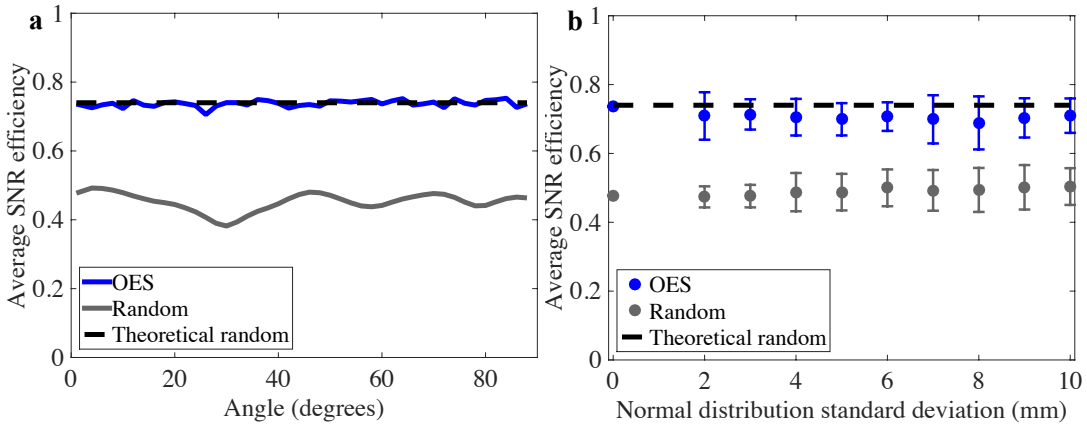


Figure 4.6: Simulated average SNR efficiencies in different scenarios: **a**: nine vessels rotated through various angles; **b**: nine vessels perturbed by random shifts of increasing magnitude. Note that there is no standard method for encoding this number of vessels.

is significantly greater than both the standard ($P \approx 10^{-16}$) and random ($P \approx 10^{-16}$) encodings. Similarly the random encodings have a significantly greater SNR efficiency than standard encoding ($P \approx 10^{-4}$).

Four vessel shifts

As the size of the vessel location perturbation increases, the average SNR efficiency of the OES encodings remains close to the ideal value of one, mean $\pm$ s.d. = 0.903 $\pm$ 0.002. The average SNR efficiency of the standard encodings decreases and becomes more variable, mean $\pm$ s.d. = 0.770 $\pm$ 0.111 (Figure 4.5.b). Once again the average SNR efficiency of the random encodings is below that of the OES method and close to the theoretical value, mean $\pm$ s.d. = 0.676 $\pm$ 0.016. According to a Mann-Whitney U-test the SNR efficiency of the OES encodings is significantly greater than both the standard ($P \approx 10^{-4}$) and random ($P \approx 10^{-4}$) encodings and the SNR efficiency of the standard encodings is significantly greater than that of random encoding ($P = 0.04$).

Above the circle of Willis vessel rotation

As the nine vessels are rotated, the average SNR efficiency of the OES encodings remains close to the theoretical optimal SNR efficiency of random encoding, mean $\pm$ s.d. = 0.738 $\pm$ 0.009 (Figure 4.6.a), and remains higher than random encoding. The average SNR efficiency of the random encodings is 0.452 $\pm$ 0.026. According to a Mann-Whitney U-test

the SNR efficiency of the OES encodings is significantly greater than random encodings ($P \approx 10^{-16}$).

Above the circle of Willis vessel shifts

The average SNR efficiency of OES encodings is greater than random encodings in all cases. Mean SNR efficiency $\pm$ s.d. = 0.707 $\pm$ 0.012 for OES encodings and 0.489 $\pm$ 0.011 for random encodings (Figure 4.6.b). The SNR efficiency of the two different encoding methods is significantly different ($P \approx 10^{-4}$), according to a Mann-Whitney U-test. The SNR efficiency of the OES encodings for this number of vessels is on average lower than for four vessels. The theoretical SNR efficiency of random encoding exceeds the simulated values for random encoding in this scenario. OES and random encoding achieve the same SNR efficiency whether the above the circle of Willis vessels of interest are shifted or rotated.

Regardless of the number of vessels, the average SNR efficiency of the OES encodings was, on average, approximately 32% greater than for random encodings. Additionally, the minimum and maximum SNR efficiencies across all vessels for all the simulations follow the same trend as the average SNR efficiency.

4.4.2 Subject scans: four vessels

For all subjects in both straight and rotated positions the vascular territories were visually well separated using both the MAP and matrix inversion analyses.

Mean SNR of the vascular territory images

For images produced using the MI analysis the OES method maintained a similar mean SNR of the vascular territory images regardless of the alignment of the subject within the magnet. The mean SNR of the OES images was significantly higher, according to a paired t-test, than images acquired using the random method when the subjects were aligned ($P = 0.006$), and than the standard method ($P = 0.043$) when the subjects were rotated (Figure 4.7). The SNR efficiency of the standard method was significantly greater than random encoding in the aligned case ($P = 0.08$).

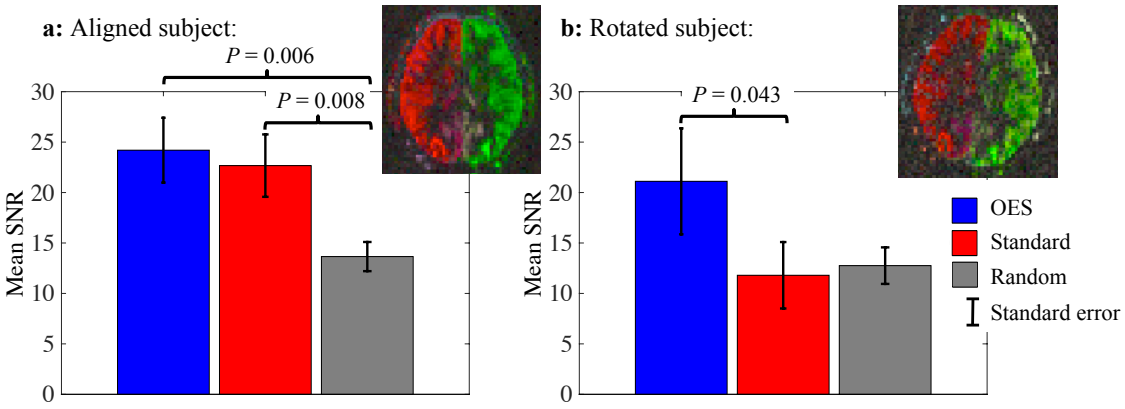


Figure 4.7: The mean SNR of the vascular territory images, produced using MI analysis, for 5 subjects **a**: aligned with the scanner and **b**: rotated. The vascular territory images show a single slice following the standard encoding method. The image from the rotated subject is visibly noisier.

For images produced using the MAP analysis similar trends were seen. Significant differences were found in the aligned case between the mean SNR of the OES and random images ($P = 0.011$) and between the standard encoding and random images ($P = 0.024$). The lack of a significant difference between the standard and OES methods is to be expected, as the MAP analysis is able to partially compensate for poorly conditioned encoding matrices [75].

Relative labelling efficiency maps

The relative labelling efficiency maps revealed the OES resulted in labelling efficiencies consistently close to the ideal values (± 1). When the subjects were rotated the relative labelling efficiency of standard encoding scheme images tended to move away from the ideal – in particular during the anterior-posterior encodings. In this case the vessels were both less efficiently labelled and labelled opposite to the desired encoding. Figure 4.8 shows a single subject example.

4.4.3 Subject scans: more than four vessels

When labelling above the circle of Willis it was not possible to optimally encode the vessels of interest due to B_0 field inhomogeneities at this level in the brain. The non-linear inhomogeneities resulting from air in the sinuses and ear canals led to distortions in the

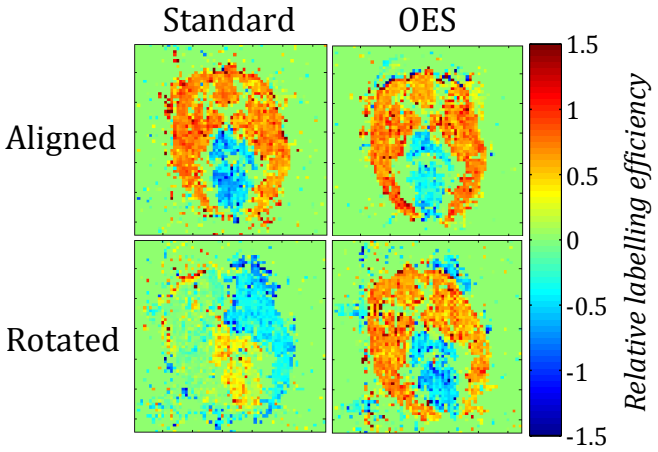


Figure 4.8: Relative labelling efficiency maps for the anterior-posterior labelling of a single subject.

encoding functions (Figure 4.9). As a result the vessels of interest were not labelled as expected and only a few vascular territories were separable using MAP or matrix inversion analyses.

The labelling plane in the neck, where the two internal carotid and two vertebral arteries run approximately perpendicular to the transverse plane, does not suffer from similar levels of B_0 inhomogeneity. Multi-phase (MP) PCASL [106] data is sensitive to phase offsets in the labelling plane. The method acquires data with multiple RF phase increments, instead of only 0 and π radians for standard PCASL label and control cycles. The MP-PCASL signal is then fit to the expected inversion response curve of the magnetisation. Any phase offsets in the labelling plane will shift the signal along this curve and so can be calculated. MP-PCASL data from a previous study across four healthy subjects, acquired using a labelling plane in the neck, have found the mean absolute phase offset at this level to be approximately 0.22 ± 0.16 radians (Figure 4.10). Here rough grey matter masks, based on thresholding the signal as in Section 4.3.3 for relative labelling efficiency maps, were used to identify voxels to include in phase calculations for each subject. The data were also smoothed with a 4 mm Gaussian kernel. Phase offsets of this magnitude will not interfere notably with the applied encodings, at a label location they result in a change in the inversion profile of the magnetisation of approximately 1%. Phase offsets of the magnitudes

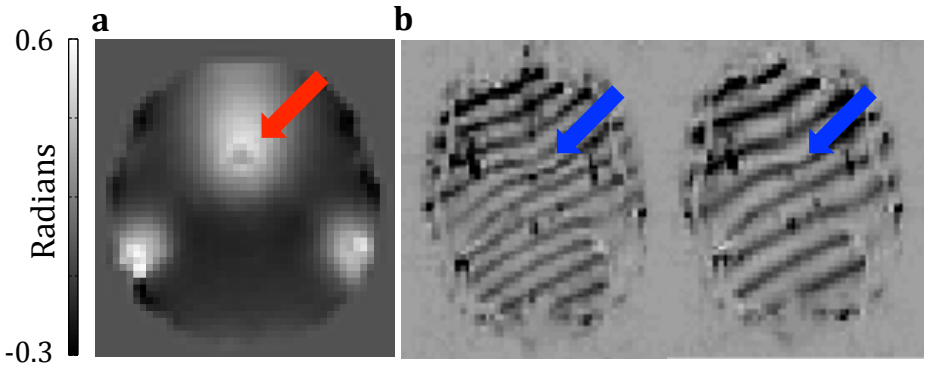


Figure 4.9: **a**: A field map above the circle of Willis showing the phase accrued between two RF pulses in the VEPCASL train and **b**: two different encoding functions in a labelling plane above the circle of Willis. The largest field offsets (red arrow) cause the greatest shifts in the VEPCASL encoding functions (blue arrows).

seen in Figure 4.9 result in changes to the inversion profile of the magnetisation on the order of 10%.

4.5 Discussion and conclusions

The OES method proposed here is capable of rapidly calculating SNR optimal vessel encodings for any number and arrangement of arteries using the smallest possible number of encoding cycles. The OES has been shown in simulations and in experiments using healthy subjects to be more SNR-efficient than standard or random encoding methods when labelling four vessels, regardless of their arrangement. This is particularly useful in patient groups with irregular vascular geometry, for example subjects with arteriovenous malformations, where the vasculature can be unusual and complex. The method is computationally fast and would be simple to integrate with any scanner operating system, as it only requires basic mathematical functions and knowledge of the vessel locations.

Compared to random encoding, the OES method provides a higher SNR efficiency when labelling any number of vessels, while still allowing a minimal number of encodings to be used. For vessel arrangements above the circle of Willis, simulations showed that random encoding does not achieve its theoretical SNR efficiency. This may be due to the fact that some of these vessels are close together and the theoretical value relates to well-separated

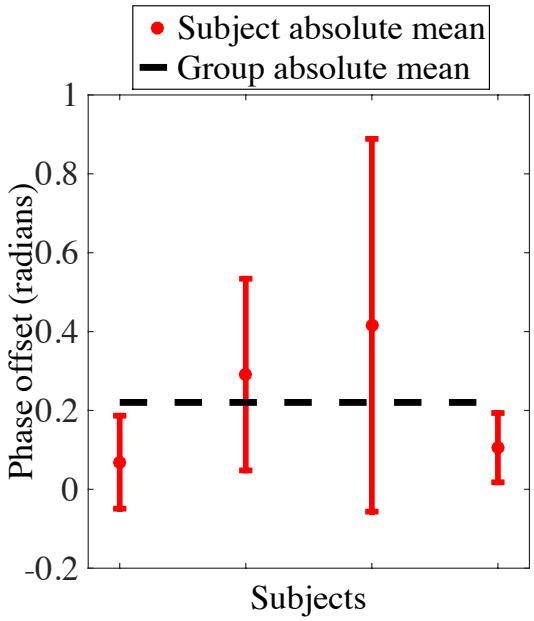


Figure 4.10: Absolute phase offset values in the labelling plane for four subjects, calculated from MP-PCASL data.

vessels [33]. Using the original random encodings [33] allowed us to compare the OES to an existing method.

Additional simulations, performed in the same way as nine vessel simulations in Section 4.3.1, demonstrated that including shorter wavelengths when encoding nine vessels can improve the SNR efficiency (Figure 4.11). Random encodings were generated in a similar way to the original set [33], but wavelengths as short as 4 mm were included; the first set of random encodings only included wavelengths as short as 30 mm. OES encodings with a minimum wavelength of 4 mm were also generated for comparison, this equates to a minumum motion setting of 1 mm in the calcuation of the encodings. The wavelength here is defined as the distance between two labelling points along the encoding function. The mean SNR efficiency of random encoding including shorter wavelengths still remained significantly below that of the OES encodings in both rotation and shift simulations, $P \approx 10^{-16}$ and $P \approx 10^{-4}$ respectively, according to a Mann-Whitney U-test. This was also the case when random encodings with a shorter minimum wavelength were compared to OES encodings with a minumum wavelength of 4 mm, $P \approx 10^{-16}$ and $P \approx 10^{-4}$. For the rotation simulations the mean SNR efficiency of OES encodings including shorter wavelengths was

not significantly different to the encodings calculated with a minimum 16 mm wavelength. However, when the vessel locations where randomly shifted there was a difference between the mean SNR efficiencies of the two cases: $P \approx 10^{-4}$

With random encoding a high number of encodings must be performed to ensure each artery is uniquely encoded, but, especially in the case of angiography where each image takes some time to acquire, it is not always possible to take the time to do so many encodings. Random encoding does, however, remove the need for planning the encodings, somewhat simplifying the acquisition process. One improvement to the OES method would be to automate the input of the vessel locations into the calculation of the encodings. This would simplify and speed up the planning process. One way this could be achieved would be to use a segmentation algorithm to find the vessel locations from time-of-flight data.

It should be noted that the OES method is somewhat dependent on the choice of function used to weight the Fourier space. Here, a gradually varying function with a maximum value of 0.5 was chosen, so that if an encoding function with a high spatial frequency leads to the most SNR-efficient encoding it is still likely to be selected, despite the weighting. However, where a number of spatial frequencies give a similar match to the desired ideal encoding, this weighting function encourages the selection of the lower spatial frequency. A linear weighting function was used in this study, but we expect that other smooth, slowly varying weighting functions would yield similar results. It is also possible to adjust the Fourier space mask according to the predicted motion of a given subject population. This should make the OES method robust to subject motion, although if the wavelength is limited to values larger than the vessel separations then the SNR efficiency of the encodings is likely to drop.

One general limitation of this Fourier based method is the implicit assumption that the encoding functions are sinusoids, rather than a sum of Fourier coefficients. As such it is an approximation, although both the sum of Fourier coefficients and the encoding function simulated using the Bloch equations are close to a sinusoid at the velocities typically found in the cerebral arteries, 0.3 – 0.4 m/s, [101, 103] (Figure 4.2). It is also worth noting that the ideal encodings specify the labelling efficiency to be ± 1 at each vessel location. Therefore,

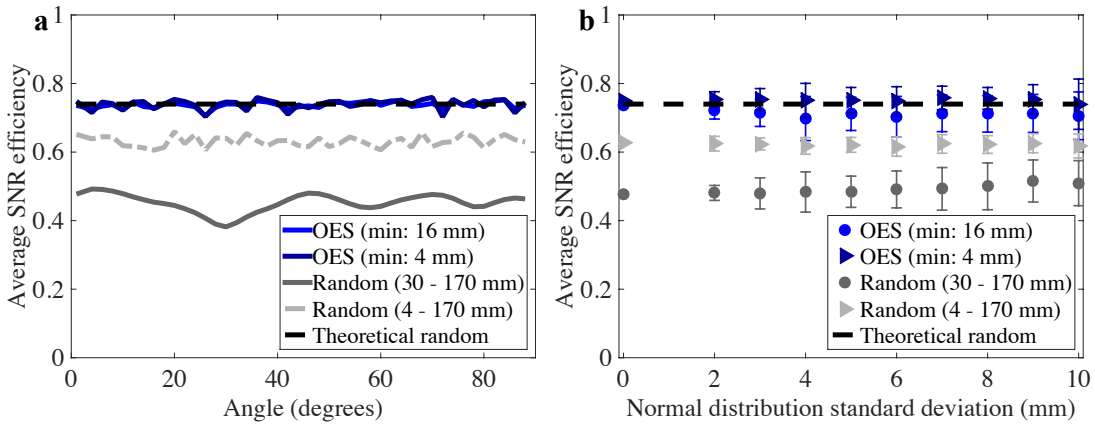


Figure 4.11: Simulated average SNR efficiencies in different scenarios: **a**: nine vessels rotated through various angles; **b**: nine vessels perturbed by random shifts of increasing magnitude. Random wavelengths (the distance between two tag locations along an encoding) of 30 – 170 mm are wavelengths taken from [33]. Random wavelengths of 4 – 170 mm were generated separately. The OES encodings were calculated with different minimum wavelengths allowed: 4 and 16 mm.

as long as the peaks/troughs of the encoding function are in the correct locations, the shape of the function in between is less critical.

As with all vessel-selective methods, the OES is more likely to perform poorly if the vessels of interest are very close together. An encoding function with a sufficiently small wavelength is required to differentiate such vessels. However, if the motion of a subject is greater than the distance between vessels of interest then vessel selectivity is not possible. The weighting and masking elements of the OES method are designed to encourage the choice of encodings that cope better with motion, while not completely excluding encodings with a wavelength small enough to differentiate close-set vessels. If vessels are close together in a complex geometry the use of a mask to limit the minimum possible wavelength could potentially reduce the SNR efficiency of the encodings. However, this is a reasonable trade-off to ensure the method is more robust to subject motion. The problem of closely spaced vessels is seen to a certain extent when simulating encodings on vessels above the circle of Willis (Figure 4.6), where there are a larger number of vessels close together and the average SNR efficiency does not exceed 0.75. However, this is still a considerable improvement over random encoding, where the mean SNR efficiency does not exceed 0.55.

When scanning subjects the OES method as described in this chapter was unable to provide optimal encodings for vessels above the circle of Willis due to substantial B_0 field inhomogeneities at this level in the brain. However, it is possible to base an ideal encoding scheme around the desired phase at each vessel location. In this way the expected shifts in the encoding functions, due to phase offsets generated by field inhomogeneities, can be incorporated into the selection of the optimal spatial frequency and phase. This adaptation to the OES method is described in Chapter 5.

Chapter 5

An optimised encoding scheme with off-resonance correction

Both PCASL and VEPCASL invert the magnetisation of blood by applying a train of radio-frequency (RF) pulses and gradients [30]. The pulse train causes a flow-driven adiabatic inversion of the blood magnetisation as it flows through a chosen labelling plane. The inversion is dependent on the phase accrued by the magnetisation between successive RF pulses and this phase depends on the gradients applied during and between the pulses [30, 33].

The presence of B_0 inhomogeneities in the labelling plane impacts on the labelling efficiency of PCASL and VEPCASL. Sources of off-resonance across the labelling plane introduce phase offsets that change the phase accrued at each vessel location. Consequently, the inversion efficiency of PCASL will be reduced and the encoding function present during unipolar VEPCASL will be shifted away from the desired label/control locations, as shown in the previous chapter (Figure 4.9)[1]. Depending on the particular subject, hardware and field strength of a given study, standard shimming may not be sufficient to correct for B_0 inhomogeneities [17].

A variety of methods have been proposed to deal with the issue of phase offsets in the labelling plane during PCASL scans. The multi-phase PCASL (MP-PCASL) approach varies

[1] Berry, E. S. K, Jezzard, P. and Okell, T. W., An optimized encoding scheme for planning vessel-encoded pseudocontinuous arterial spin labeling, Magnetic Resonance in Medicine, 74:1248-1256, 2015

the phase between each RF pulse over successive labelling cycles in equal steps from 0 to 2π radians [106]. This is in contrast to the standard PCASL label/control phase pattern where there is $0/\pi$ phase between RF pulses. The perfusion signal is determined by fitting the data acquired across all phase offsets to an expected inversion curve for the magnetisation. However, compared to the performance of PCASL without any phase offsets in the labelling plane, MP-PCASL suffers from lower SNR per unit time. OptPCASL [107] performs a series of prescans to automatically determine the phase offsets that need to be accounted for at each of the arteries in the labelling plane. Additional transverse gradients and an additional RF phase term are calculated from the prescan information and applied during a standard PCASL labelling scheme to correct for both a global phase offset in the labelling plane and offsets local to each vessel. The method currently only deals with three feeding vessels and the prescans add an extra 5 minutes to the total scan time. Luh *et al.* [108] have applied a method similar to OptPCASL at 7 T that likewise only enables correction for phase offsets at three vessel locations in the labelling plane. Jahanian *et al.* [17] developed a technique that takes phase offsets at the vessel locations from a field map of the labelling plane. An additional RF phase term and z gradient term are then calculated to best compensate for the phase offset across the entire labelling plane. The result is a compensation for a global phase offset, but offsets specific to individual vessels may not be dealt with.

Here we propose a technique to correct for phase offsets due to B_0 inhomogeneities in the labelling plane during both PCASL and VEPCASL scans. The method is based on the Optimised Encoding Scheme (OES) described in Chapter 4 [109], which has been adapted to take into account off-resonance at the vessel locations, ascertained from a rapidly acquired field map of the labelling plane. Transverse gradients and RF phase increments are then calculated, using the Fourier based OES method, which compensate for the offset at each vessel location. For VEPCASL scans the calculation results in alternative encoding functions that can account for phase offsets present in the labelling plane, whilst also labelling/controlling the desired vessels concurrently. The technique is automated, compatible with any number of vessels and requires only the addition of a field map of the labelling plane to established (VE)PCASL protocols. A US patent is pending for this work (United

States Patent application no. US 62/178,418). All scans in this chapter were acquired using a 3T TIM Verio system (Siemens, Erlangen, Germany). All subjects were scanned under a technical development protocol approved by local ethics and institutional committees.

5.1 Theory

PCASL either labels or controls all vessels in a chosen labelling plane. During a VEP-CASL cycle combinations of vessels will be labelled/controlled at the same time. The OES automatically defines an ideal encoding scheme for a given set of vessels and calculates encoding functions that will best achieve this scheme [109].

The technique described here defines an encoding scheme according to the required phase at each vessel location. As a result, it is capable of taking into account offsets already present when calculating encodings that best achieve the necessary phase at each vessel. Phase offsets are taken as the additional phase accrued by the magnetisation between RF pulses in the labelling pulse train due to the presence of B_0 inhomogeneities. The technique is organised similarly to the original OES method and is structured as follows:

1. Construct an "image" of the vessel locations. Each vessel is represented by $e^{i\Phi}$, where Φ is the desired phase at the vessel location
2. Zero-pad this "image" and take its Fourier transform
3. Weight and mask the resulting Fourier space to up-weight lower spatial frequencies and mask higher frequencies
4. Find the maximum intensity in this weighted Fourier space.

Φ depends on the ideal encoding scheme phase, 0 or π, with any local phase offsets, ϕ, subtracted. The phase required at a given vessel location i is therefore:

$$\Phi_{label} = 0 - \phi(i), \Phi_{control} = \pi - \phi(i) \tag{5.1}$$

The optimised encoding function, which now includes a correction for phase offsets in the labelling plane, is taken as the spatial frequency and phase at the maximum intensity point.

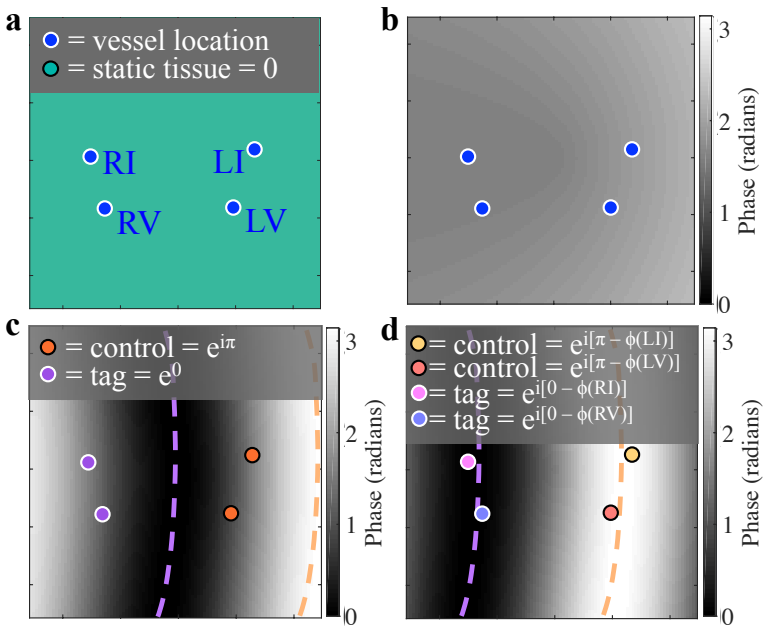


Figure 5.1: **a**: A group of four vessels representing the four main brain-feeding arteries (RI/LI = right/left internal carotid artery, RV/LV = right/left vertebral artery) and **b**: a simulated field map within the vessel labelling plane. **c**: Encodings applied across the labelling plane are shifted away from the ideal by the presence of phase offsets. **d**: If the offsets at each vessel, $\phi(vessel)$, are corrected for, the encodings label/control the vessels correctly.

The process is repeated for all cycles of the ideal encoding scheme. The technique currently requires the manual input of the vessel locations and phase offsets at those locations. The optimised encoding functions are then calculated without further user intervention. Calculation times are identical to the original OES method, less than 3 seconds (Section 4.3).

Figure 5.1 shows an example group of four vessels (5.1.a) and a simulated field map for the labelling plane (5.1.b). If the phase offsets due to the B_0 inhomogeneities plotted in the field map are not taken into account then encodings chosen by the OES method will be shifted away from the intended labelling positions (5.1.c). However, encodings where the phase offsets have been taken into account can be seen to label/control the desired vessels (5.1.d).

The Fourier space of the image of complex numbers is not symmetric so, unlike the original OES method, the mask used at this stage is circular, with a radius calculated according to

the predicted subject motion as in Chapter 4. Zero-padding of the Fourier space and up-weighting of lower spatial frequencies is performed as in Chapter 4.

5.2 Methods of evaluation

Simulations, phantom and subject scans are all used to evaluate the OES with off-resonance correction. The selection of the ideal encoding scheme depends on the number of vessels to be encoded and Section 5.2.1 details how the ideal schemes are chosen here. For all calculations of the optimised encodings with a correction for phase offsets the zero-padded image matrix size was 1024 x 1024. All simulations and phantom scans limited the predicted subject motion to 4 mm.

5.2.1 Choice of ideal encoding scheme

Four vessels

For four vessel VEPCASL of the main brain-feeding arteries in the neck the ideal encoding matrix as in Okell *et al.* [37] was used (Section 4.2.1).

More than four vessels

Although ideal encoding schemes for a given set of vessels are equivalent, the optimised encodings they give rise to will vary. The pattern in which the arteries of interest are labelled/controlled impacts on the SNR efficiency of that particular encoding. Figure 5.2.a is an example of where an ideal encoding scheme has forced the choice of a higher frequency encoding function for a set of vessels. Ideally, the magnetisation at each vessel would have a value of ± 1, so an absolute value of 1. The mean absolute value of the magnetisation across the vessels here is 0.74. Figure 5.2.b offers an example encoding that allows a broader spatial frequency to be chosen and yields a higher mean absolute magnetisation (0.86). If an ideal encoding scheme can be chosen where geometrically close vessels are, in general, labelled/controlled at the same time the arteries of interest would be more conveniently grouped. This would allow broader frequency encodings to be chosen and thus avoid suboptimal encodings in subjects with either a higher degree of motion or arteries

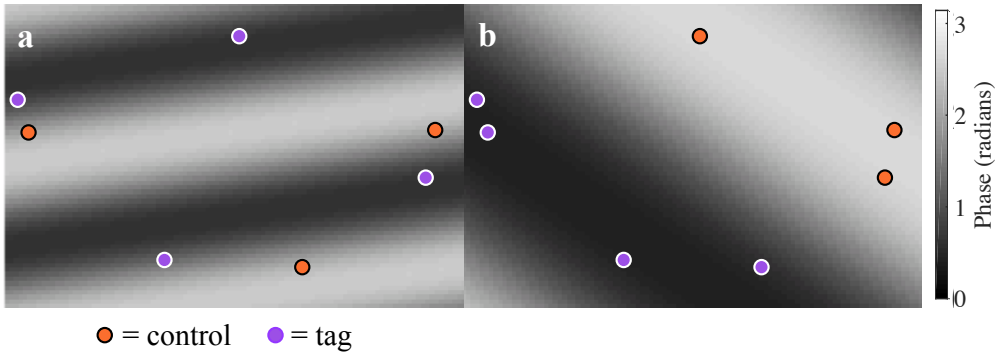


Figure 5.2: **a**: An example set of seven vessels with a complicated ideal encoding. **b**: An ideal encoding that allows for easier labelling/controlling of the vessels with a broader spatial frequency encoding function.

of interest that are very close together combined with small levels of motion. A lower frequency will help ensure the encoding of each vessel is close to that expected, even in the event of subject motion.

The columns of a Hadamard matrix will always yield an encoding matrix with SNR efficiency equal to one [30]. As per the previous chapter, for encoding more than four vessels columns from the Hadamard matrix closest in size to (but bigger than) the number of vessels, plus static tissue, are used as the ideal encoding scheme here. The order of the Hadamard matrix columns is not important for decoding the signals or for SNR efficiency. Therefore, an additional step has been added to the OES technique to choose the order of the columns that will better encode a given vessel geometry. Adjusting the order of the columns changes the pattern in which the vessels are labelled/controlled, allowing for more optimal patterns to be chosen.

The condition number of an encoding matrix indicates how sensitive the resulting vascular territory information will be to errors in the acquired data. Ideally the condition number would be as low as possible – with a minimum (and ideal) value of one. Here, an algorithm has been developed to find an ideal encoding scheme that leads to an optimised encoding matrix with a minimised condition number. When more than four vessels are being encoded in a subject, the columns of the initial Hadamard matrix chosen as the ideal encoding scheme are randomly ordered to find alternative Hadamard matrices. The ideal matrix that

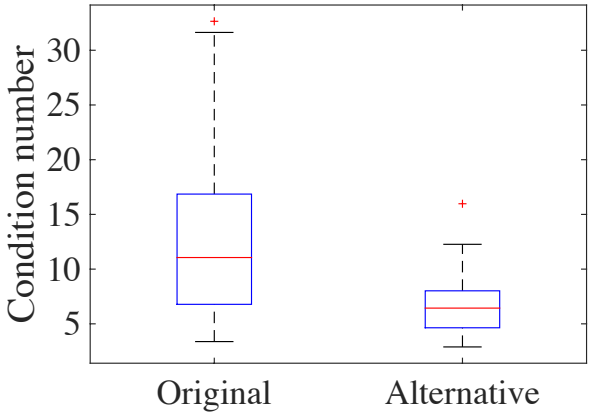


Figure 5.3: The mean condition number of the optimised encoding matrices calculated for 20 sets of nine vessels before (Original) and after (Alternative) application of the algorithm to find alternative Hadamard ideal encoding schemes. Red crosses represent outliers (>1.5x the interquartile range from the upper/lower quartile).

corresponds to the optimised encoding matrix with the lowest condition number is then chosen. The algorithm is structured as follows:

1. Choose the initial ideal Hadamard encoding matrix for the number of vessels to be encoded

2. Calculate the optimised encoding matrix using the modified OES method described above, accounting for off-resonance at each vessel location

3. Randomly permute the columns of the initial Hadamard matrix and calculate the corresponding optimised encoding matrix

4. Continue permuting the columns until either the condition number of the optimised encoding matrix is lower than the starting encoding matrix or the permutations have been running for more than 10 seconds

5. The ideal encoding scheme with the lowest condition number is then set as the initial Hadamard matrix before steps 3 and 4 are repeated twice.

In this way the entire process is time limited to approximately 35 seconds and the resulting encoding matrix will always be at least as good as the initial matrix. Figure 5.3 shows the results for the above algorithm applied to 20 different sets of nine vessels, representative of vessels above the circle of Willis, with corresponding off-resonance values. The mean

condition number of the final encoding matrices is lower than the mean starting value by approximately 49%, significantly different ($P = 0.004$) according to a Mann-Whitney U-test.

5.2.2 Simulations

Simulations were performed in Matlab® (Mathworks™, Natick, Massachusetts, USA) to test the efficacy of the off-resonance correction in the labelling plane for both PCASL and VEPCASL. The SNR efficiency of encodings was tested across three scenarios for four vessels and six scenarios for cases of greater than four vessels:

1. No phase offsets present
2. Phase offsets present, encodings un-corrected
3. Phase offsets present, encodings corrected

   For more than four vessels:

4. No phase offsets present, alternative Hadamard ideal encoding matrix used
5. Phase offsets present, encodings un-corrected, alternative Hadamard ideal encoding matrix used
6. Phase offsets present, encodings corrected, alternative Hadamard ideal encoding matrix used.

Generation of field offsets

Phase offsets were taken from both simulated and real field maps. The simulated field maps (Figures 5.4.a and 5.5.a) were generated in Matlab to replicate the combination of a linear and quadratic distribution of field offsets. Two real field maps were used (Figures 5.4.b and 5.5.b); one was taken from a labelling plane in the neck of a healthy subject where a linear shim offset had been applied and one was taken from a labelling plane above the circle of Willis. The offsets in all the field maps were gradually increased to test the off-resonance correction against increasingly large phase offsets, up to twenty times the original values.

Vessel arrangements in the field offsets

For both simulated and real field maps, arrangements of four and nine vessels, representative of arteries in labelling planes in the neck and above the circle of Willis, were perturbed by random distances and directions. The perturbations for each vessel were randomly chosen from a normal distribution (mean = 0 ± 2 mm) and twenty different arrangements of both four and nine vessels were simulated. The arrangements of four vessels were perturbed within the real map acquired in the neck and the nine vessels within the real field map acquired above the circle of Willis.

(VE)PCASL SNR efficiency calculations

As discussed in Chapter 4, the labelling values of the calculated encodings were drawn from simulated magnetisation inversion curves for the PCASL/unipolar VEPCASL pulse trains, to more accurately represent the encoding matrices that can be achieved. For a given simulation of PCASL encodings, the SNR efficiency was computed by averaging the label/control magnetisation inversion values across vessels. The SNR efficiency calculation (Equation 4.3) [30] was then applied to the averaged label/control all values. In other words, the SNR efficiency of a 2 x 2 encoding matrix, labelling/controlling one 'average' vessel and controlling static tissue, was calculated. In the case of VEPCASL the SNR efficiency was calculated according to Equation 4.3 and averaged across all vessels.

For both the four and nine vessel cases the SNR efficiency of the encodings of each vessel arrangement was calculated for the twenty different simulated and real field maps (a total of 400 calculations). The mean SNR efficiency for each arrangement across all field maps was then computed. The group mean is considered to be the mean value across the vessel arrangements.

5.2.3 Phantom scans

A Eurospin test object 3 phantom, containing plastic rods used to represent the main brain-feeding arteries in the neck, was scanned with a 12-channel head coil. The encodings for PCASL, four vessel VEPCASL and seven vessel VEPCASL were mapped, similarly to

those seen in Figure 4.9, but acquired with a higher resolution readout scheme insensitive to image distortion. The three scenarios tested in simulations were compared. A three-dimensional multislab time-of-flight (TOF) angiography sequence was performed first to select a labelling plane and corresponding vessel locations in all scans. For all (VE)PCASL scans the labelling parameters of Okell *et al.* [8] were used.

Offsets were generated in the labelling plane by manually changing the scanner X direction shim by approximately 85 μT/m. The phase offsets needed to calculate the corrected encodings were taken from field maps acquired in less than one minute. In the four vessel VEPCASL scans phase unwrapping of data from the acquired field map (voxel size = 4.1 x 4.1 x 5 mm, TR = 400 ms, TE1 = 5.19 ms, TE2 = 7.65 ms) was required to obtain the true offsets in the labelling plane. In all other scans the difference between the two TEs of the field map was changed to the RF pulse spacing in the labelling plane to avoid this step (voxel size = 2.5 x 2.5 x 5.0 mm, TR = 200 ms, TE1 = 5.19 ms, TE2 = 6.19 ms). Phase unwrapping was not required in this case as we are only interested in the deviation in phase from 0 or π radians that is accrued between two RF pulses, which is cyclic once the phase has wrapped.

All encodings were imaged with a spoiled gradient echo readout [8] in a single slice across the labelling plane, readout flip angle = 10°. The four vessel VEPCASL encodings were acquired with a labelling duration of 400 ms (voxel size = 0.9 x 0.9 x 5 mm, TR = 5.92 ms, TE = 2.95 ms, acquisition window 400 ms) and other scans with a labelling duration of 300 ms (voxel size =1.6 x 1.6 x 5 mm, TR = 5.30 ms, TE = 2.64 ms, acquisition window 300 ms).

5.2.4 Subject scans

All scans were performed on healthy subjects with a 32-channel head coil. A three-dimensional multislab TOF angiography sequence was performed at the start of each scan to allow selection of a labelling plane and localisation of vessels (voxel size = 0.8 x 0.8 x 1.3 mm). Additionally, field maps of the labelling plane and the imaging region were

acquired during each scan. The resolution of the labelling plane field map was brought into line with the TOF scan to better localise the phase offsets at the vessels (voxel size = 0.9 x 0.9 x 2.0 mm, TR = 200 ms, TE1 = 5.19 ms, TE2 = 6.19 ms, acquisition time = 1 minute). A (VE)PCASL labelling scheme was combined with a single-shot echo-planar imaging (EPI) readout to acquire all perfusion data. The majority of the scan parameters were the same as those in Section 4.3.2 [8]: tag duration = 1.4 s, voxel size = 3.4 x 3.4 x 5 mm and a single post labelling delay of 1 s. The number of measurements acquired varied depending on the particular scan. A field map of the imaged slices was acquired with the same resolution as the EPI readout (voxel size = 3.4 x 3.4 x 5.0 mm, TR = 200 ms, TE1 = 5.19 ms, TE2 = 7.65 ms, acquisition time = 54 s) to make distortion correction of the EPI images possible prior to analysis.

Neck labelling plane: four vessels

PCASL and VEPCASL perfusion scans were performed with the labelling plane positioned in the neck, to provide perfusion data for the right and left internal carotid arteries (RICA/LICA) and the right and left vertebral arteries (RVA/LVA). The three scenarios tested were the same as those investigated with simulations (no phase offsets, uncorrected offsets and corrected offsets), with the expected maximum subject motion in the OES calculations set to 4 mm. Similarly to the phantom scans, to test the response of the correction to off-resonance, phase offsets were induced in the labelling plane by both shifting the automated shim adjustment volume higher in the brain and modifying the in plane and through plane shim currents. The ZX shim was shifted by approximately 350 μT/m^2 and the Z^2 shim by approximately 250 μT/m^2. Scans where the shim volume and gradients were set automatically by the system were deemed to be those with no phase offsets present, as they are comparable to current (VE)PCASL studies. The shim settings were kept the same across all field map and perfusion data acquisitions for a given scenario.

PCASL scans of 40 measurements (acquisition time 2'27 s) were performed on 6 subjects, 2 female, mean age 27 $\pm$ 3 years. VEPCASL scans of 80 measurements (acquisition time 4'45 s) were performed on 5 subjects, 1 female, mean age 27 $\pm$ 3.5 years. PCASL and VEPCASL scans were acquired sequentially in all of the scans, apart from one where only

PCASL scans were performed. The data for one additional subject was excluded because all of the scans were severely motion corrupted.

Above circle of WiIlis labelling plane: more than four vessels

VEPCASL perfusion scans were performed with a labelling plane above the circle of Willis to yield perfusion data on the anterior, middle and posterior cerebral arteries and their branches. Random encoding [33] was compared with optimised encodings calculated:

1. Without correcting for phase offsets in the labelling plane
2. With phase offset correction
3. With both phase correction and choosing an alternative Hadamard matrix (Section 5.2.1).

All optimised encodings were calculated with a predicted subject motion of 7.5 mm and with the complementary pair of each encoding included, as in the four vessel encoding scheme. Paired encodings allow for the subtraction of cycles without loss of vessel specific information. The pairs of encoding cycles are acquired consecutively and this has been found to reduce artefacts due to scanner drift and/or subject movement [8]. The predicted motion was chosen so the minimum possible wavelength of a chosen encoding was the same as the minimum random encoding wavelength, to ensure a fair comparison.

VEPCASL scans of 120 measurements (acquisition time 7'14 s) were performed on 4 subjects, 2 female, mean age 26.3 $\pm$ 1.3 years. In two subjects the scan acquisition order was: random encoding, OES without off-resonance correction, OES with correction and OES with correction and using an alternative Hadamard matrix. In the other two subjects random encoding was moved to the end of the acquisition order to prevent bias. An additional, two-dimensional, TOF angiogram was acquired (voxel size = 0.6 x 0.6 x 5 mm) to better facilitate vessel localisation. The width of the acquired slice was increased to be close to the true width of the labelling plane. Angiograms above the circle of Willis were also acquired using the alternative Hadamard encoding scheme, to provide a comparison between the vascular territories and the feeding vessels. A single measurement of each encoding was acquired, 24 measurements in total. The angiograms were acquired with a

balanced steady-state free precession radial readout (Subjects 1 and 2: 80 spokes, x4.4 undersampled, voxel size = 0.9 x 0.9 x 50.0 mm, TR = 5.09 ms, TE = 2.55 ms, acquisition time ≈1'03 s. Subjects 3 and 4: 120 spokes, x3 undersampled, voxel size = 1.0 x 1.0 x 50.0 mm, TR = 4.97 ms, TE = 2.49 ms, acquisition time ≈2'29 s). Further details of this sequence can be found in Chapter 6. For the first two subjects the encodings in the labelling plane were imaged in the same way as during phantom scans (Section 5.2.3).

5.2.5 Subject scans analysis

For all scenarios imaged with an induced shim offset the FMRIB Software Library tool FUGUE [110] was used to correct for distortion in the EPI images. For each subject grey matter masks were created using partial volume maps, obtained with the FMRIB Software Library tool FAST [104] from T_1-weighted structural images acquired separately. The masks were registered to the (VE)PCASL space of each subject using a linear registration [105] before being thresholded with a value of 0.5.

PCASL image analysis

PCASL images were averaged across all repeats and control/label cycles subtracted to yield ASL signal images proportional to the tissue perfusion (Section 2.2). A grey matter mask was then applied to the perfusion images of each subject. SNR was calculated using the mean of the signal in all slices from the grey matter masked images divided by the standard deviation of a background region-of-interest (ROI) in the unmasked images. The SNR was averaged across subjects and compared for the three scenarios tested.

Four vessel VEPCASL image analysis

Images were averaged across all repeats and a Bayesian, maximum *a posteriori* (MAP), method was used to separate out vessel specific information into vascular territory maps (Section 3.1.4) [75]. The MAP analysis was updated to include shifts in the inversion efficiency curves in the labelling plane due to off-resonance. The SNR for VEPCASL encoding was calculated as in Section 4.3.3, i.e. with signal from the dominant feeding vessel in each voxel that falls within a grey matter mask. The SNR of all vascular territories

was averaged for each subject before averaging the SNR across subjects and comparing for the three scenarios tested.

More than four vessel VEPCASL image analysis

Vascular territory analysis and calculation of SNR in perfusion territories was performed in the same way as for four vessels, i.e. a MAP analysis method followed by SNR calculations using only signal from grey matter. Additionally, MAP analysis was used to separate out vessel specific information in the acquired angiograms.

In certain scenarios, such as angiography, the acquisition time of a given readout scheme prohibits multiple acquisitions of the same encoding. To assess the fidelity of the different encoding schemes with fewer measurements, the number of measurements used in the analysis was reduced to 72 and 48 measurements retrospectively and MAP and SNR analyses performed.

5.3 Results

5.3.1 Simulations

Four vessels

Figures 5.4.c-f show the results of the four vessel simulations for PCASL and VEPCASL across the field maps and scenarios tested. When no offsets were present the inversion efficiency of each PCASL encoding was assumed to be the optimal value from the simulated inversion efficiency curve, consequently the standard deviation for this scenario was always zero. In all labelling and field map combinations every scenario was significantly different to the others according to Mann-Whitney U-tests, except for the comparison of the no offset and offset corrected scenarios for the real and simulated field map VEPCASL simulations ($P = 0.882 and 0.102$ respectively). However, the mean values for the no offset and offset corrected scenarios are very similar to each other and greater than the offset scenario values. The mean PCASL encoding SNR efficiency across both field maps with no offsets was 0.938. This value ($\pm$ standard deviation) dropped to 0.687 $\pm$ 0.022 (simulated field map) and 0.528 $\pm$ 0.099 (real field map) when phase offsets were present but

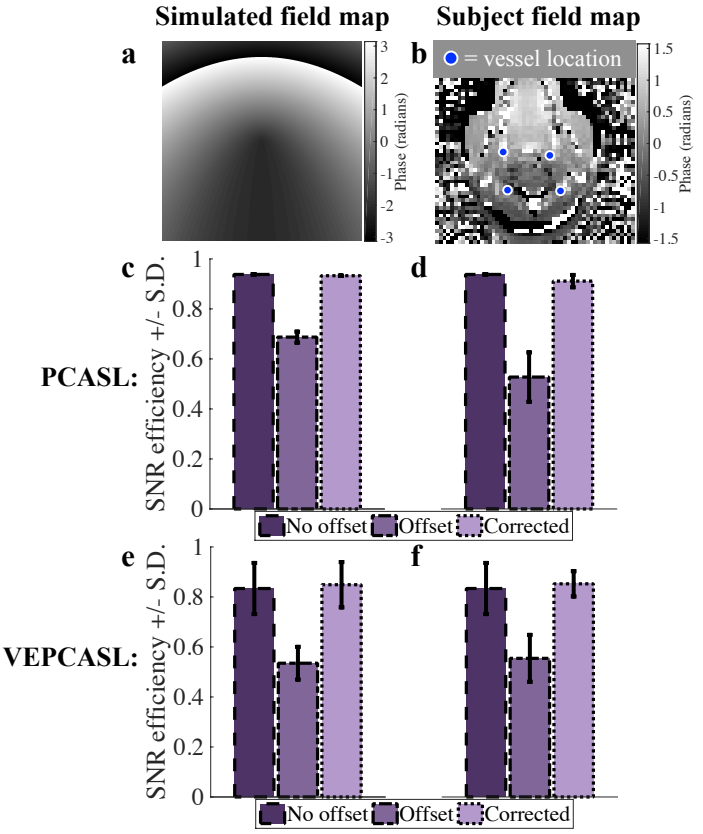


Figure 5.4: **a**: Simulated and **b**: real field maps, with a phase offset in the anterior-posterior direction and an example set of four vessels, used in simulation of PCASL and VEPCASL encodings. Bar charts **c – f** show the mean SNR efficiency results for the PCASL and VEPCASL simulations across all field map and offset correction scenarios.

not corrected for. After correction using the adapted OES method, the mean PCASL SNR efficiency rose back to 0.933 ± 0.001 (simulated field map) and 0.911 ± 0.025 (real field map), very close to the no offset case. A similar trend was seen for VEPCASL: the mean encoding SNR efficiency across both field maps with no offsets was 0.834 ± 0.102, which dropped to 0.535 ± 0.065 (simulated field map) and 0.554 ± 0.094 (real field map) when offsets were present, but recovered to 0.849 ± 0.091 (simulated field map) and 0.853 ± 0.050 (real field map) when these were accounted for in the OES framework.

More than four vessels

The results of simulations for more than four vessels are shown in Figures 5.5.c and d. According to Mann-Whitney U-tests, the SNR efficiency for scenarios where there is no offset present and where offsets have been accounted for is significantly different to cases

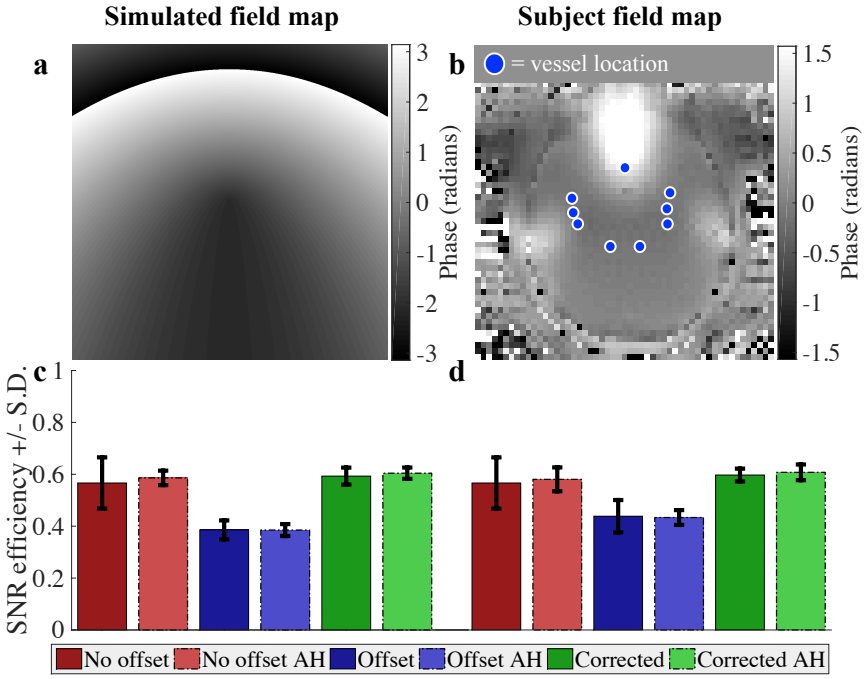


Figure 5.5: **a**: Simulated and **b**: real field maps, with an example set of nine vessels, used in simulation of VEPCASL encodings. Bar charts **c** and **d** show the mean SNR efficiency results for the simulations. AH = Alternative Hadamard ideal encoding matrix used.

where there are phase offsets present and no correction applied. The SNR efficiency of the alternative Hadamard simulations is not significantly greater than the equivalent cases where it has not been used, but in general it results in slightly higher SNR efficiency and a smaller spread of efficiencies. The mean values for the no offset and offset corrected scenarios for both the simulated and real field maps are all similar to each other and greater than the values for the offset scenario.

For the simulated field map the mean encoding SNR efficiency ($\pm$ standard deviation) with no offsets was 0.567 $\pm$ 0.099 and 0.586 $\pm$ 0.028 using an alternative Hadamard matrix. This dropped to 0.386 $\pm$ 0.037 and 0.385 $\pm$ 0.023 respectively when offsets were applied to the simulations. Following correction the SNR efficiency recovered to 0.593 $\pm$ 0.033 and 0.604 $\pm$ 0.022 for the alternative Hadamard case. Very similar trends were seen for the real field map: mean encoding SNR efficiency with no offsets was 0.567 $\pm$ 0.099 and 0.581 $\pm$ 0.046 using an alternative Hadamard matrix. With offsets present but no correction applied the mean SNR efficiency was 0.438 $\pm$ 0.062 and 0.433 $\pm$ 0.029 respectively and

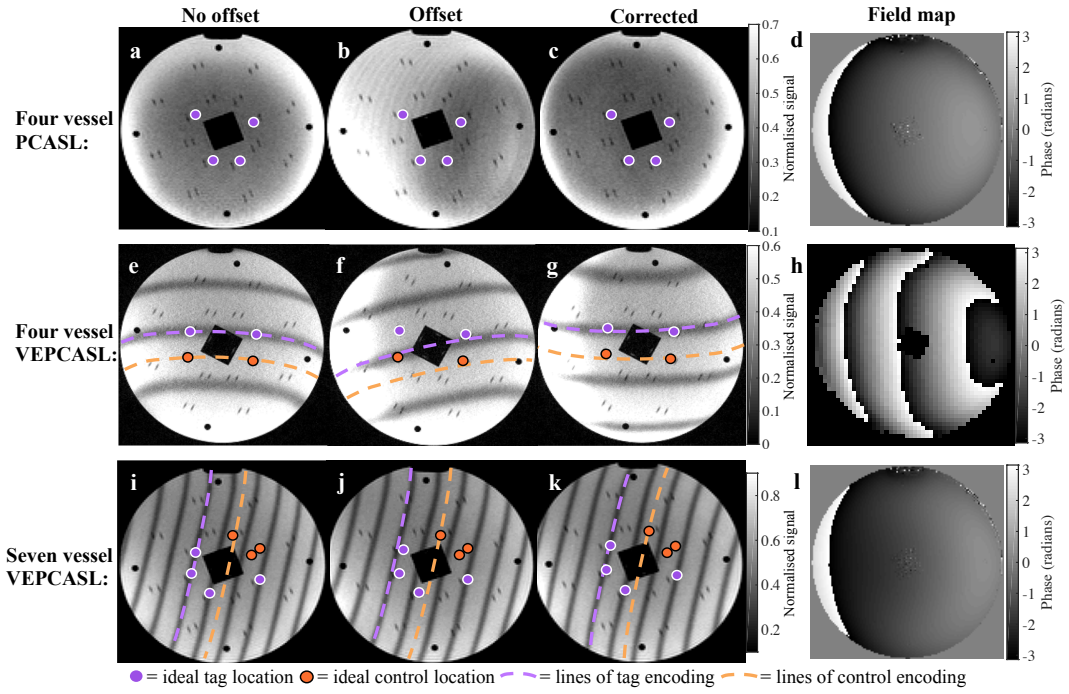


Figure 5.6: Phantom scans showing the encodings in the labelling plane when there are no offsets present (**a, e, i**), phase offsets are present but no correction has been made to the encodings (**b, f, j**) and the performance of corrected encodings (**c, g, k**). PCASL (top row, four vessel VEPCASL (middle row) and seven vessel VEPCASL (bottom row) encodings were applied with right-left phase offsets induced (**d, h, l**).

after correction they rose to 0.597 ± 0.025 and 0.608 ± 0.030.

5.3.2 Phantom scans

Figure 5.6 illustrates the ability of the OES correction technique to choose encodings that account for phase offsets in the labelling plane. The figures for each vessel number have been normalised with respect to the corresponding no offset scan in order to have the same scaling. In Figures 5.6.a, e and i no offsets are present and the dark bands in the image, which correspond to regions that would be efficiently labelled, line up precisely with the targeted tag locations whilst avoiding those "vessels" which should be placed in a control condition. In Figures 5.6.b, f and j the labelling regions have all been shifted away from the desired labelling locations due to the presence of off-resonance. Figures 5.6.c, g and k show how the encodings calculated with a correction for phase offsets in the labelling

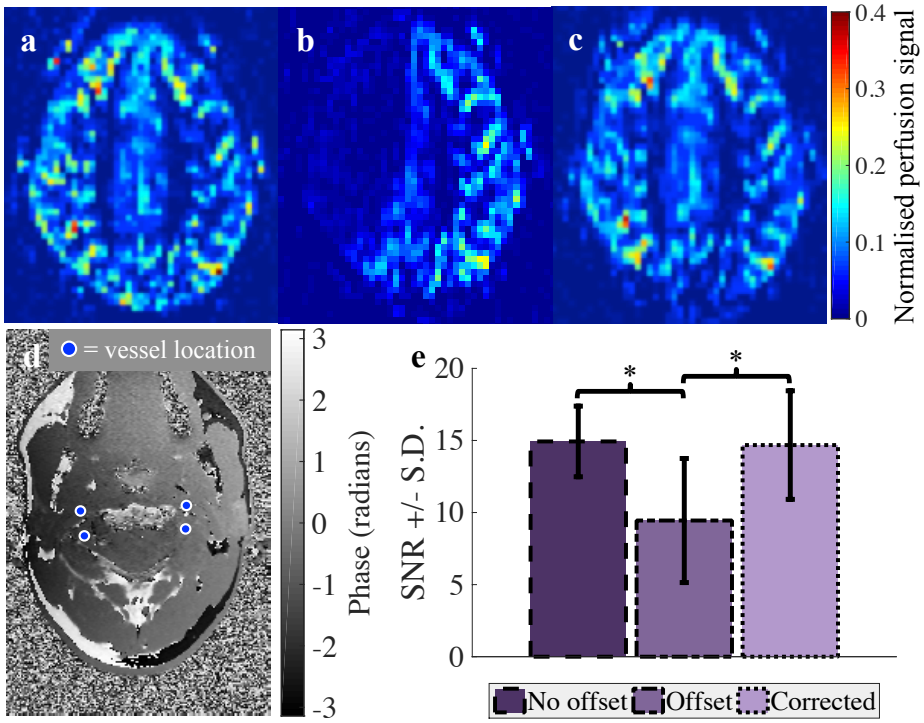


Figure 5.7: The perfusion signal in a single slice of the brain following PCASL with **a**: no offsets in the labelling plane, **b**: offsets, un-corrected in the encoding and **c**: an offset corrected encoding. **d**: Field map of the labelling plane after shim adjustments to generate phase offsets. **e**: Mean SNR $\pm$ standard deviation of the perfusion signal across all subjects. No offset = 14.9 $\pm$ 2.4, offset = 9.4 $\pm$ 4.3, corrected = 14.7 $\pm$ 3.8.

plane undo the effect of off-resonance to restore the correct encoding pattern.

5.3.3 Subject scans

Neck labelling plane: four vessels

Figure 5.7 shows the perfusion signal in a single imaging slice of a representative subject following PCASL. The images demonstrate the loss of signal in the brain (Figure 5.7.b) when there are phase offsets in the labelling plane and the corresponding recovery of signal if the encodings are calculated to take these into account (Figure 5.7.c). Calculated across all subjects, the SNR of the no offset and corrected scenarios was significantly greater than the SNR from the offset scans according to a paired t-test ($P = 0.003$ in both cases). The drop in SNR in the offset case represented a signal loss of $\approx 37\%$ versus the no offset case, whereas between the no offset and corrected scenarios there was only a 2% difference,

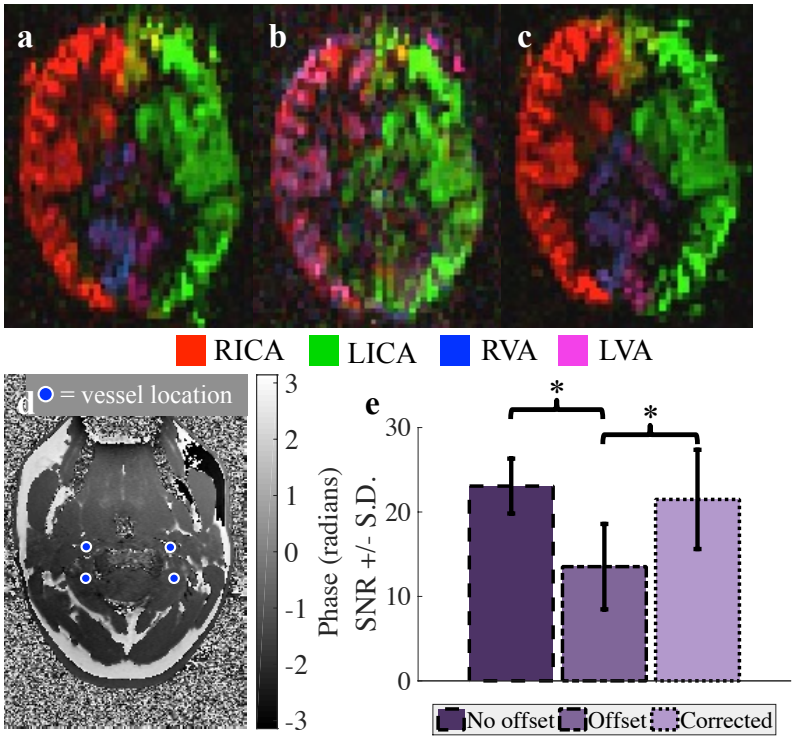


Figure 5.8: The vascular territories of the main brain-feeding arteries following VEPCASL. **a**: No offsets in the labelling plane, **b**: offsets, un-corrected in the encoding and **c**: offsets corrected in the encoding. **d**: Field map of the labelling plane after shim adjustments to generate phase offsets. **e**: Mean SNR $\pm$ standard deviation of the vascular territory signal. No offset = 23.1 $\pm$ 3.2, offset = 13.5 $\pm$ 5.1, corrected = 21.5 $\pm$ 5.9.

which was not significant. Any signal loss leads to underestimations in the cerebral blood flow, which is directly related to the perfusion signal.

Figure 5.8 shows the signal in the vascular territories of the main brain-feeding arteries for a single imaging slice following VEPCASL. The images demonstrate the mis-assignment of vascular territories during analysis when there are phase offsets in the labelling plane (Figure 5.8.b) and the restoration of the correct vascular territories if the encodings are calculated to take these into account (Figure 5.8.c). As in the PCASL case the SNR of the no offset and corrected scenarios was significantly greater than the SNR from the offset scans according to a paired t-test ($P = 0.003$ in both cases).

Above circle of WiIlis labelling plane: more than four vessels

Figure 5.9 shows an example imaging slice acquired following the four different encoding schemes tested. The vascular territories according to the MAP analysis vary depending

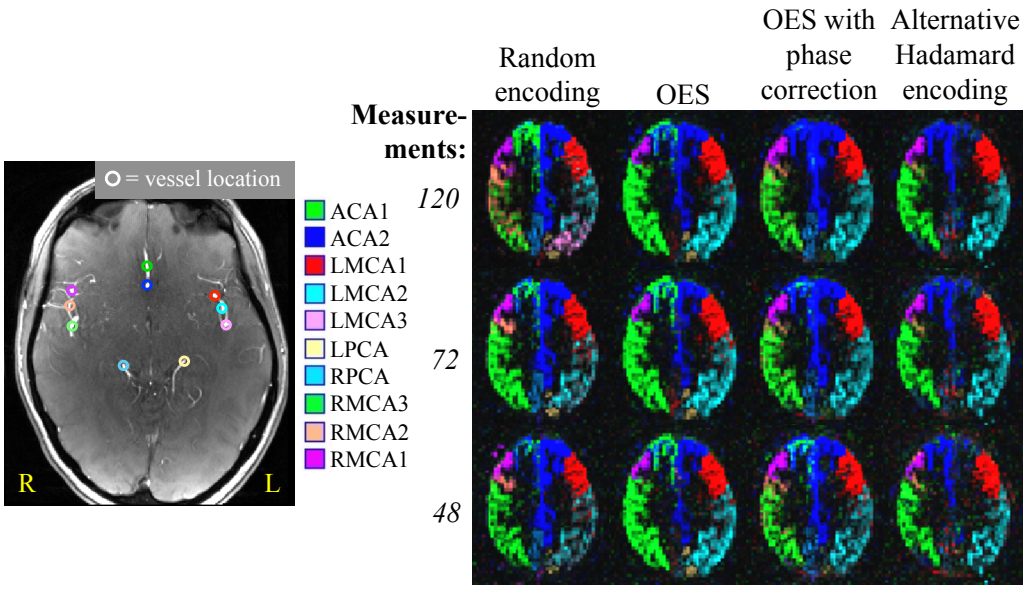


Figure 5.9: The labelling plane (2D TOF image) is shown with the cerebral arteries identified. The right hand images show individual vascular territories across one slice in a single subject, following analysis with 120, 72 and 48 measurements for each encoding scheme. ACA = anterior cerebral artery, L/RMCA = left/right middle cerebral artery, L/RPCA = left/right posterior cerebral artery.

on both the encoding scheme and the number of measurements used in the analysis. The vascular territories found following random encoding are most clearly delineated when 120 measurements are acquired, with regional signal assignment following the pattern of arteries identified in the labelling plane. Using only 48 measurements results in a loss in territory definition and signal. The differentiation of vascular territories following OES, OES with offset correction and OES with correction using an alternative Hadamard matrix has met with mixed success. This is common across all subjects. In this particular subject the posterior circulation has not been well defined. There is less signal assigned to the posterior cerebral arteries and the first branch of the anterior cerebral artery as compared to random encoding. However, the vascular territories identified following OES based schemes remain consistent regardless of the number of measurements used in the analysis. When fewer encodings are used the vascular territories of random encoding become more similar to those of the OES based methods.

Upon inspection of the encodings and angiogram results (Figure 5.10) it can be seen that arteries in the scalp were also labelled, but had not been identified during the initial vessel

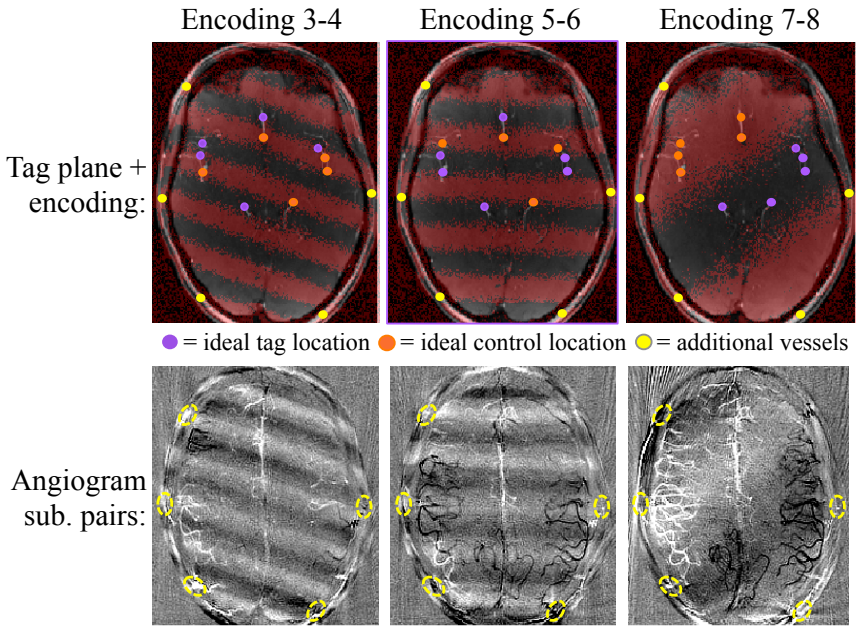


Figure 5.10: The top row shows three subtracted pairs of encodings (red = control regions), calculated using an alternative Hadamard matrix. The bottom row shows angiograms for the same subtracted pairs of encodings. The encodings are visible in the angiograms due to the proximity of the labelling plane to the imaging slab. Additional arteries in the scalp are identified by dashed ellipses.

localisation. Whilst the original arteries identified are fairly well encoded (Figure 5.10, top row), in the angiograms some of the arteries in the scalp were clearly contributing signal without having been identified (Figure 5.10, bottom row, yellow dashed ellipses). In the subject shown the right and left occipital arteries and superficial temporal arteries (parietal and frontal branches) were identified from the angiograms and located in the labelling plane (Figure 5.11). The analysis process was re-run to include the five additional vessels, to assess whether vascular territory identification could be improved (Figure 5.11), as extracranial arteries may contribute to the cerebral blood flow [2].

The angiogram in Figure 5.11 shows that some of the scalp arteries could be correctly separated, particularly the parietal branches of the superficial temporal arteries. However, signal from the others was still assigned to the cerebral arteries. The angiogram is particularly noisy though, due to remaining signal from the encodings where the imaging slab was too close to the labelling plane. Even with the inclusion of the additional arteries the perfusion images in Figure 5.11 are similar to Figure 5.10; the posterior circulation is not

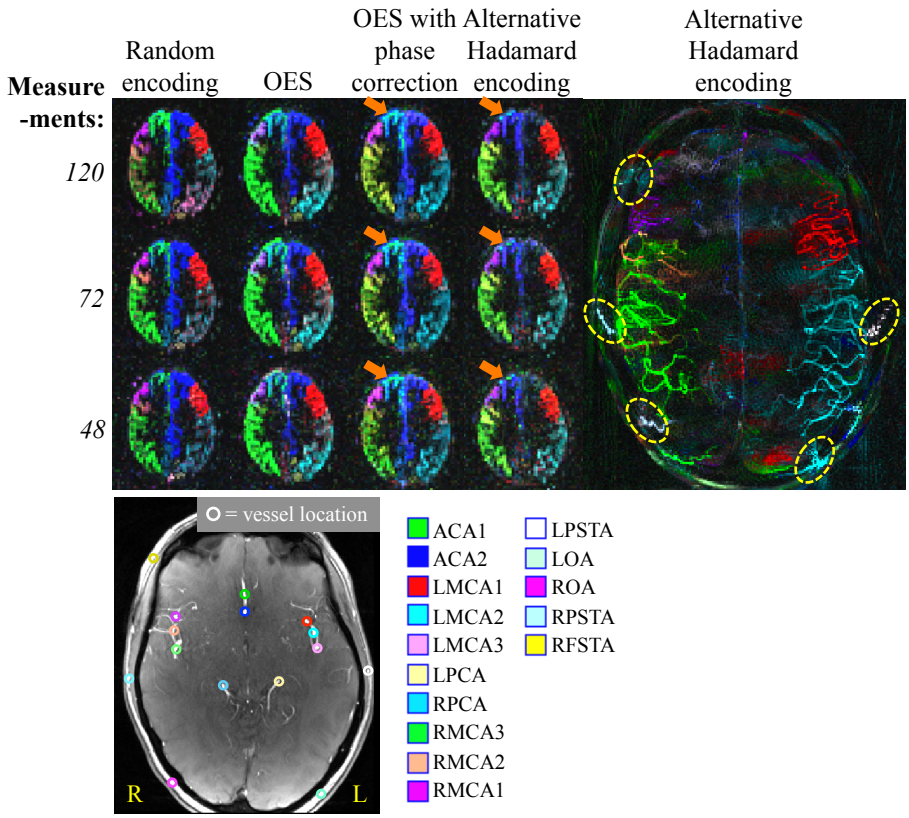


Figure 5.11: The cerebral and scalp arteries are identified in the labelling plane (2D TOF image). The perfusion images show individual vascular territories across the same slice/subject as Figure 5.9, following analysis with 120, 72 and 48 measurements for each encoding scheme. Orange arrows indicate mixed signal of the anterior cerebral arteries. The right-hand image is an angiogram acquired with the encodings calculated from an alternative Hadamard matrix. Arteries labelled: ACA = anterior cerebral, L/RMCA = left/right middle cerebral, L/RPCA = left/right posterior cerebral, L/RPSTA = left/right parietal branch superficial temporal, L/ROA = right/left occipital, RFSTA = right frontal branch superficial temporal.

that well defined in the OES based methods and there is disagreement between the methods on the exact assignment of vascular territories for the other arteries. There are some differences however. Before the inclusion of the extra vessels very little signal in the alternative Hadamard and OES with correction schemes was assigned to one of the anterior cerebral arteries (ACA1, Figure 5.10). After inclusion of the scalp arteries more signal was assigned to this artery, resulting in a mixing of signal between the two anterior cerebral arteries (Figure 5.11, orange arrows). There is also more mixing of the right middle cerebral arteries (RMCA2, RMCA3, Figure 5.11). Including additional scalp vessels has affected the as-

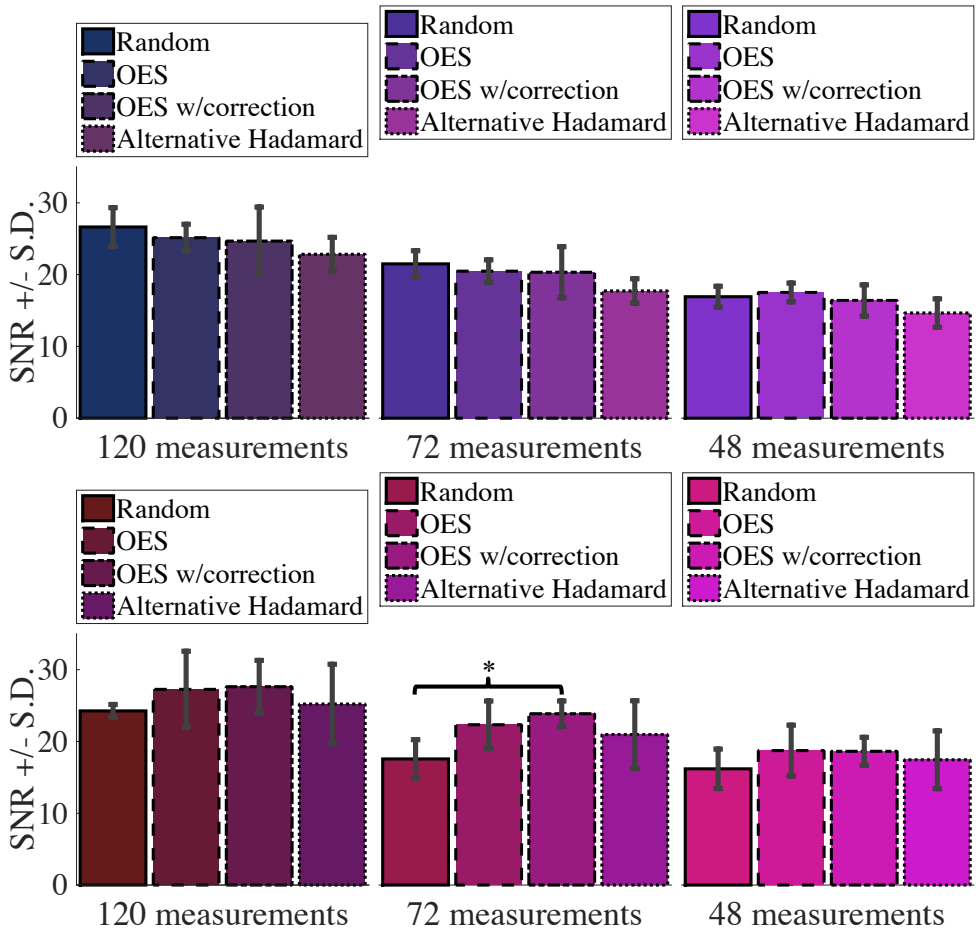


Figure 5.12: Mean SNR ± standard deviation of the perfusion signal across subjects and vascular territories for the cerebral arteries identified in the labelling plane (top row) and the cerebral and scalp arteries identified (bottom row).

signment of vascular territories but very little perfusion signal has been assigned to these arteries. This is to be expected, as the extracranial arteries predominantly supply blood to the scalp, as opposed to grey matter in the brain. All other subjects show similar perfusion/angiography results to the one shown in Figures 5.9 – 5.11, with the clearest vascular territory definition provided by the 120 measurement random encoding.

The SNR was calculated across vascular territories and subjects for each encoding scheme, number of measurements used in the analysis and for cases where only the cerebral arteries were included in the analysis (Figure 5.12, top row) and where additional arteries in the scalp were also identified (Figure 5.12, bottom row). Paired t-tests were used to assess the difference between the SNR values for each encoding scheme for a given number of

measurements and vessels in the labelling plane in the analysis.

The bar charts in Figure 5.12 demonstrate that for all encoding methods, analysed with varying numbers of measurements for a given set of vessels in the labelling plane, the SNR across vascular territories is not generally significantly different. There was only one significant difference identified, found using paired t-tests, between random encoding and OES with offset correction ($P = 0.025$) when analysed with only 72 measurements and extra vessels identified in the labelling plane.

For the analyses that included only the cerebral arteries in the labelling there is a trend for the SNR of the random encodings to be greater than for other methods and to have a smaller spread of SNR values. When arteries in the scalp were included in the analysis this became less evident. As expected, the SNR tends to decrease as fewer measurements are included in the analysis.

5.4 Discussion and conclusions

The proposed method for correcting phase offsets in the labelling plane during PCASL and VEPCASL has been shown to work well in simulations, phantom scans and subject scans for four vessels. Significant improvement in the SNR in vascular teritories of healthy subjects was seen following correction for inhomogeneities in the labelling plane (Figures 5.7 and 5.8). Consequently, for labelling planes in the neck, commonly used for whole brain perfusion imaging with PCASL, the technique could be easily implemented to ensure the SNR of the resulting images is minimally affected by sources of off-resonance in the labelling plane. As described in Section 4.3.3, it is important to note that the SNR calculations here used background ROIs outside of the brain. Due to the use of parallel imaging these ROIs will contain noise terms related to parallel imaging and the corresponding reconstruction along with background noise. As noted previously, the SNR values are intended for internal comparison of the tests performed here, as opposed to an absolute measure of SNR.

When labelling more than four vessels the technique described here is robust during simulations and phantom scans. However, when imaging healthy subjects the identification of vascular territories with MAP analysis has been shown to vary between the encoding schemes tested. Additionally, if arteries that contribute signal to the region imaged are not identified the analysis may struggle to correctly assign signal to vascular territories. Here some of the main arteries in the scalp were identified in the labelling plane after imaging and included in the analysis. This did not result in numerous differences in the assignment of vascular territories to the feeding vessels, when compared to the original analysis including only the cerebral arteries (Figures 5.9 and 5.11). If arteries in the scalp were identified prior to VEPCASL, however, they would affect the calculation of the optimised encodings and could lead to a more accurate separation of the vascular territories.

The difficulty in accurately labelling the arteries of interest using OES based methods may be due to the tortuosity of certain vessels in labelling planes above the circle of Willis. For example, in Figure 5.10 the ACAs appear to be well separated by the encodings shown. However, upon inspection of the labelling plane (Figure 5.9) the more anterior ACA (ACA1) is actually at an angle to the labelling plane. Labelling efficiency is dependent to a certain extent on the angle of the artery with the labelling plane [111] and the angulation will also make the artery location less well defined with respect to the encoding, so the ACAs may not be as well separated by the encodings as hoped.

If the encodings are not labelling the arteries as expected then the OES methods are, to a certain extent, equivalent to the random encoding method, but with less encodings applied. This coincides with the result that when fewer random encodings are applied the vascular territories separated out become more similar to those found using the OES methods (Figures 5.9 and 5.11). Additionally, the SNR of the OES methods is not higher than that for random encoding and, as fewer encodings are included in the calculations, the SNR for random encoding both decreases and tends to become more similar to the SNR for the OES based methods. In particular the alternative Hadamard matrix based encodings. Conversely, the vascular territories identified following encoding schemes based on the OES

method do not change greatly as a function of the number of measurements, although the overall SNR of the perfusion signal does decrease as expected.

In general it is difficult to find a labelling plane above the circle of Willis where the arteries are all perpendicular (or close to perpendicular) to the labelling plane. It may be possible to automatically isolate a more suitable labelling plane from 3D TOF data of the region, using vessel segmentation to identify regions where all arteries of interest are approximately perpendicular to the labelling plane. A more sophisticated approach would be to incorporate knowledge of the vessel tortuosity into the choice of encodings.

Perfusion territories above the circle of Willis vary greatly between subjects and there is currently no gold standard method for establishing the 'true' vascular territories at this level in the brain. Whilst single-artery selective ASL methods could be used, they can partially label nearby vessels, especially in regions above the circle of Willis where branches of the middle cerebral arteries are so close to each other, so would not offer clear delineation of the vascular territories. If time is not a constraint then applying many different encodings, as in random encoding [33], produces the most well defined vascular territories (Figures 5.9 and 5.11). The use of a large number of different encodings provides a great deal of data to inform the analysis process, however, the inclusion of encodings with smaller wavelengths could further increase the SNR efficiency of random encoding (Figure 4.11) and help to more easily differentiate signal from arteries that are close together. The vascular territories identified across OES based methods are similar, so the benefits of using an alternative ideal Hadamard encoding scheme are difficult to ascertain outside of simulations. The small differences between the techniques including a phase correction and the OES method without one may be due to the smaller phase offsets at this level in the brain, as compared to the offsets induced in the labelling plane during the acquisition of four vessel data (Section 5.2.4). If a minimal number of encodings is required, such as where readout times are longer and/or scan time is at a premium, the OES method, including phase corrections and using an alternative ideal Hadamard matrix, presents an option for calculating optimised encodings.

Further development of the OES method for more than four vessels would be of benefit to ensure that vascular territory data acquired with these encodings is more reliable. The next steps would include further evaluation of which labelling planes, and how to choose them, are most suitable for using VEPCASL above the circle of Willis and to assess both alternatives to Hadamard matrices as the source of ideal encoding matrices and the inclusion of information on the shape of the arteries in the labelling plane in the calculation of encodings. As mentioned in Section 5.2.1, the pattern of a particular set of arteries in the labelling plane and the choice of which vessels are labelled/controlled during a given cycle affects the ease with which encodings with a high SNR efficiency can be chosen. The development of a method to choose an ideal encoding scheme that takes into account the vessel geometry to a greater degree would likely increase the efficacy of the method. Likewise, including a metric that indicates the tortuosity of a given artery in the labelling plane could help further optimise the process.

Throughout scanning, the phase offsets – both induced through changes to scanner shim settings and those occurring implicitly in the labelling plane – have been assumed to remain constant. Every effort was made to keep the shim settings constant across scans, but it is possible that time delay between assessing the phase accrued in the labelling plane and applying the phase corrected encodings may result in changes to the phase. If there was any extra phase offset due to gradient imperfections, however, we would expect to see the bands of tagging shifted in the phantom scans, which was not observed (Figures 5.6.a, e, i).

As with the original OES method this technique still bases the choice of encodings on the assumption of a sinusoidal encoding function. However, the difference between a sinusoid and the true labelling function is minimal. The vessels are also assumed to be points. It would be possible to account for the actual vessel cross-section size within the labelling plane using TOF data. Currently this would require some off-line analysis during scanning.

In conjunction with VEPCASL the OES method including a correction for phase offsets only requires an additional field map ($\approx$1 minute) to be possible. When used with PCASL, localisation of the vessels in the labelling plane using a TOF scan is also necessary, but

this is often already acquired to help position the labelling plane. Therefore the total increase in scan time is minimal compared to existing off-resonance correction methods for PCASL [17, 107, 108]. Additionally, the other techniques designed to correct for B_0 inhomogeneities have been limited to either a global phase correction or small numbers of vessels [17, 106–108]. However, to ascertain the relative benefits of each technique a direct comparison would be useful as part of future work.

The inclusion of a correction in the optimised encoding scheme for phase offsets makes the technique more robust to off-resonance and allows the choice of a labelling plane anywhere in the head. The technique is applicable to any number of vessels and is suitable for use with PCASL and VEPCASL at any field strength. However, the separation of vascular territories for arteries labelled above the circle of Willis has been found to be difficult. Further optimisation of encodings for the numbers, and geometries, of vessels in these regions in the brain, and inclusion of both cerebral and scalp vessels in calculation of these encodings, may help to make the technique more robust.

Chapter 6

Time-efficient vessel-selective dynamic angiography

Current vessel-selective angiographic methods, both magnetic resonance based (i.e. arterial spin labelling) and otherwise, require either the use of a contrast agent or are prohibitively slow to acquire in a clinical setting (Section 3.2). For magnetic resonance methods, if less data are acquired through undersampling k-space scan times can be reduced.

The choice of readout scheme for a given magnetic resonance angiography (MRA) technique affects both the speed of acquisition and the type of artefacts that appear in the images. Radial acquisition schemes result in more manageable flow or respiration artefacts than Cartesian acquisitions and, when angularly undersampled, the aliasing artefacts take the form of streaks, rather than image ghosting seen with Cartesian trajectories [48]. The position of these streak artefacts relative to each point is dictated by the point-spread-function of the k-space sampling strategy, so there is a region around each point that is free from artefacts associated with it. The size of this artefact-free region is a function of the angular sampling density [48]. The magnitude of these artefacts is proportional to the strength of signal at each point, so if the majority of the signal is at the centre of the image, as in angiography, the major artefacts will be at the edge of the image. As a result, the type of undersampling artefact associated with radial acquisition makes it particularly applicable for angiography, as the data are sparse and streak artefacts are relegated to the edges of images [53, 54].

Ideally, three-dimensional (3D) time-resolved vessel-selective angiograms would be acquired to provide the greatest amount of information on the cerebral vasculature. However, this is not feasible for many clinical applications, especially in an acute setting due to the increased time needed to acquire 3D data. Consequently, the focus of this chapter is to cater for cases where a rapid scan is required, such as acute stroke diagnosis/treatment, to look for occlusions or stenoses and collateral flow in relatively large arterial segments. Vessel-encoded pseudocontinuous arterial spin labelling (VEPCASL) is one method used to obtain vessel-selective time-resolved angiograms. It is particularly suited to applications where scan times have to be short, as it is more SNR-efficient versus single-artery selective methods (Section 3.2.5). In this chapter an accelerated radial acquisition scheme is optimised and compared to a Cartesian scheme to demonstrate the feasibility of reducing the acquisition duration of VEPCASL angiograms to approximately one minute. This will result in better prospects for use of the method in a clinical setting. All scans were acquired using a 3T TIM Verio system (Siemens, Erlangen, Germany), with a 32-channel head coil. All subjects were scanned under a technical development protocol approved by local ethics and institutional committees.

6.1 Sequence implementation

PCASL has been combined with a variety of readout strategies for angiography [8, 38–40, 97]. The initial sequence testing here aimed to develop a suitable radial k-space trajectory for VEPCASL and to assess the benefits of balanced steady-state free precession (bSSFP) and spoiled gradient echo (SPGR) readouts.

6.1.1 Radial k-space trajectory

For two-dimensional (2D) radial acquisition there is a range of possible k-space trajectories (Section 2.4.2). The trajectory used in this work evenly spaces full radial spokes that contain the same number of samples either side of the centre of k-space. The azimuthal angle,

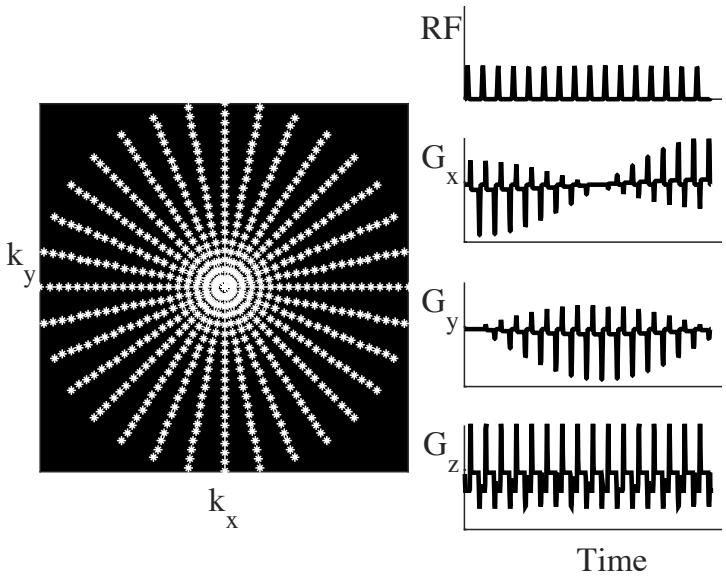


Figure 6.1: k-space data points and the associated RF pulses and gradients for an example 2D radial acquisition (matrix size = 64 x 64, number of spokes = 16, undersampling factor = 6.3). The angle between the acquired radial spokes is constant.

ϕ, of each spoke in the k_x-k_y plane depends on the total number of spokes and whether there are an even or odd number of spokes:

$$\phi_{even} = \pi \cdot {}^{n}/_{N}, \phi_{odd} = 2\pi \cdot {}^{n}/_{N} \tag{6.1}$$

where n = spoke number, N = total number of spokes. These formulae ensure uniform sampling across the azimuthal angle and avoid overlap of spokes running in opposite directions. Figure 6.1 shows a 16 spoke radial trajectory and the corresponding SPGR readout radio-frequency (RF) pulses and gradients.

Instead of acquiring single spokes in k-space after each VEPCASL pulse train, the sequence acquires multiple lines, or a segment, of k-space. The order of segment acquisition can be sequential, i.e. the whole of k-space is progressively acquired for a given VEPCASL cycle [112]. Alternatively, the VEPCASL cycles can be interleaved, such that the same segment of k-space is progressively acquired for all encoding cycles before any further segments [8] (Figure 6.2). Interleaving the encodings aims to minimise the effects of scanner drift or subject motion between encodings to avoid artefacts arising from differences in the static tissue signal. Fewer dummy scans, which normally precede labelling, were applied when

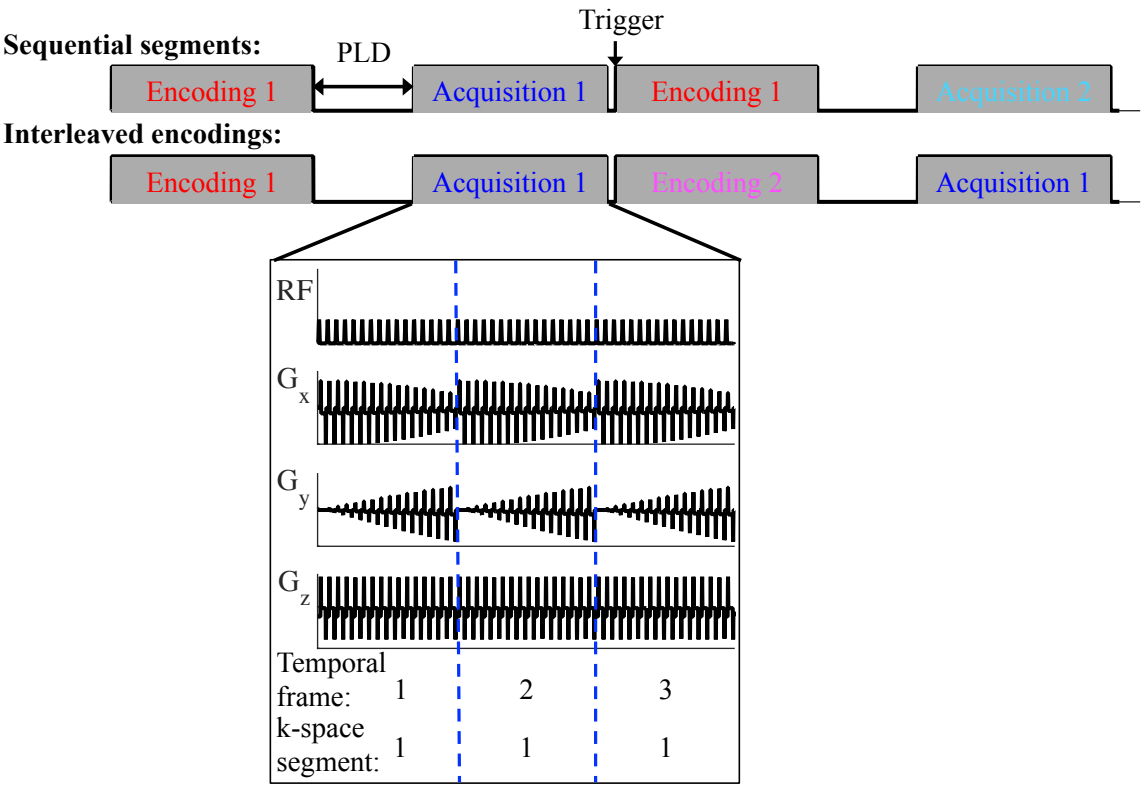


Figure 6.2: Sequence schematic for sequential segment ordering and interleaved encodings. Acquisition number corresponds to the number of the k-space segment acquired. Encoding number refers to the applied (VE)PCASL labelling cycle. The start of the acquisitions can be triggered using a pulse oximeter. PLD = post-labelling delay.

the encodings were interleaved here. This resulted in slightly shorter scan times. Temporal information is gathered by acquiring a given segment multiple times following labelling, to track the flow of labelled blood through the vasculature. The acquisition can be triggered through cardiac gating via a pulse oximeter.

6.1.2 Radial image reconstruction

Online reconstruction (Siemens Healthcare, Erlangen, Germany) based on gridding (Section 2.4.3) is available for this 2D radial acquisition only when the encodings are not interleaved. In order to reconstruct the interleaved acquisitions an in-house reconstruction pipeline was developed around an inverse non-uniform fast Fourier transform (NUFFT) technique. A NUFFT interpolates Cartesian image data onto a non-Cartesian k-space grid,

so the reconstruction here applies an inverse NUFFT to transform radial k-space data onto a Cartesian image grid. There are a variety of NUFFT methods available; the reconstruction here uses a min-max criterion to constrain the interpolation – it seeks to minimise the worst-case approximation between the interpolation and the true image [57]. The in-house reconstruction pipeline has been developed in Matlab® (Mathworks™, Natick, Massachusetts, USA) around NUFFT software from the Fessler Image Reconstruction Toolbox [113].

Radial k-space trajectories result in an uneven sampling of k-space; the centre is more densely sampled. Consequently, when performing a reconstruction such as gridding, and by extension a NUFFT technique, the difference in sampling density across k-space must be accounted for. The radial trajectory used here acquires evenly spaced points along each spoke and the spokes are evenly spaced. As a result the density compensation for each point is proportional to its absolute distance from the centre of k-space [49]. At the centre of k-space, as opposed to a weighting of zero, the density compensation factor is considered to be the area around the sample: $\pi(\frac{\Delta k_r}{2})^2$, where Δk_r is the distance between data points acquired along each spoke [114].

Multi-coil data were acquired for all radial imaging. Online reconstruction uses the sum of squares coil combination technique [115] and in offline reconstruction this was likewise found to yield high quality images and incorporated into the reconstruction pipeline. Scaling of the final image is ordinarily done to fit the dynamic range of both the image display and data storage available [49]. Here scaling was performed to bring the final image intensity onto the order of the images reconstructed using vendor software. The scaling factor was chosen to be a function of the reconstructed voxel size and the applied bandwidth:

$$Scaling factor = \Delta x \Delta y \Delta z \sqrt{\frac{N_{freq} N_{phase} N_{avrg} \times 1000}{BW}} \tag{6.2}$$

where N_{freq} is the number of frequency encoding points per spoke, N_{phase} is the number of phase encoding points on the Cartesian grid the radially acquired k-space is mapped to, N_{avrg} is the number of signal averages taken and BW is the bandwidth per pixel.

Readout parameters					
Protocol number	*1*	*2*	*3*	*4*	*5*
Trajectory type	Cartesian		Radial		
# k space lines/spokes	240	56	360	80	60
Acceleration/undersampling factor	1	4	1	4.4	5.9
Approximate total acquisition time (s)	164	63	239	63	50
Matrix size	224 x 224				
Image FOV (mm)	200 x 200				
Imaging slab thickness (mm)	50				
Readout flip angle (°)	40				
TR (ms)	5.09				
TE (ms)	2.55				
Readout bandwidth (Hz/Px)	475				

Table 6.1: Readout parameters for fully sampled and undersampled Cartesian and radial k-space trajectory bSSFP phantom image acquisitions. NB: radial undersampling factor is with respect to full radial sampling

The time taken for reconstruction varies depending on the level of undersampling in the data being processed. For a typical fully sampled radial trajectory dataset with six time frames, acquired with a 32-channel head coil, the reconstruction time takes less than a minute when performed on a laptop computer with a 3.1 GHz processor.

Phantom validation

To assess the in-house reconstruction pipeline, for both fully sampled and undersampled k-space trajectories, a GE phantom was scanned. Five 2D bSSFP acquisitions were performed, see Table 6.1 for readout parameters. The bSSFP readout was initialised over approximately 100 ms, through a series of twenty RF pulses with linearly increasing flip angles [45]. Fully sampled Cartesian and radial trajectories were acquired (protocols 1 and 3). The number of radial k-space spokes (N_s) is greater than the number of phase encode lines (N_{phase}) for the Cartesian case, in order to satisfy the Nyquist criterion for the radial data and acquire data with the same field-of-view (FOV) and spatial resolution [48] ($N_s = \frac{\pi}{2} N_{phase}$). Time-matched undersampled Cartesian and radial protocols were acquired in approximately one minute (protocols 2 and 4). Although the total acquisition time was matched the acceleration factors are not identical, as the GRAPPA technique requires time during the acquisition to gather calibration data. Finally, a further undersampled radial protocol was acquired (protocol 5), in order to assess the fidelity of the reconstruction for

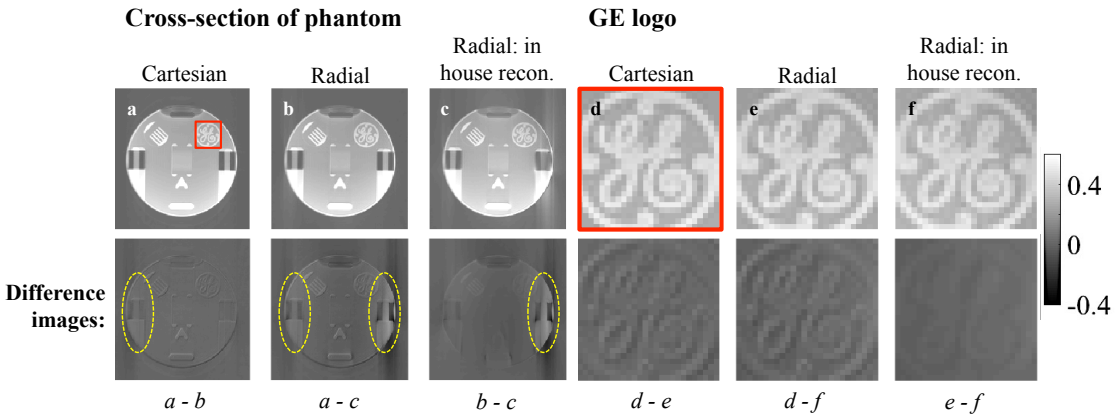


Figure 6.3: **a – c**: Fully sampled phantom images with the subtraction images of the different readout trajectories/reconstructions below. The yellow outlines highlight regions with the largest signal difference. **d – f**: Enlargements of the GE logo structure within the phantom and the corresponding subtraction images. The images were normalised prior to subtraction.

a higher undersampling factor, which is needed in order to push the scan time below one minute. The raw data from all images was reconstructed online using Siemens software. The raw data from the radially acquired images was also taken offline to be reconstructed using the in-house reconstruction pipeline.

Figure 6.3 shows fully sampled Cartesian and radially acquired phantom images, along with the difference images of both the entire phantom and an inner structure depicting the GE logo. The difference images are the result of subtracting the different fully sampled images (intensity scales normalised) from each other. There is visibly very little difference between the internal structures as reconstructed online and offline. The major differences in the reconstructions are at the edges of the phantom (Figure 6.3, yellow outlines). The k-space trajectory in radial imaging can be mis-centred due to delay between the requested and actual gradient start times, leading to this type of artefact [116], and the vendor reconstruction may have more complex trajectory corrections built in to account for this.

Figure 6.4 shows phantom images for accelerated Cartesian and radial acquisition schemes. The acceleration factors are the same as those used in subsequent subject scans, where a GRAPPA factor of four, for Cartesian scans, was the maximum possible acceleration here. Partial Fourier acquisition schemes were not considered in order to keep the Cartesian and

radial readouts more comparable. In Figure 6.4 (top row) there are typical artefacts in evidence for the undersampling schemes. There is a wraparound artefact in the centre of the Cartesian cross-section image (green arrow), a result of the high GRAPPA factor, whilst streak artefacts are in evidence in the radially acquired images. Compared to the GRAPPA artefact, the streak artefacts in the time-matched radial acquisition are further from the centre of the image (yellow arrows). In the more heavily undersampled images the streak artefacts are closer to the centre (orange arrows), which is to be expected, as the size of the central artefact-free region in radially acquired images is a function of the undersampling factor. Difference images of the phantom's internal GE logo are also shown. As with the fully sampled images, there is visibly little difference between the internal structures as reconstructed using vendor software and the in-house reconstruction pipeline. Major differences in the reconstructions remain at the edge of the phantom.

To give a measure of how similar the different acquisitions are the Jaccard distance was calculated between the GE logo sections of the phantom images. The images were normalised to avoid skewing the results due to differences in scaling factors between reconstruction techniques. Only images with similar undersampling factors or time-matched acquisitions were compared. The Jaccard distance is a quantitative measure of how different two images are and was calculated as follows [117]:

$$D = 1 - \frac{\sum_i min(A_i, B_i)}{\sum_i max(A_i, B_i)} \tag{6.3}$$

where i represents the coordinates of pixels in images A and B. The closer to zero the value of D, the more similar images A and B are. The Jaccard distances for the GE logo regions as in Figures 6.3 and 6.4 are shown in Figure 6.5. The Jaccard distances for all comparisons are small. The smallest differences were found between radial images reconstructed with vendor and in-house software. The radial images reconstructed in-house are the most different to the Cartesian acquisitions. However, the degree of undersampling does not affect the similarity of images. The Jaccard distances show the different acquisition strategies and reconstruction schemes to be similar in regions that would be inside the brain, where angiography data are primarily concentrated.

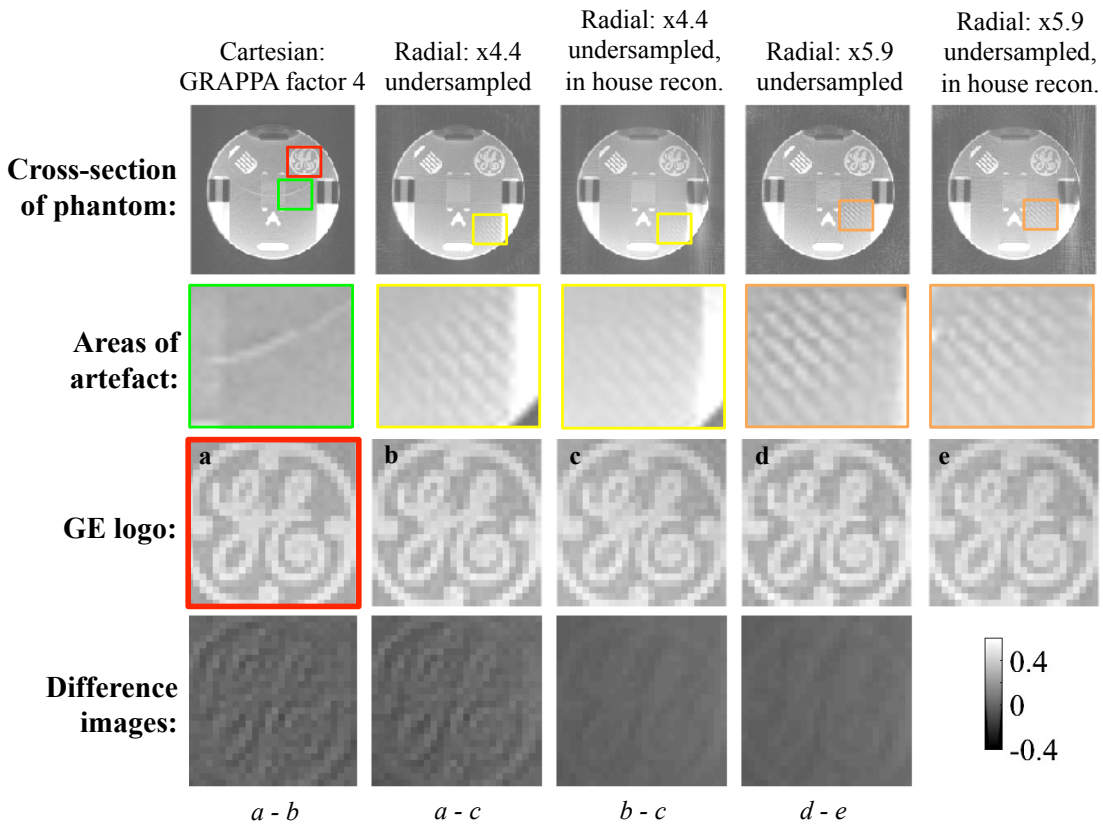


Figure 6.4: Phantom images acquired using accelerated acquisition schemes and reconstructed using both vendor based software and an in-house reconstruction pipeline. Green, yellow and orange boxes, with section enlargements, highlight artefacts due to undersampling. **a – e**: Enlargements of the GE logo structure within the phantom and the corresponding subtraction images. Only subtraction images of equivalently accelerated acquisitions are shown. The images were normalised prior to subtraction.

6.2 Comparison of readout schemes

PCASL angiograms have previously been acquired with SPGR and bSSFP readout schemes [39, 40]. The major requirements for angiograms acquired with accelerated sequences are sufficient image signal-to-noise ratio (SNR) and good vessel definition in a short acquisition time. In comparison to SPGR, bSSFP is more prone to artefacts as a result of local B_0 field inhomogeneities [41], although with a short imaging time artefacts associated with B_0 drift may be less important [118]. Additionally, flow related artefacts in bSSFP sequences are somewhat dependent on the k-space trajectory [119]. However, SPGR results in reduced SNR compared to bSSFP [100], making a comparison of the two readout schemes,

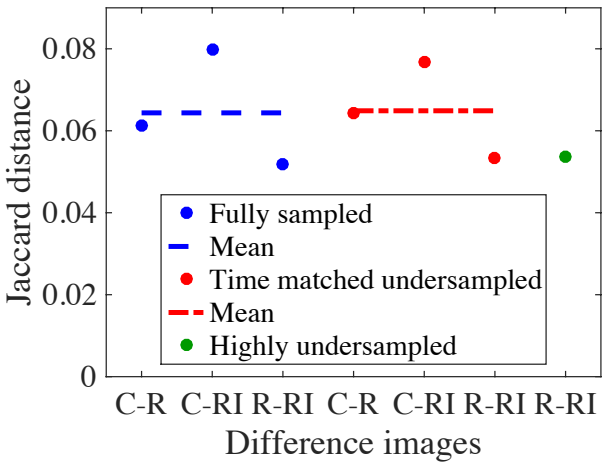


Figure 6.5: Jaccard distances for the phantom GE logo images in Figures 6.3 and 6.4. Fully sampled refers to Cartesian and radial phantom protocols 1 and 3. Time matched undersampled refers to Cartesian and radial phantom protocols 2 and 4. Highly undersampled refers to the radial phantom protocol 5. C = Cartesian, R = radial, vendor reconstruction, RI = radial, in-house reconstruction.

particularly for accelerated radial acquisitions, pertinent here.

A series of protocols were set up to compare similarly undersampled SPGR and bSSFP acquisition schemes. An accelerated Cartesian acquisition scheme was compared to a time matched radially undersampled scheme and a further undersampled radial scheme that can achieve acquisition times of under one minute. The bSSFP protocols were run twice, once with and once without the vendor advanced shim setting. The advanced shim should help mitigate the effects of any off-resonance in the imaging region. However, it takes approximately three times the time required for the standard shim (up to $\approx$ 90 s), as it performs a field map based shim correction three times instead of once. The additional shim corrections work in much the same way as the standard shim process – a field map is acquired and shim coil currents calculated to render the field more homogeneous. The advanced shim repeats this process three times, in order to both check the shimming is making the field more homogeneous and to refine the calculations further to increase homogeneity. Additionally, cardiac gating has been shown to improve bSSFP imaging to a certain degree [93] so was employed during all bSSFP scans.

A healthy male subject (31 years) was scanned. A three-dimensional multislab TOF angiography sequence was performed at the start of the scan to allow selection of a labelling

Readout parameters	**SPGR versus bSSFP**					
Protocol number	*1*	*2*	*3*	*4*	*5*	*6*
Readout type	SPGR			bSSFP		
Trajectory type	Cartesian	Radial		Cartesian	Radial	
# k space lines/spokes	56	84	56	56	80	60
Acceleration/undersampling factor	4	4.2	6.3	4	4.4	5.9
Approximate total acquisition time (s)	88	90	64	63	63	50
Readout flip angle (°)	8			40		
# frames	7	8		6		
Temporal resolution (ms)	101.92	93.94		101.8		
TR (ms)	7.28	6.71		5.09		
TE (ms)	3.59	3.58		2.55		
Readout bandwidth (Hz/Px)	302			475		
Matrix size	224 x 224					
Image FOV (mm)	200 x 200					
Imaging slab thickness (mm)	50					

Table 6.2: Readout parameters for undersampled SPGR and bSSFP subject scans

plane and localisation of the four main brain-feeding arteries in the neck (voxel size = 0.8 x 0.8 x 1.3 mm). A field map of the labelling plane (voxel size = 0.9 x 0.9 x 2.0 mm, TR = 200 ms, TE1 = 5.19 ms, TE2 = 6.19 ms, acquisition time = 1 minute) was acquired and a set of optimised encodings calculated, including a correction for any phase offsets in the labelling plane (Chapter 5). The imaging slab was positioned to include the circle of Willis of the subject. Nine different readout strategies, three SPGR and six bSSFP acquisitions, were used in conjunction with a unipolar VEPCASL [33] pulse train. Labelling parameters were as in Section 5.2.4 for four vessels. Table 6.2 contains the acquisition parameters for the protocols. The further three bSSFP scans acquired were identical to protocols 4-6, but with the vendor advanced shim setting applied.

PCASL MRA has been performed with a range of different temporal resolutions. A value of approximately 100 ms was chosen here, in line with the dynamic ASL bSSFP sequence of Yan *et al.* [38], to provide relatively short temporal resolution but constrain the total scan time. The size of k-space segment that can be acquired after each application of VEPCASL depends on the length of the temporal resolution. The shorter the temporal resolution, the smaller the segment and the more times VEPCASL must be applied in order to acquire the whole of k-space. The SPGR and bSSFP sequence parameters were chosen to best

match the undersampling factors and temporal resolution of the two readout types. Other parameters were then optimised for SPGR/bSSFP image quality. In a steady-state regime the optimum flip angles for bSSFP and SPGR readouts can be calculated based on the T_1 and T_2 values and the Ernst angle respectively (Section 2.4.1) [41]. Here the choice of flip angle becomes a trade off between high initial signal and the level of signal attenuation that is acceptable for the duration of the scan. For an SPGR sequence the signal attenuation, R, at a time t is a function of the flip angle, α, and the TR [120]:

$$R = (\cos\alpha)^{t/TR} \tag{6.4}$$

The SPGR parameters chosen here, with relatively short TR to keep the imaging times short, result in a final signal intensity that is approximately 33% of the original. To minimise banding artefacts in the bSSFP images the TR is kept as short as possible and the flip angle chosen in line with previous bSSFP VEPCASL acquisitions [100]. It is approximately the same as the optimum steady-state flip angle ($\alpha = 41^\circ$ for T_1 = 1.932 s and T_2 = 0.275 s [102]). For the SPGR readout, the minimum TEs for Cartesian and radial acquisitions with the desired undersampling factors were different, as no phase encoding is required with a radial trajectory. This resulted in somewhat different repetition times and temporal resolution.

Figure 6.6 shows the subtraction images of the tag/control all encoding cycles for the three acquisition strategies tested for each k-space trajectory. The bSSFP images are visibly less noisy than the SPGR images and, when the advanced shim was applied, the posterior circulation can clearly be seen in the radially acquired bSSFP images (red arrows). A higher signal was expected in the bSSFP images compared to the SPGR images, due to the greater SNR efficiency of bSSFP, as it reuses transverse magnetisation across excitations [41]. However, most of the posterior circulation is not visible in the bSSFP images acquired without the advanced shim setting. This may be a result of inhomogeneities around the posterior arteries. When there are sources of off-resonance in the imaging region, for example due to an imperfect shim, bSSFP can suffer from flow-related signal changes [121]. As it offers the best imaging of all arteries, versus the comparisons made here, a bSSFP acquisition in conjunction with an advanced shim was used for future scans.

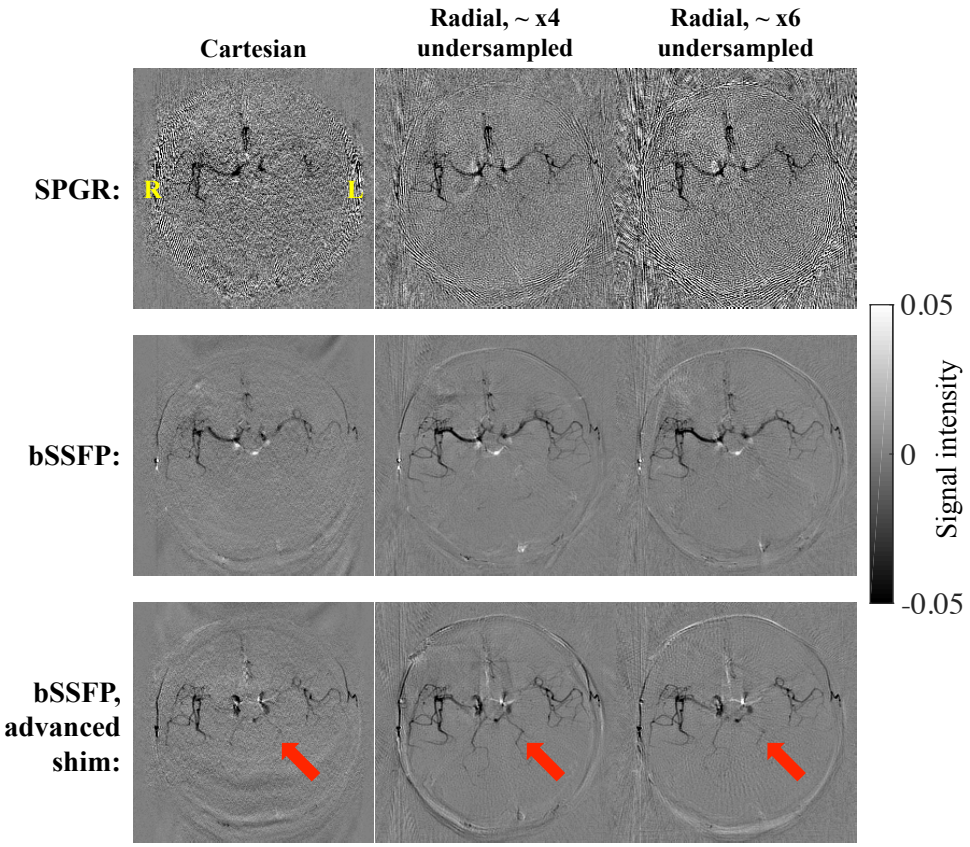


Figure 6.6: Subtraction of the VEPCASL tag and control all encoding cycles, so blood appears dark, for the first time frame of the three accelerated protocols: SPGR, bSSFP and bSSFP with advanced shimming. Red arrows display the posterior circulation visible when using the advanced shim setting.

6.3 Comparison of Cartesian and radial VEPCASL dynamic angiograms

To assess whether an accelerated radial acquisition strategy would be the most appropriate choice for time-resolved vessel-selective angiograms, radial readouts were compared to a time matched Cartesian acquisition strategy.

6.3.1 Subject scans

Acquisition protocol

Six healthy male subjects (mean age 30.3 $\pm$ 4.5 years) were scanned. Five different bSSFP

Readout parameters	**Cartesian versus radial**				
Protocol number	*1*	*2*	*3*	*4*	*5*
Trajectory type	Cartesian	Radial			
# k space lines/spokes	56	80		60	
Acceleration/undersampling factor	4	4.4		5.9	
Approximate total acquisition time (s)	63	63	52	50	39
Interleaved encodings?	X	X	✓	X	✓
Matrix size	224 x 224				
Image FOV (mm)	200 x 200				
Imaging slab thickness (mm)	50				
Readout flip angle (°)	40				
TR (ms)	5.09				
TE (ms)	2.55				
Readout bandwidth (Hz/Px)	475				

Table 6.3: Readout parameters for undersampled Cartesian and radial k-space trajectory bSSFP subject acquisitions

acquisition strategies were used (Table 6.3), similar to those used in Section 6.2. The acquisitions included time-matched Cartesian and radial scans plus interleaved and further accelerated radial acquisitions. The VEPCASL acquisitions were cardiac gated, so the acquisition times listed are the predicted times for each sequence. Some subjects experienced mild peripheral nerve stimulation during the bSSFP scans, but not severe enough to either disrupt or require terminating the scans. All non-interleaved raw images were reconstructed online with Siemens software and all radially acquired images were reconstructed offline in Matlab.

Image analysis

All images were analysed using a Bayesian maximum *a posteriori* (MAP) method [75], as used in Chapters 4 and 5, to separate out vessel specific information. The SNR in the MAP vessel images for each subject, using a somewhat heuristic metric, was then calculated as follows:

1. Mask signal from outside the brain and the scalp (6.7.a)

2. Apply a signal threshold to voxels within the brain mask. Only voxels with signal above the 80^{th} percentile of the data signal across all acquisitions were included. This is to reduce inclusion of voxels away from the main brain-feeding arteries and

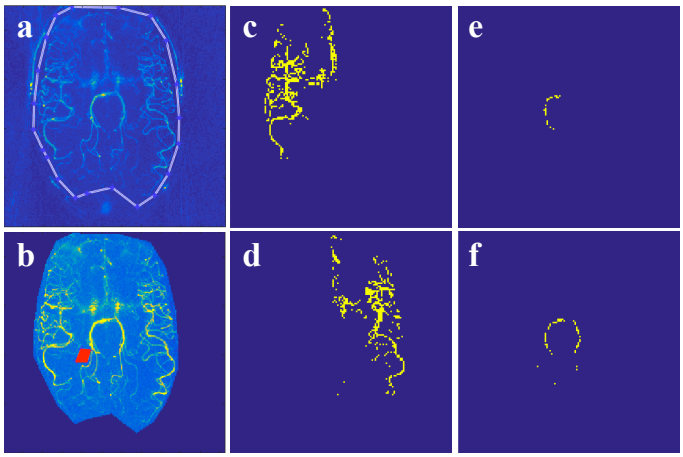


Figure 6.7: An example subject showing **a:** the masked scalp region, **b:** an example noise ROI (red region) and **c – f:** the first time frame signal masks for the four main brain-feeding arteries

ensure the same number of voxels are compared across acquisitions

3. Create vessel specific signal masks according to the dominant feeding artery of each voxel meeting the signal threshold (6.7.c-f)

4. Select a noise region-of-interest (ROI), around 40 voxels, from the centre of the brain of each subject, avoiding any arteries, to assess noise close to vessels of interest (6.7.b)

5. Mean signal was calculated within the vessel mask for each artery and the standard deviation of the noise calculated from the chosen ROI mask. The ratio yields the SNR.

This technique will lead to inclusion of aliased signal in the undersampled images. However, signal from outside the brain is intentionally excluded, as these regions do not convey any information about the cerebral vasculature and, especially in undersampled radial acquisitions, contain large artefacts due to undersampling. Measuring noise outside the head would therefore give an exaggerated estimation of the noise level inside the head. The noise ROI is instead chosen from areas that are close to the arteries of interest inside the brain. In this way the measure of SNR calculated here gives an idea of the strength of the ASL vascular signal as compared to the subtracted static tissue signal, aliased signal and

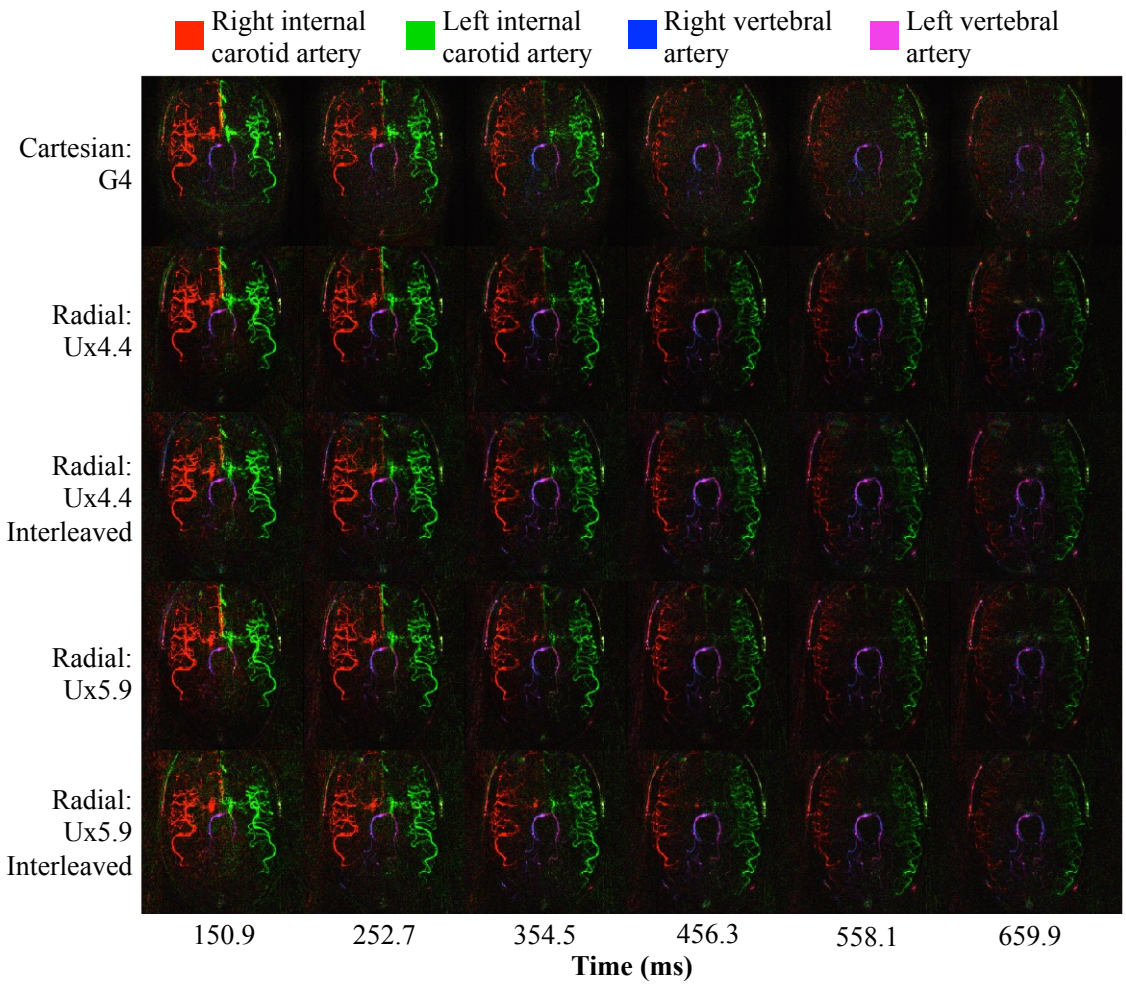


Figure 6.8: Dynamic vessel-selective images for a single subject across five acquisition schemes. Time = time after the end of the VEPCASL pulse train. Radial images without interleaved encodings were reconstructed using vendor software. G = GRAPPA factor, Ux = undersampling factor.

thermal noise close to the arteries. Theoretically, static tissue signal in ASL should be the same across signal acquisitions and so, in the subtraction of ideal ASL acquisitions, static tissue signal would be equal to zero.

6.3.2 Results

Across subjects, scan times of approximately one minute and below were achieved, dependent on the pulse rate of the individual. Figure 6.8 shows the flow of blood through the vessels of one of the subjects. For all acquisitions the arteries are relatively well visualised

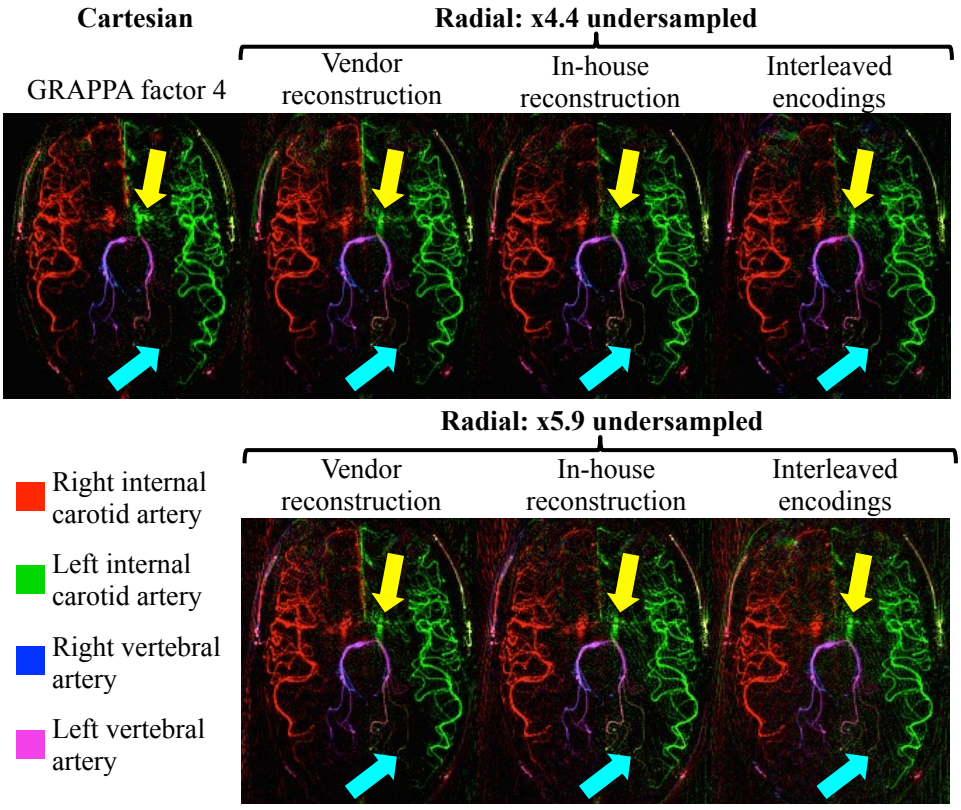


Figure 6.9: Time averaged vessel-selective images for a single subject. Yellow arrows point to smearing of the proximal artery signal. Turquoise arrows indicate signal in the left posterior cerebral artery.

and movement of the blood from the central circle of Willis to the peripheral circulation over time can be seen. The posterior circulation has a delayed arrival time, which is consistent with perfusion data [122]. The more heavily undersampled images are noisier, especially around the eyes. In the time-matched Cartesian and radial images, however, there is a greater degree of noise in the centre of the Cartesian images.

Figure 6.9 contains the time averaged vessel-selective images for a single subject across the five acquisition schemes. Minor streak artefacts are in evidence at the edges of all of the radially acquired images, particularly when only 60 spokes were acquired (x5.9 undersampled). There are also artefacts at the centre of the images, including smearing of the proximal artery signal around the circle of Willis (yellow arrows). The turquoise arrows in Figure 6.9 highlight signal in the left posterior cerebral artery, which is almost negligible in the Cartesian acquisition but can be identified in all the radially acquired images. Figure

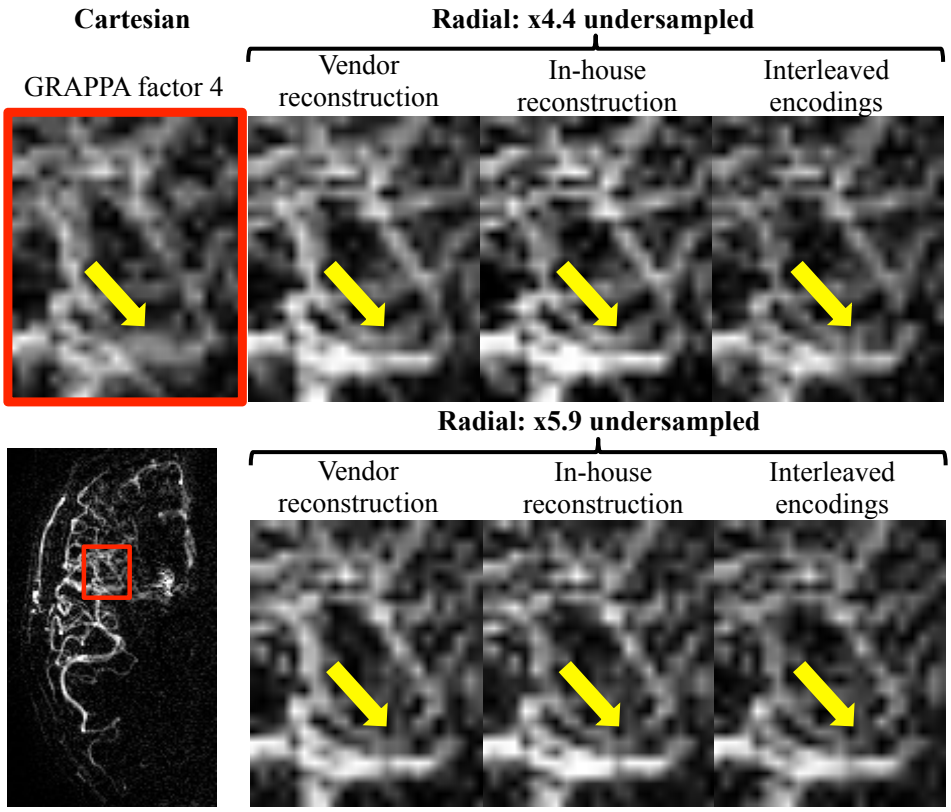


Figure 6.10: Enlarged sections of time averaged right internal carotid artery images for a single subject. Areas of differing vessel definition (yellow arrows) are highlighted.

6.10 shows an enlarged section of the time averaged right internal carotid artery images for the same subject as in Figures 6.8 and 6.9. The yellow arrows indicate the reduced SNR and vessel definition of the Cartesian acquisition towards the centre of the image, which is to be expected with a GRAPPA accelerated sequence [123]. This is in comparison to the time-matched radial readout with both online and offline reconstruction. The in-house reconstruction of the interleaved acquisition with 80 radial spokes has resulted in vessel definition that is improved compared to the Cartesian acquisition, but not as defined as images following non-interleaved encodings. Further radial undersampling has also resulted in reduced vessel definition compared to the 80 spoke radial acquisition.

The SNR was calculated for all five acquisition strategies, including the radially acquired images reconstructed with the in-house reconstruction, regardless of whether the encodings were interleaved or not (Figure 6.11). According to paired t-tests the mean SNR across all Cartesian acquisitions is significantly lower than the mean SNR for all radial

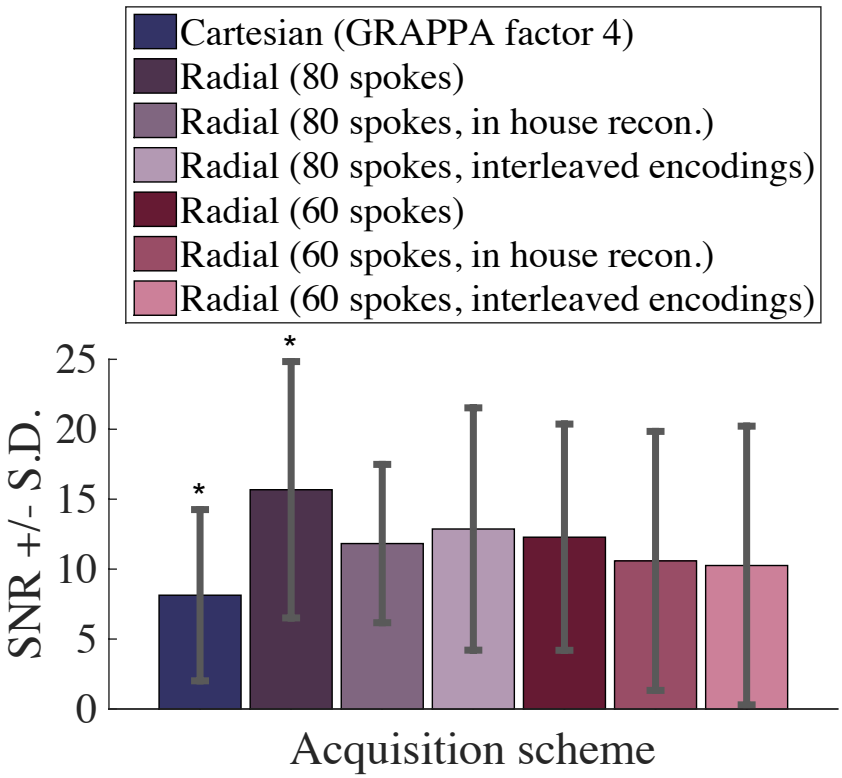


Figure 6.11: Bar chart of the mean SNR across vessels for all different acquisition and reconstruction schemes. Asterisks indicate acquisitions with SNR that is significantly different to the SNR of all other acquisitions shown.

acquisition strategies. For acquisitions/reconstructions using 80 radial spokes, the SNR of the vendor-reconstructed images is significantly greater than the SNR for both the in-house reconstruction ($P \approx 10^{-4}$) and the interleaved encodings ($P = 0.003$). The SNR of both the vendor-reconstructed and interleaved acquisitions using 80 radial spokes is significantly greater than all 60 spoke acquisitions, apart from the interleaved 80 spoke acquisition SNR is not greater than the vendor-reconstructed 60 spoke acquisition. The in-house reconstructed 80 spoke data, however, has not resulted in SNR significantly greater than any of the 60 spoke acquisitions. The SNR of the vendor reconstructed 60 spoke acquisitions is significantly greater than both the in-house reconstructed 60 spoke images ($P = 0.03$) and the interleaved acquisitions ($P = 0.04$).

6.4 Discussion

We have shown here that it is possible to acquire vessel-selective dynamic angiograms in one minute and under with both accelerated Cartesian and radial readouts. The Cartesian readout with high GRAPPA factor suffered from reduced SNR towards the centre of the brain, around vessels of interest. Radial undersampling, however, led to increased noise at the edges of the FOV due to streak artefacts, but away from these vessels. As a result the time-matched radial acquisition had a two-fold better SNR than the Cartesian acquisition within the major cerebral vessels. Increasing the undersampling factor for the radial acquisition resulted in vessel-selective angiograms with increased streak artefacts, but the peripheral arteries were still better delineated than in accelerated Cartesian acquisitions (Figure 6.10).

For all acquisition schemes tested artefacts were visible at the centre of the images around the circle of Willis (Figure 6.9, yellow arrows). These may be a result of pulsatile blood and/or cerebrospinal fluid flow. Cardiac gating can minimise distortions due to pulsatile flow [93], however, there is a delay between the cardiac trigger and image acquisition that could result in acquisition at a suboptimal point during the cardiac phase. Moreover, B_0 drift, due to gradient heating over time during the scan, is another potential source of frequency offset [118]. If sources of off-resonance remain in the imaging slab then flow-related artefacts may still appear. A real-time B_0 drift correction could help improve the bSSFP sequence used here, although the short scan time also helps to minimise the size of any drift.

Artefacts in the images can also affect the ability of the MAP analysis to correctly separate vessel information. Signal from artefacts can lead the MAP analysis to erroneously shift vessel locations in the labelling plane and consequently attribute vascular signal to the wrong feeding artery. An adjustment to the positioning of the imaging slab could help to mitigate these artefacts around the circle of Willis by avoiding the most pulsatile regions of the brain. However, this could affect the imaging of all vessels of interest. Further investigation of the artefacts in the centre of the images is necessary, but the current protocol

could be particularly useful in cases where information about the peripheral vasculature is of interest, for example, in assessing distal occlusions or visualising arterial flow into an arteriovenous malformation higher up in the brain.

Images reconstructed using the in-house software were similar to the vendor-reconstructed images in central regions. There were greater differences towards the edge of the images, but angiograms are typically concerned with information in the centre, so these differences did not interfere with the quality of the angiograms. The greater SNR in vendor-reconstructed images for the same data may be due to additional smoothing or filtering applied during the image reconstruction that is not used in the in-house pipeline.

Interleaving the encodings during radial acquisitions has not shown an increase in SNR of the resulting vessel-selective images, even when compared to non-interleaved images reconstructed in-house. The use of interleaved encodings should help minimise the effects of scanner drift and subject motion. However, the effects of these are likely to be minimal for the short scan times used here. As a result the SNR of the interleaved and non-interleaved acquisitions is equivalent. For vessel-selective angiograms acquired in approximately a minute, interleaving the encodings does not offer any gains in SNR and currently prevents the reconstruction of the acquired images using vendor software. Interleaved encodings are likely to be of use where there are longer scan times, as the effects of scanner drift become more significant and subject motion is more likely.

The measure of SNR at the moment is somewhat qualitative. It allows aliasing signal from undersampling to be included, which could both erroneously increase the vascular signal and affect the noise measure. However, the effect on the mean signal is likely to be small, as the aliasing in the centre of the brain is not severe in these images and will in fact both add to and subtract from the signal. Moreover, the aliased signal will contribute to the noise in ROIs close to the arteries in such a way as to include information on signal fluctuations not due to local vascular signal. A way of improving the assessment of SNR would be to create a more accurate vessel mask, giving a truer estimate of vascular signal. At the moment the mask is based on signal thresholding, however vessels can be extracted from angiographic data using a wide range of techniques [124]. One example would be a

segmentation algorithm, where the start of a vessel is seeded and then the algorithm follows the structure of the vasculature according to the signal in voxels around the seed location. This would avoid the inclusion of signal from voxels not connected to the vascular tree, which can occur with thresholding if a particularly noisy voxel meets the signal threshold.

Whilst the angiograms here can take as little as one minute to acquire, the set-up for this method requires TOF and field map data of the labelling plane and use of the advanced shim, all of which add to the total scan time. A number of steps could be taken to reduce the overall scan time. For example, alternative ways of choosing the labelling plane could be employed, such as fixing the location at a particular distance below either the anterior commissure-posterior commissure line or the bottom of the cerebellum [16]. This would avoid acquiring TOF data, which contributes the most scan time. Additionally, adjusting the location of the imaging region could reduce the need for the advanced shim by acquiring data in a more homogeneous region in the brain.

6.5 Conclusions

To reduce the scan times for vessel-selective angiography an undersampled radial acquisition scheme is shown to be preferable to an accelerated Cartesian scheme. Both the vessel SNR and definition are superior.

The next stage of this work would be to increase its robustness in proximal vessels before assessing its utility through clinician scoring of the angiograms for their usefulness in a clinical setting. Additionally, the inclusion of the protocol on a patient population would better evaluate its ability to provide dynamic vessel-selective information in diseased cerebral vasculature.

The focus of this chapter has been time-resolved angiograms with vessel specific information for four arteries. This work could easily be extended to more than four vessels. The optimised encoding scheme technique with off-resonance correction (Chapter 5) is able to generate a minimal number of optimised encodings for any number of vessels. Consequently, the number of encoding cycles can be tailored to the number of vessels of interest

and so kept to a minimum. The result of this would be relatively short total scan times for multi-vessel dynamic angiographic information.

Chapter 7

Vessel-selective three-dimensional dynamic angiography

Three-dimensional (3D) angiography allows the cerebral vasculature to be viewed and analysed across multiple directions. This can provide increased precision in diagnosis and treatment of patients with cerebrovascular disease [9, 10].

Arterial spin labelling (ASL) based 3D cerebral angiography has previously been performed by combining a hybridised pseudocontinuous (PCASL) and pulsed ASL (PASL) sequence [96] with 3D radial sampling schemes. Most notably a Vastly undersampled Isotropic Projection Reconstruction (VIPR) spoiled gradient echo (SPGR) readout [40] and a balanced steady-state free precession (bSSFP) readout that uses an alternative, but similarly undersampled, 3D radial scheme [39].

Undersampled 3D radial trajectories have been suggested for angiography as the desired data is sparse in the image domain and streak artefacts that result from undersampling do not interfere greatly with the image features of interest, i.e. the vessels. Three-dimensional vessel-selective angiography requires adequate SNR throughout the vasculature and good vessel definition in order to allow analysis of the flow from different vessels across the brain. The combination of current 3D acquisition strategies with VEPCASL, to acquire vessel-selective angiograms, would result in prohibitively long scan times, even outside of an acute clinical setting. Consequently, this chapter aims to develop a protocol that can

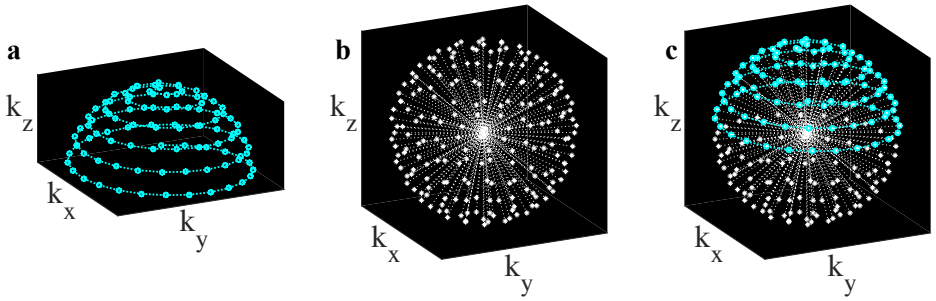


Figure 7.1: 3D radial trajectory. **a**: The ends of the projections in k-space form a spiral around the k-space sampling volume. **b**: Full projections are acquired across k-space. **c**: Both the helical trajectory and the points acquired in k-space are shown.

acquire 3D, time-resolved, vessel-selective angiograms with adequate spatial resolution in acceptable scan times.

The radial protocol as described in Chapter 6 was the basis for the 3D sequence. It was adapted to determine the most suitable 3D trajectory and readout scheme to use with VEPCASL. All scans took place on a 3T TIM Verio system (Siemens, Erlangen, Germany), with a 32-channel head coil. All subjects were scanned under a technical development protocol approved by local ethics and institutional committees. A 3D time-of-flight angiography sequence was performed at the start of all (VE)PCASL scans to allow selection of a labelling plane bisecting the four main brain-feeding arteries in the neck (voxel size = 0.8 x 0.8 x 1.3). VEPCASL pulse train parameters as in Okell *et al.* [8] were used for VEPCASL and PCASL acquisitions (only label/control all cycles acquired).

7.1 Sequence development

7.1.1 Radial k-space trajectory

There is a range of possible 3D radial k-space trajectories. The trajectory chosen here, to combine with VEPCASL, evenly spaces full projections across k-space. A similar trajectory has been used with standard PCASL for cerebral angiography [39]. The ends of the projections are uniformly distributed points across a k-space sphere, calculated according to an algorithm developed by Rachmanov *et al.* [125]. They travel round the surface in a

spiral (Figure 7.1). The uniformity of distribution takes any undersampling into account to keep the projections evenly distributed. The projection acquisition order follows the sweep of the spiral around k-space. For N projections, the polar (θ) and azimuthal (ϕ) angles of the nth radial spoke are calculated as follows:

$$\begin{gathered} \theta_n = \cos^{-1}(h_n) \\ \phi_n = mod\left(\phi_{n-1} + \frac{3.6}{\sqrt{2N(1-h_n^2}}, 2\pi\right), \phi_1 = \phi_N = 0 \\ h_n = \frac{n}{N} - 1 \end{gathered} \tag{7.1}$$

A non-selective RF pulse is applied to excite the entire head and neck before the acquisition of k-space. Similarly to the 2D radial sequence (Chapter 6), the 3D sequence acquires multiple lines of k-space, or a segment of k-space, after each VEPCASL pulse train. Likewise, the order of segment acquisition can be sequential or interleaved by encoding. In this way the same segment for all VEPCASL cycles can be acquired before moving on to the next. Due to the greater acquisition time inherent with a 3D acquisition of this kind versus the 2D case – there are thousands more k-space spokes to be acquired in order to satisfy the Nyquist criterion (Section 2.4.2) – the effects of scanner drift or subject motion are likely to have a greater effect on the resulting images. Acquisitions without interleaving were attempted but the artefacts in the images resulted in very little visible angiography signal. Consequently, all acquisitions in this chapter use interleaving. Temporal information is gathered by acquiring a given segment multiple times following labelling to track the flow of labelled blood through the vasculature. The labelling/acquisition can be triggered through cardiac gating.

7.1.2 Radial image reconstruction

The reconstruction pipeline for radially acquired images was developed in-house. The 2D reconstruction detailed in Chapter 6, based on the non-uniform fast Fourier transform (NUFFT) software from the Fessler Image Reconstruction Toolbox [113] (Section 6.1.2), was extended to three dimensions. When the NUFFT is used to reconstruct non-Cartesian

Readout parameters				
# k space lines/spokes	3424	2560	2272	2048
Approximate undersampling factor	30	40	45	50
Matrix size	128 x 128 x 128			
Image FOV (mm)	150 x 150 x 150			
Readout flip angle (°)	8			
TR (ms)	5.98			
TE (ms)	2.67			
Readout bandwidth (Hz/Px)	300			

Table 7.1: SPGR readout parameters for four different undersampling factors.

data the variable sampling density of the trajectory must be compensated for. Here each point was weighted by its absolute distance from the centre of k-space and the centre point itself by the volume of the finite sphere around it, $\frac{4}{3}\pi(\frac{\Delta k_r}{2})^3$, where Δk_r is the radial distance between data points, as used by Barger *et al.* [126]. The sum of squares [115] coil combine method was used and the images scaled (Equation 6.2) to bring the absolute values in line with 2D reconstructions (Section 6.1.2). High levels of RAM were required in the reconstruction, for trajectory undersampling factors of 30 or more this was less than 4 gigabytes. Reconstruction was run on 20 parallel nodes of a Sun Grid Engine cluster and processing times for undersampling factors of 30 or more were kept to less than 180 minutes in total. For (VE)PCASL scans, data for each encoding is reconstructed before subtraction to yield angiograms.

Phantom validation

In order to assess the reconstruction a GE phantom was scanned with four 3D radial SPGR acquisitions of varying undersampling factors, see Table 7.1 for readout parameters. All raw images were reconstructed offline using the in-house reconstruction pipeline.

Figures 7.2 and 7.3 show images through cross-sections of the phantom. The detail of the internal structures of the phantom are visible for all undersampling factors, but there are increasing levels of artefact in the centre of the image (yellow arrows). The difference images in Figures 7.2 and 7.3 are subtraction images focussing on the GE logo and CS symbol in an x-y and x-z plane of the phantom respectively. There is little visible difference in these subtraction images. The Jaccard distances (Equation 6.3) between the x30 under-

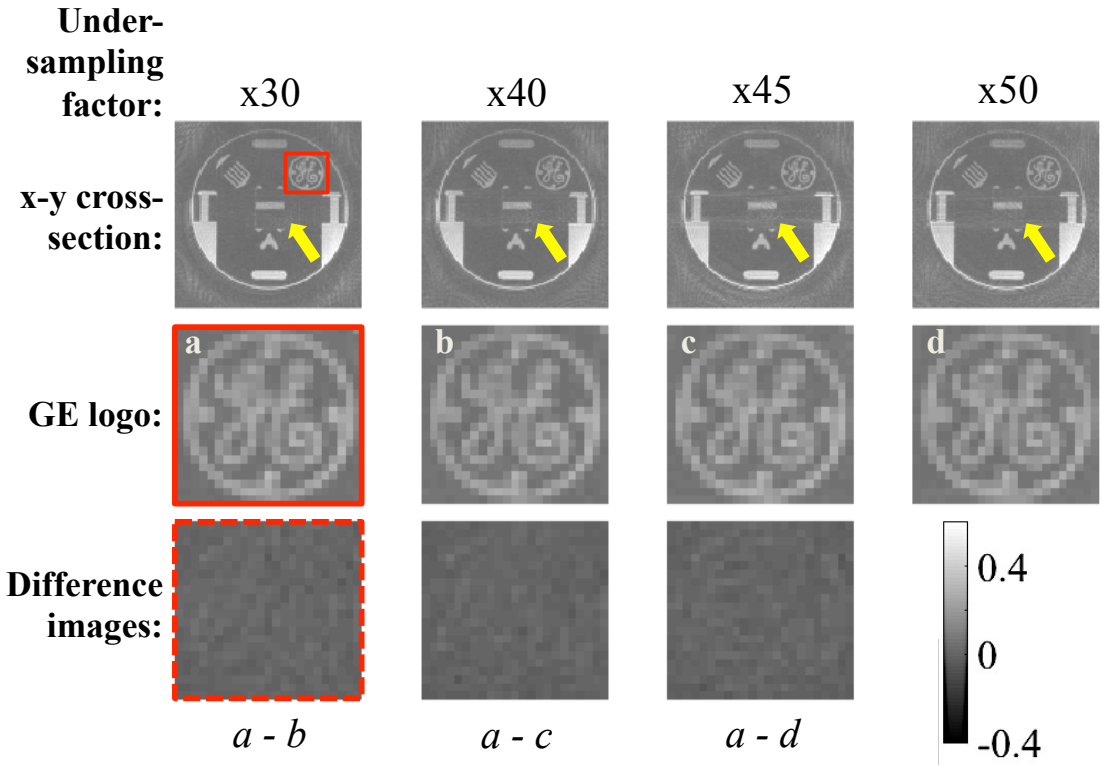


Figure 7.2: Cross-section images of a GE phantom acquired with four different undersampling factors. The difference images show the subtraction of the highlighted GE logo for the different undersampling factors. The yellow arrows indicate increasing levels of artefact in the centre of the images as the undersampling factor increases.

sampled phantom images and logos and the images acquired with higher undersampling factors were calculated. The Jaccard distance gives a measure of how different two images are, the closer to zero the value the more similar the images, up to a maximum distance of one. The images were normalised prior to calculating the Jaccard distances. The Jaccard distances are in general small (Figure 7.4). The values calculated for the whole phantom images are the greatest, and those calculated across the GE logo cross-section the smallest. This is to be expected, as there is more structure towards the centre of the phantom so the increased undersampling factor will increase the streak artefacts at the edge of the images, leaving the central region less affected. The magnitude of streak artefacts is proportional to signal at the point they are related to and their position relative to that point is dictated by the trajectory angular undersampling [48]. The Jaccard distances show that data collected with different undersampling factors reconstruct into similar images.

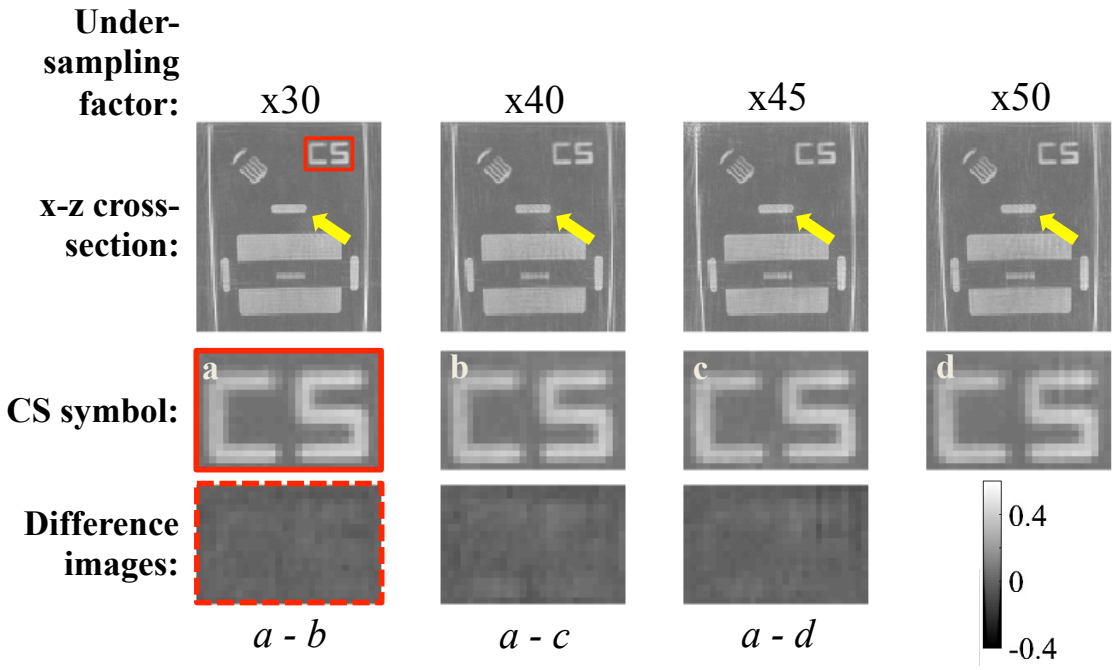


Figure 7.3: Cross-section images of a GE phantom acquired with four different undersampling factors. The difference images show the subtraction of the highlighted CS symbol for the different undersampling factors. The yellow arrows indicate increasing levels of artefact in the centre of the images as the undersampling factor increases.

7.2 Comparison of readout schemes

The combination of PCASL and VIPR for cerebral angiography in a previous study [40] made use of a SPGR readout to avoid the banding artefacts, due to off-resonance, that affect bSSFP and to maintain a lower specific absorption rate. However, PCASL and bSSFP have also been combined for angiography due to the higher signal-to-noise ratio (SNR) of bSSFP [39] and the reduction in RF saturation effects. In Section 6.2 2D bSSFP images acquired in less than two minutes were found to be less noisy than SPGR images. This was as expected, due to the greater SNR efficiency of bSSFP readouts [41]. However, 3D imaging necessitates longer scan times, which can lead to B_0 drift and a shift in resonance frequency that produces banding artefacts in bSSFP images [118]. Additionally, shimming effectively over the entire 3D volume acquired here is non-trivial, which also increases the likelihood of off-resonance in the imaging region, and so banding artefacts. Banding artefacts will strongly attenuate the ASL signal and affect the quality of angiograms. As

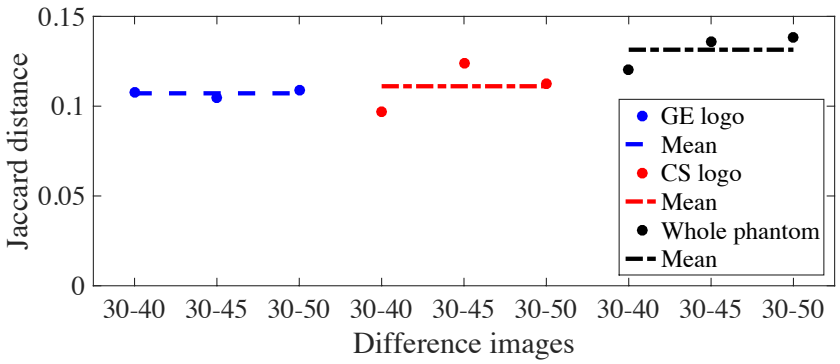


Figure 7.4: Jaccard distances between the GE logo (blue), CS symbol (red) and whole phantom images (black) with different undersampling factors, shown in Figures 7.2 and 7.3.

such, a comparison between the two readout schemes was performed here for the 3D case.

To directly compare readouts a healthy female subject (34 years) was scanned using bSSFP and SPGR readouts in conjunction with PCASL labelling. Only two encoding cycles were acquired during optimisation to decrease the total scan time. The undersampling factor, temporal and spatial resolution of the readouts were chosen to be similar (Table 7.2). As in Section 6.2, parameters were then optimised for SPGR/bSSFP image quality and the bSSFP acquisition was initialised over approximately 80 ms using a series of linearly increasing flip angles [45]. The TR for bSSFP was minimised to reduce banding artefacts and the flip angle chosen, in line with previous VEPCASL acquisitions [100], to offer a high level of initial signal during the acquisition. The TR for the SPGR readout was kept short to help minimise the total scan times and, combined with the chosen flip angle of 10° [8], will result in a final signal of approximately 11% of the starting intensity (Equation 6.4). Both readout schemes were cardiac gated using a pulse trigger, as cardiac gating can help to improve the quality of bSSFP images [93].

To give some measure of SNR, in order to compare PCASL images quantitatively, a similar method to that employed in Section 6.3.1 was used to calculate SNR. Signal masks were found by first using the FMRIB Software Library Brain Extraction Tool [127] to find a binary mask of brain tissue from the reconstructed 3D images. The masks were then manually extended to incorporate signal at the base of/below the brain, which includes

the entirety of the circle of Willis and the top of the internal carotid arteries. The SNR calculation was then as follows:

1. Mask signal from outside the brain
2. Apply a signal threshold to voxels within the brain mask. Only voxels with signal above the 99^{th} percentile of the data signal across all acquisitions being compared were included. This is to reduce inclusion of voxels away from the main brain-feeding arteries and ensure the same number of voxels are compared across acquisitions
3. Select a 3D noise region-of-interest (ROI), on the order of 1000 voxels, from the centre of the brain of each subject before the signal threshold is applied, avoiding any arteries, to assess noise close to vessels of interest
4. Mean signal was calculated within the vessel mask and the standard deviation of the noise calculated from the chosen ROI mask. The ratio yields the SNR.

As in Chapter 6 this technique will include aliased signal in the undersampled images. However, signal from outside the brain is excluded in an effort to reduce inclusion of streak artefacts that do not contain any information about the vasculature. Additionally, measuring noise outside the head, where large streak artefacts are in evidence, would give an exaggerated estimation of the noise inside the head. A noise ROI close to the arteries of interest indicates the strength of the ASL vascular signal compared to the subtracted static tissue signal, aliased signal and thermal noise close to the arteries.

Figure 7.5 shows axial maximum-intensity projections (MIPs) of label/control all subtraction images across time frames, following both SPGR and bSSFP readouts. The bSSFP images have more artefact, especially around the eyes where subtraction has not completely removed static tissue. The orange boxes highlight regions where there is signal dropout in vessels in the bSSFP images as compared to the SPGR images. This is likely to be a result of the banding artefact seen in the pre-subtraction bSSFP image (Figure 7.5, yellow arrow). The artefact cuts directly across a region through which the main brain-feeding

Readout parameters	**SPGR**	**bSSFP**
# k space lines/spokes	7880	7878
Approximate acquisition time	18'04 s	13'50 s
Approximate undersampling factor	10	
Matrix size	112 x 112 x 112	
Image FOV (mm)	160 x 160 x 160	
Readout flip angle (°)	10	40
Temporal resolution (ms)	114.8	100.62
# temporal frames	6	
TR (ms)	5.74	3.87
TE (ms)	2.57	1.94
Readout bandwidth (Hz/Px)	300	475
PCASL duration (ms)	800	

Table 7.2: Imaging parameters for SPGR and bSSFP readouts following PCASL encodings.

arteries flow. There is stronger signal in some of the peripheral vessels in the bSSFP images versus the SPGR images. However, in the bSSFP images some bright signal remains in the centre of the brain, near the brainstem, across time frames. Due to the high T_2/T_1 ratio of cerebrospinal fluid (CSF) it appears bright on bSSFP images [128] and the pulsatile motion of CSF at this level in the brain [129] could account for signal remaining after the subtraction of ASL acquisitions.

SNR calculations were performed, firstly as detailed above and secondly in a similar way, but using an alternative signal mask. The alternative masking did not manually adjust the masks found using brain extraction, so signal from lower down the neck and the extracranial arteries was excluded, with the aim of excluding the bright central artefact seen in the bSSFP images (Figure 7.5, bottom row).

Calculations of SNR across time frames (Figure 7.6.a) show how the SNR of the bSSFP images does not fall steadily over time as it does for the SPGR images, regardless of whether the bright central artefact is excluded or not. On inspection of the signal and noise measurements (Figure 7.6.b) it becomes apparent that the signal for both SPGR and bSSFP images decreases steadily over time, with greater overall signal present in the bSSFP case, as would be expected. However, the noise present in the bSSFP images, particularly in the first time frame, is greater than for the SPGR acquisitions.

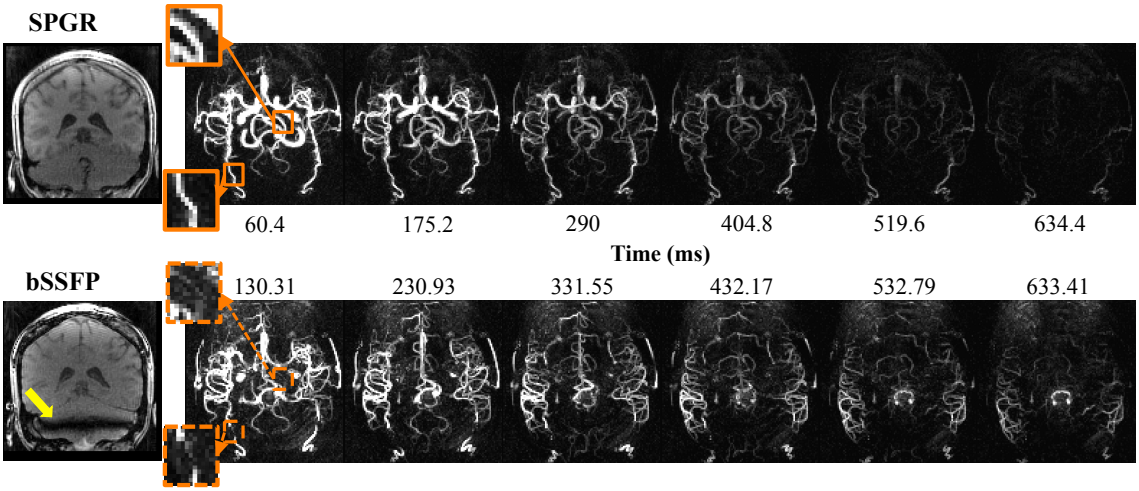


Figure 7.5: Coronal images (pre-subtraction) and axial MIPs following PCASL and SPGR (top row) and bSSFP (bottom row) readouts. The yellow arrow indicates a banding artefact in the bSSFP image and the orange boxes highlight regions of signal dropout in the bSSFP MIPs, as compared to the SPGR MIPs.

The aliasing artefacts will be greater in earlier time frames, as their magnitude is linked to the signal strength, and the noise ROI will include some aliased signal. However, this applies to both the SPGR and bSSFP readout schemes and, although the noise is elevated in earlier time frames for the SPGR acquisition, there is a greater degree of noise in the SPGR case that accounts for the SNR trends in Figure 7.6.a. The standard deviation values in a noise ROI, across time frames, for both the un-subtracted and subtracted ASL acquisitions is shown in Figure 7.6.c to ascertain the time course of the static signal noise before subtraction. Relative to later time frames bSSFP has proportionally higher noise earlier on than the SPGR acquisitions. As such the elevated noise in earlier time frames may be driven by more than just aliasing artefact. It could be affected by the oscillations of the bSSFP signal, which may not have reached the steady state prior to acquisition.

From these subject scans, the bSSFP readout used here was found to be more prone to artefacts over the imaging volume. It is difficult to accurately shim over such a large volume, resulting in the distinct banding artefact seen at the base of the brain that has lead to signal dropout in the MIP images of the subtracted bSSFP PCASL measurements. Additionally, the scan times for 3D acquisitions are long, increasing the likelihood of artefacts due to B_0 drift. Consequently a SPGR readout was used for future scans.

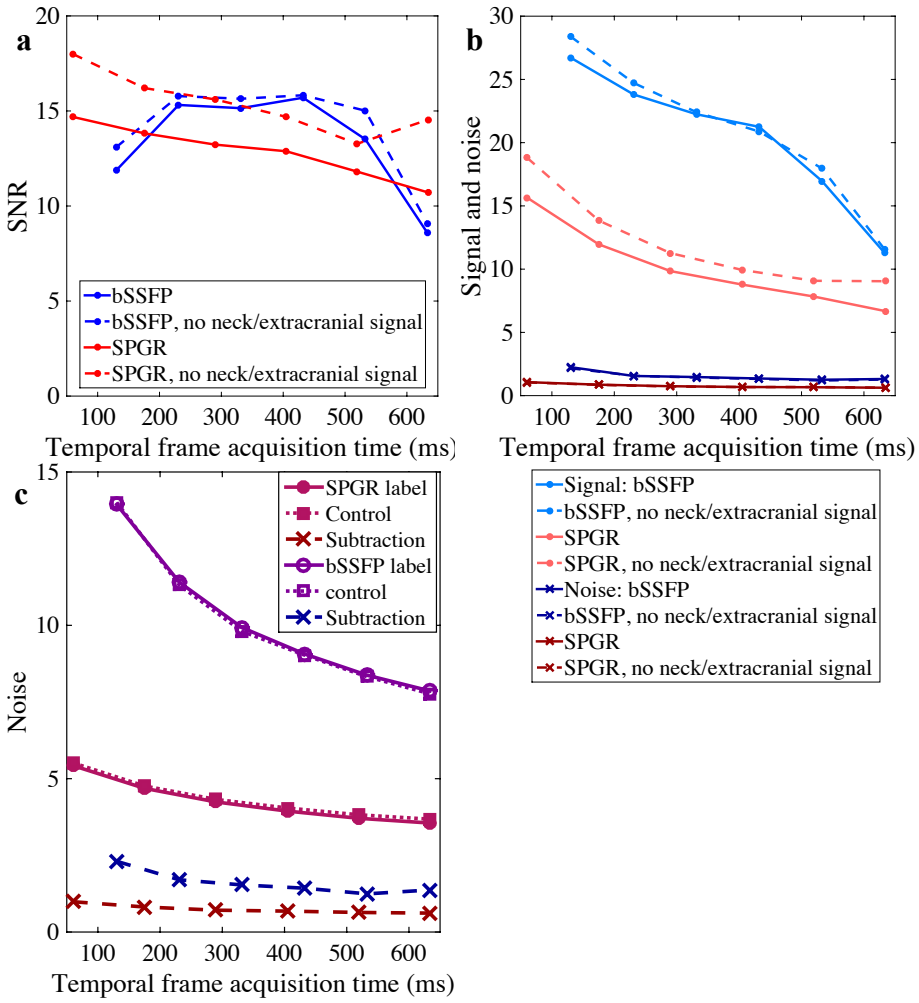


Figure 7.6: **a**: SNR, **b**: signal and noise values for each time frame of the bSSFP and SPGR PCASL subtraction images, calculated using a mask including signal in the neck (solid lines) and without (dashed lines). **c**: Noise values in the un-subtracted and subtracted SPGR and bSSFP PCASL acquisitions.

7.3 Sequence optimisation

Time-resolved 3D VEPCASL angiograms require sufficient signal throughout the acquired time frames to visualise the flow of blood through the vasculature. Dynamic information has previously been achieved using a PCASL-VIPR sequence [95], in which a number of images are acquired with varying contributions of control and labelling pulses, yielding a temporal resolution of 200 ms with 0.68 mm isotropic voxel size (undersampling factor $\approx$ 30). However, this resulted in a scan time, for non-vessel-selective information, of seven and a half minutes. To acquire vessel specific information for the four main brain-feeding

arteries the ideal encoding scheme would consist of eight cycles, as seen in Section 4.2.1, which would increase the scan time fourfold. Consequently, the spatial resolution of the images presented in this chapter is somewhat reduced, to decrease the total scan time whilst maintaining a similar level of temporal resolution. The acceptable levels of signal attenuation and k-space undersampling were both considered during sequence optimisation.

For all following subjects, unless otherwise stated, two VEPCASL encodings were acquired (label/control all) using SPGR readout parameters as in Table 7.1. A subject pulse trigger was not used, instead the time between acquisitions was fixed to minimise any 'dead' time before the next acquisition. This is in line with other VEPCASL SPGR acquisitions, which did not employ cardiac gating [8, 95]. The temporal resolution of the scans was kept around 200 ms, in line with previous dynamic PCASL-VIPR acquisitions [95]. SNR in the subtracted label/control all images was calculated as in Section 7.2.

7.3.1 Signal attenuation

The optimum SPGR repetition time (TR) and flip angle combination that would result in reasonable levels of signal attenuation for ASL signal was considered. A short TR will provide a shorter total acquisition time but requires an increase in bandwidth, and therefore noise, and will increase the rate of signal attenuation. A high flip angle will result in higher initial signal – in earlier time frames – but leads to faster signal attenuation. The magnitude of the ASL signal in the transverse plane, at a given time point t during a SPGR readout, is dictated by the T_1 relaxation of the inverted longitudinal magnetisation [22], the signal generated by the most recently applied RF pulse, with flip angle α, and the signal attenuation that occurs as a result of the readout itself [120] (Equation 6.4):

$$M_{ASL}(t) \propto M_0 \left(1 - 2e^{-t/T_1}\right) (\sin\alpha)(\cos\alpha)^{t/TR} \tag{7.2}$$

Equation 7.2 assumes that all ASL signal will see every pulse in the readout, so the effects of labelled blood flowing into the imaging region after the readout has started are not included. Consequently, this equation may overestimate the rate of overall signal attenuation, but can therefore act as a guide for the maximum expected rate. The effects of potential TR

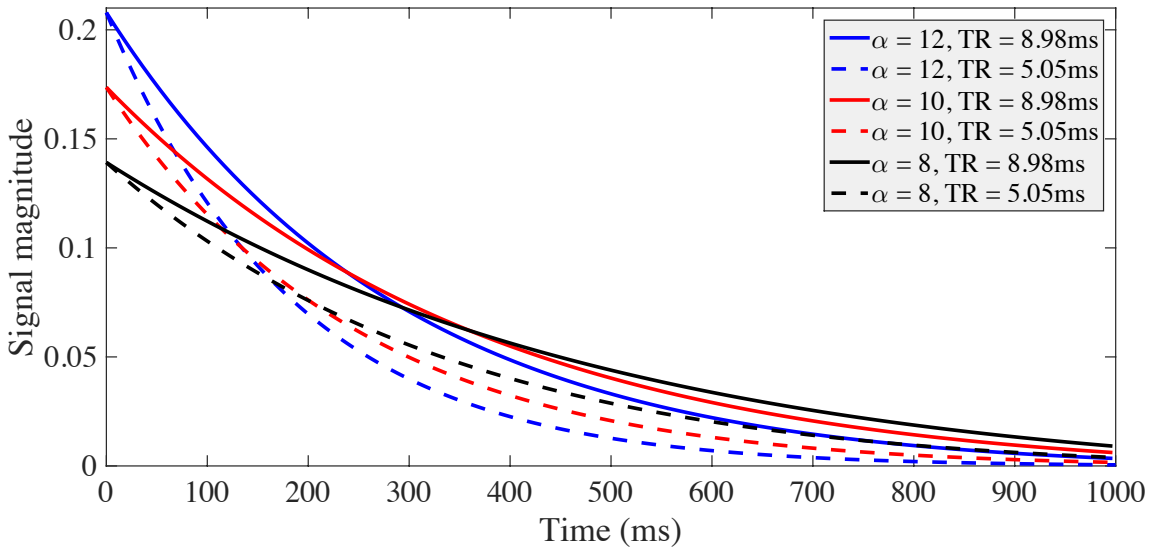


Figure 7.7: ASL signal attenuation calculations due to a SPGR imaging sequence for a range of flip angles and TRs, T_1 = 1.932 s.

and flip angle combinations were calculated in Matlab®. A short TR and flip angle of 10° have been used in PCASL-VIPR acquisitions [40] so a similar combination was compared with alternative flip angles and a longer TR (Figure 7.7). The initial magnetisation was given a normalised value of one and considered to be fully inverted at the start of the calculations. The combination of a longer TR and smaller flip angle produces the least signal attenuation. However, as the smallest flip angle also results in the least initial signal and the longest TR will result in increased scan times, a range of subject scans were also considered to assess acceptable levels of initial signal, signal attenuation and total acquisition times.

Subject validation

Three subjects were scanned using a series of different readout parameters. All PCASL scans had a labelling duration of 800 ms, undersampling factor of approximately 40, matrix size = 128 x 128 x 128 and image FOV = 150 x 150 x 150 mm. The Siemens system used here oversamples k-space by a factor of two during these acquisitions, i.e. a matrix size of 256 x 256 x 256 is acquired, this does not change the acquisition time but prevents aliasing in the FOV of interest.

Subject 1

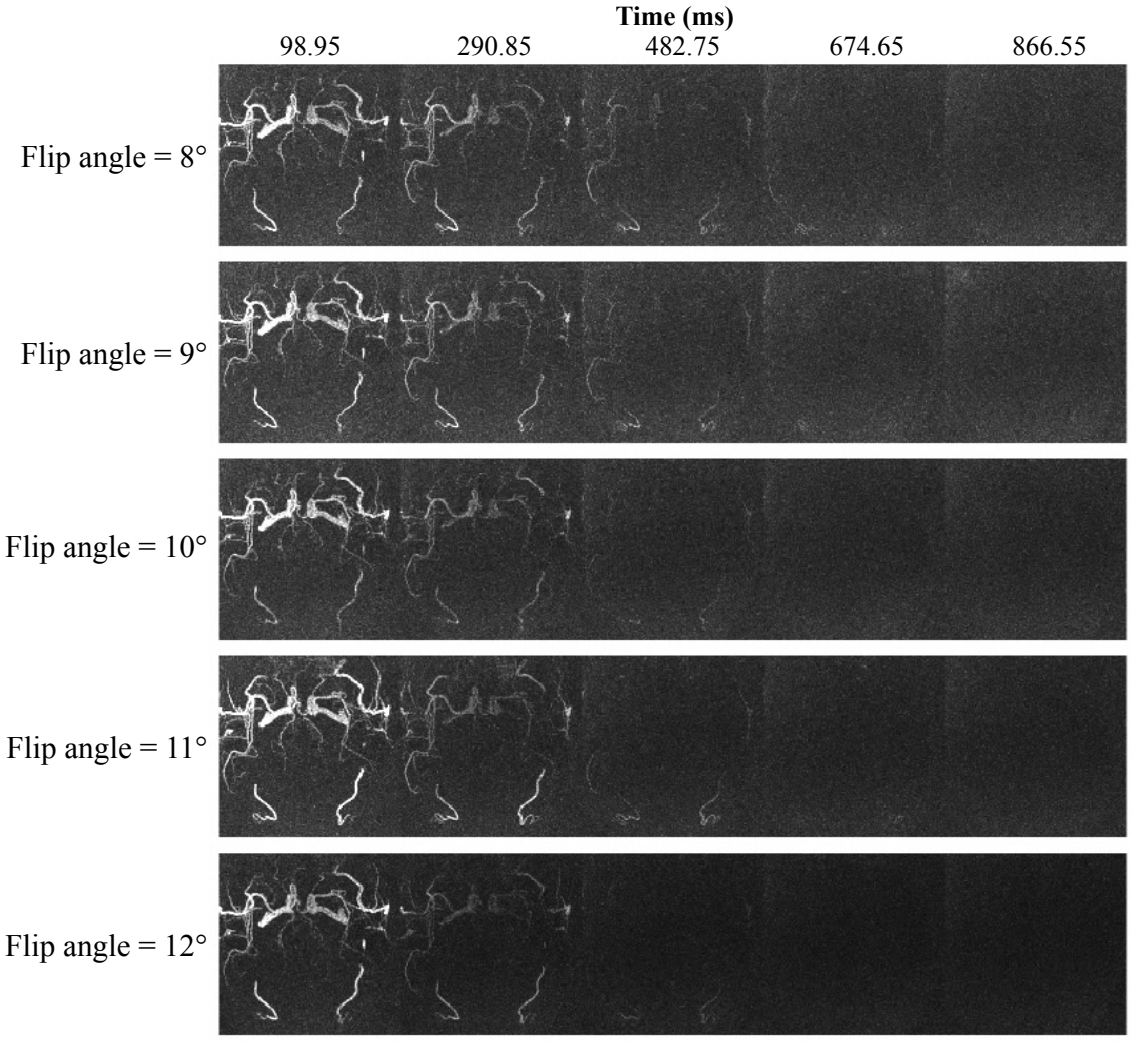


Figure 7.8: Axial MIP images for a series of acquisitions with the same readout TR (5.05 ms) and varying flip angle.

In the first series of scans a short TR, similar to that used in PCASL-VIPR acquisitions [40], was used to gauge the lower limits of potential repetition times. A range of flip angles was chosen to assess whether using a flip angle with greater initial signal or the least signal attenuation would be most effective with the short TR. Five sets of PCASL data were acquired for a healthy male subject (31 years) with TR = 5.05 ms and five different flip angles: 8°-12° (TE = 2.23 ms, readout bandwidth = 420 Hz/Px, acquisition time $\approx$ 4'15 s).

Figure 7.8 shows axial MIPs at various time frames for the data acquired during this subject scan. There is essentially no vascular signal in the latter two time frames for any flip angle. This can most likely be attributed to fast signal attenuation due to the short TR. In Chapter

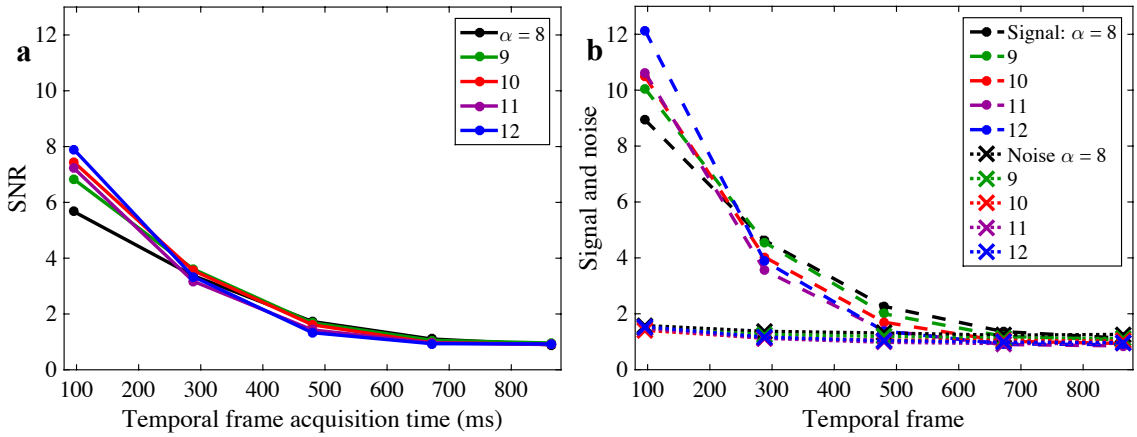


Figure 7.9: Mean SNR of the vascular signal across time frames for five acquisitions with increasing readout flip angle and a repetition time of 5.05 ms.

6 (Figure 6.8) signal was seen in later time frames, consequently the lack of signal here is likely not due to high flow rate of the labelled blood or T_1 decay of the ASL signal. Higher flip angles result in faster signal attenuation, so there is also less vascular signal in the second and third time frames the greater the angle. In the first time frame larger arteries are fairly well defined for all flip angles, but the peripheral vessels are hard to discern. The parameters required for dynamic ASL angiograms must result in less signal attenuation, as compared to the acquisition of a single time frame. Consequently, longer TRs were considered in later scans.

The SNR for the time frames of each acquisition was also calculated (Figure 7.9.a). Only voxels considered to contain signal across acquisitions were considered and the same mask, as defined from the first time frame, was used across time frames. The signal and noise values for these acquisitions are shown in Figure 7.9.b. As expected the signal, and SNR, is greater for larger flip angles. The rate of attenuation of the SNR also appears to be driven by elevated noise values in earlier time frames, as seen in Figure 7.6.

Subject 2

As a consequence of the results from subject 1 a set of scans was acquired for a second subject with a range of TR and flip angle combinations – the minimum TR chosen was greater than in the first scan. The aim was to assess a series of acquisitions, with matched scan times, that could yield improved vascular signal throughout the time frames. Five sets

Readout parameters					
Protocol	*1*	*2*	*3*	*4*	*5*
Approximate acquisition time	5'22 s				
Readout flip angle (°)	8	12	10	8	12
Temporal resolution (ms)	213.6		189	172.2	
# temporal frames	4		5		
TR (ms)	7.12		6.3	5.74	
TE (ms)	3.22		2.82	2.55	
Readout bandwidth (Hz/Px)	224		275	326	

Table 7.3: Imaging parameters for SPGR readouts following PCASL encodings.

of data were acquired for a healthy female subject (28 years), protocol parameters can be found in Table 7.3.

Figure 7.10 shows axial MIP images across acquisitions for the second subject. There is good vessel definition in the first time frame of all acquisitions. However, at higher flip angles (10° and 12°), even with longer repetition times, there is little or no vascular signal in later time frames; the signal attenuation is too great.

SNR calculations across acquisitions with a similar first time frame used the same signal mask across time frames and only voxels containing signal across all acquisitions contributing to the signal mask were considered. The SNR across time frames can be seen in Figure 7.11.a. As seen in Figure 7.7, signal attenuation in the MIP images and SNR calculations is somewhat faster for larger flip angles. However, similarly to results in Figure 7.6.a, the SNR does not fall away as expected over time for the flip angle = 8° acquisitions. Figure 7.11.b shows the signal and noise results for these SNR calculations. The signal falls away over time as expected, but the noise values are elevated in the first time frame. When this is coupled with the slower signal attenuation of the low flip angle scans the SNR does not decrease as fast as expected in the second and third time frames.

The initial SNR of the images is not found to be higher for larger flip angles here, although the starting values are all similar. This may be an effect of the chosen masks, where only voxels including signal across acquisitions are included, and a greater amount of background noise in the initial time frames with a flip angle of 12°, visible to a certain extent in the MIP images.

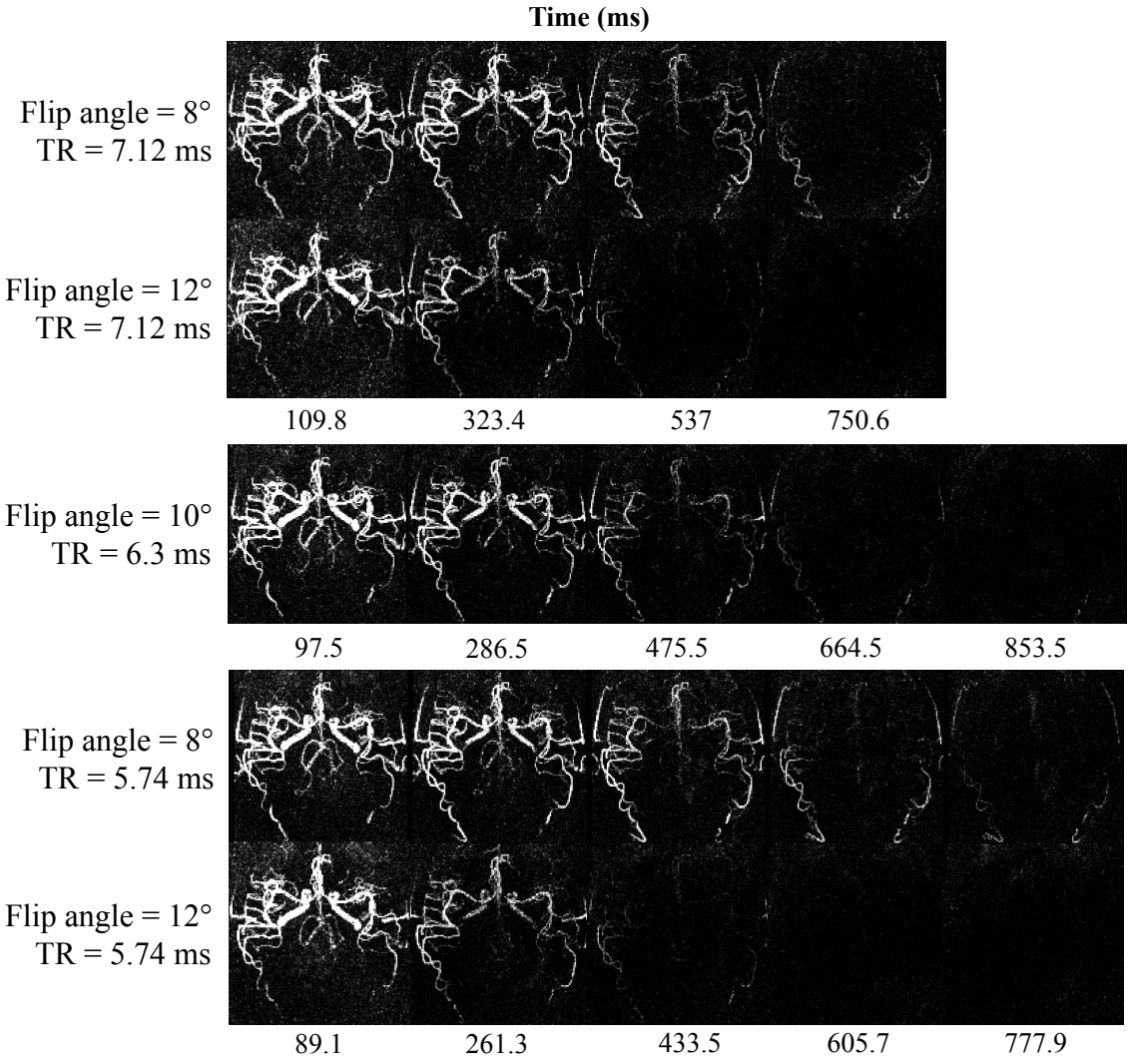


Figure 7.10: Axial MIP images for a series of acquisitions to assess acceptable levels of signal attenuation from a range of readout parameters.

The vessel definition is similar for all acquisitions in the earlier time frames but, due to the lower rate of signal attenuation for flip angles less than 12°, only angles between 8° and 10° are considered in future scans. Although there is still some vascular signal evident in the final time frame for the acquisition with TR = 5.74 ms and flip angle = 8°, the shorter TR here has still resulted in a strong level of attenuation so longer TRs are considered in the following scans.

Subject 3

In the final subject scanned parameters were calculated to match the attenuation for TR =

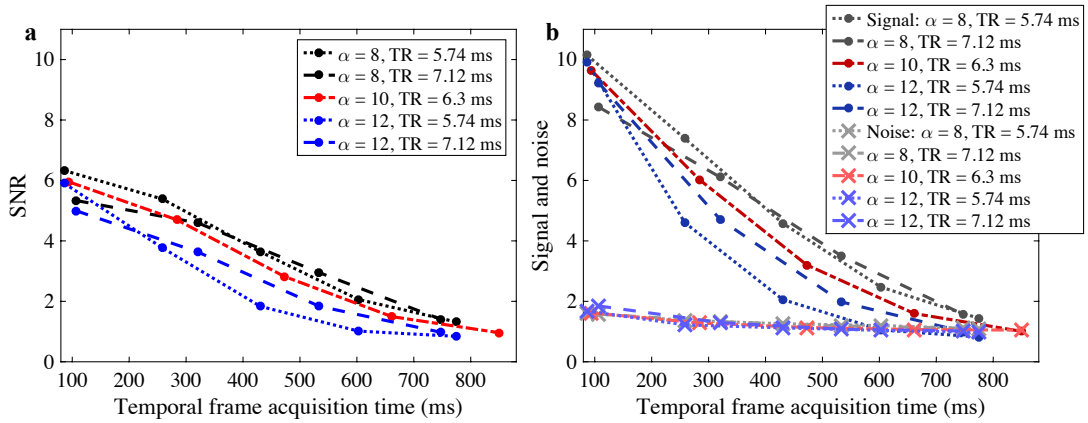


Figure 7.11: **a**: Mean SNR, **b**: signal and noise of the vascular signal across time frames for five acquisitions with differing flip angle and TR.

5.98 ms and flip angle = 8°. These parameters were chosen to provide a flip angle and TR combination with an acceptable level of signal attenuation based on the previous subject scans. Parameters with greater flip angle but matched attenuation were calculated, using the signal attenuation rate term $(\cos\alpha)^{t/TR}$ in Equation 7.2 [120], to assess the benefits of greater overall signal versus longer scan times.

Data were acquired for a healthy male subject (30 years) with three sets of parameters with matched signal attenuation (Acquisition 1: flip angle = 8°, TR/TE = 5.98/2.67 ms, bandwidth = 300 Hz/Px, acquisition time ≈ 4'59 s. Acquisition 2: flip angle = 9°, TR/TE = 7.58/3.44 ms, bandwidth = 202 Hz/Px, acquisition time ≈ 6'23s s. Acquisition 3: flip angle = 10°, TR/TE = 8.98/4.14 ms, bandwidth = 158 Hz/Px, acquisition time ≈ 7'37 s).

In Figure 7.12 the axial MIP images for the above acquisitions show similar vessel definition and signal attenuation across scans. The SNR calculated is similar across time frames (Figure 7.13.a). However, as would be expected, the signal for the different acquisitions is greater for larger flip angles (Figure 7.13.b). The noise values are also correspondingly higher, despite the fact that the bandwidth is higher the lower the flip angle, which will increase the noise level. The noise generated by aliased signal dominates the noise resulting from the higher bandwidth. The combined result is comparable overall SNR values between acquisitions. Higher noise values in earlier time frames, coupled with the lower rate of signal attenuation for these scans, has resulted in similar SNR values over time.

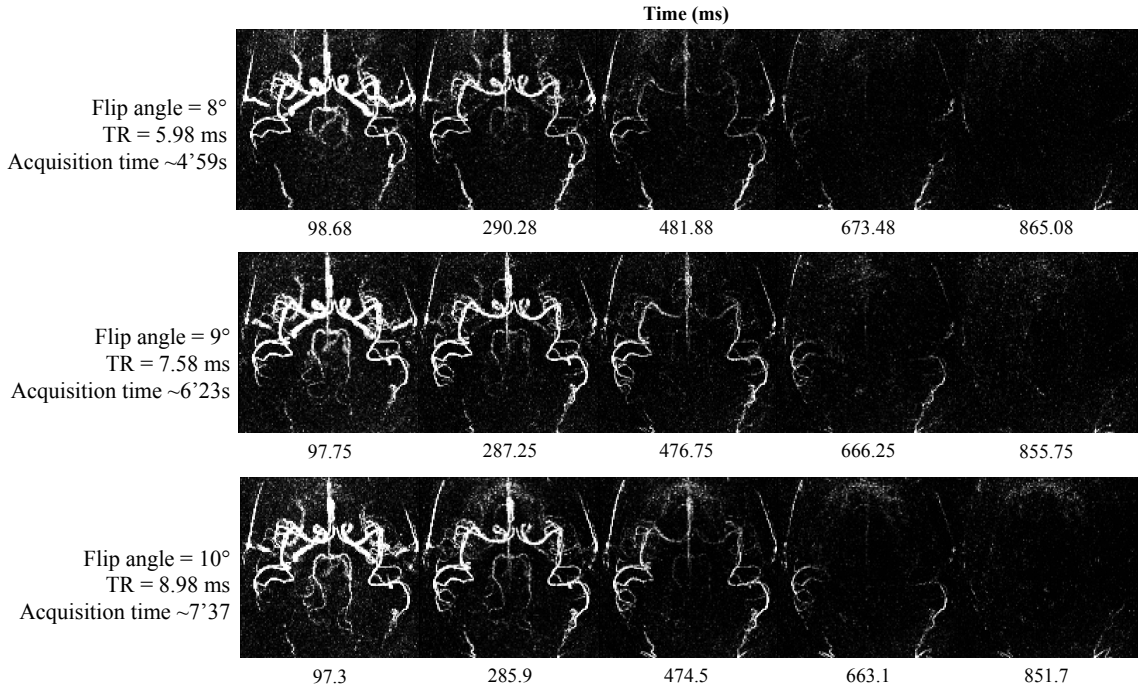


Figure 7.12: Axial MIP images for acquisitions with scan parameters designed to match their signal attenuation.

Matching the signal attenuation of the scan has resulted in angiograms of similar quality. However, due to the increased TR, the scan times of the acquisitions with flip angles greater than 8° are both over six minutes long for only two encodings. To encode four vessels efficiently with VEPCASL eight encodings are required [8] and, with the parameters described above, this would necessitate total acquisition times of more than 24 minutes. Even in a non-acute setting these scan times are prohibitively long. As a result the next section looks at the possibility of further undersampling the 3D radial trajectories for readouts with flip angles of 8° and 9° and matched signal attenuation, so as to decrease the total scan time further.

7.3.2 Undersampling factor

PCASL data from a healthy male subject (25 years) were acquired for six different readout schemes – to compare three levels of undersampling factors (x40, x45 and x50) with two different flip angle/TR combinations that had matched signal attenuation. All scans had a

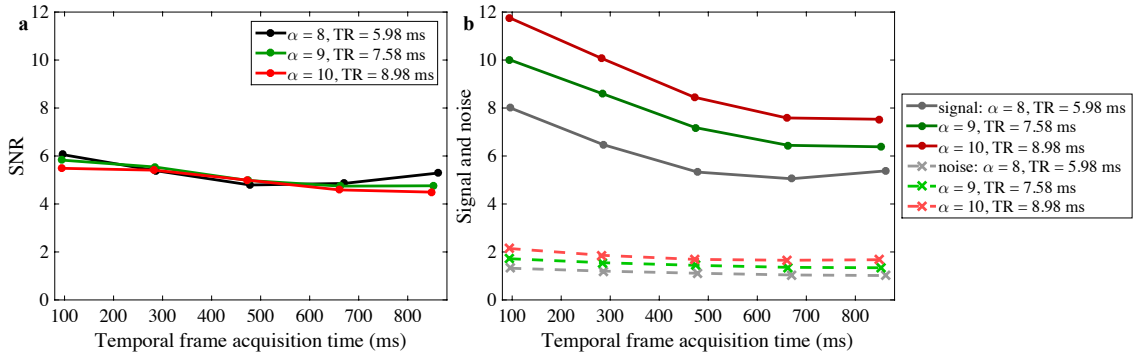


Figure 7.13: **a**: Mean SNR, **b**: signal and noise of the vascular signal across time frames for three acquisitions with readout parameters chosen to match signal attenuation.

matrix size of 128 x 128 x 128 and an image FOV of 150 x 150 x 150 mm. Scans were acquired in order of the level of undersampling. Scans with flip angle = 8° and TR = 5.98 (TE = 2.67 ms, bandwidth = 300 Hz/Px) had acquisition times of ≈ 4'59 s, ≈ 4'30 s and ≈ 4' for x40, x45 and x50 undersampling factors, respectively. Scans with flip angle = 9° and TR = 7.58 (TE = 3.44 ms, bandwidth = 202 Hz/Px) had acquisition times of ≈ 6'23 s, ≈ 5'44 s and ≈ 5'07 s.

In Figure 7.14 the axial MIP images for the first time frame of each acquisition are shown. The vascular signal is similar across all acquisitions, although extracranial arteries are in greater evidence in the more heavily undersampled scans. These scans were performed after the x40 undersampled acquisitions, so it is possible patient motion resulted in a shift in the labelling plane. This in turn would change the phase offsets at the external carotid arteries feeding these vessels and so change the labelling efficiency.

The Jaccard distances (Equation 6.3) between the PCASL images, calculated across all time frames, are shown in Figure 7.15.a. Images acquired with the same flip angle and TR are all similar; the Jaccard distances are very small. Figures 7.15.b and c show the results for the SNR calculations and the corresponding signal and noise values. As in Figure 7.13 the change in noise values over time, combined with the slower rate of signal attenuation, results in a low level of SNR attenuation over time. Upon inspection of the signal values, higher flip angles do have a higher starting signal. However, the relationship between the undersampling factor and signal levels is less clear from these acquisitions. A greater level

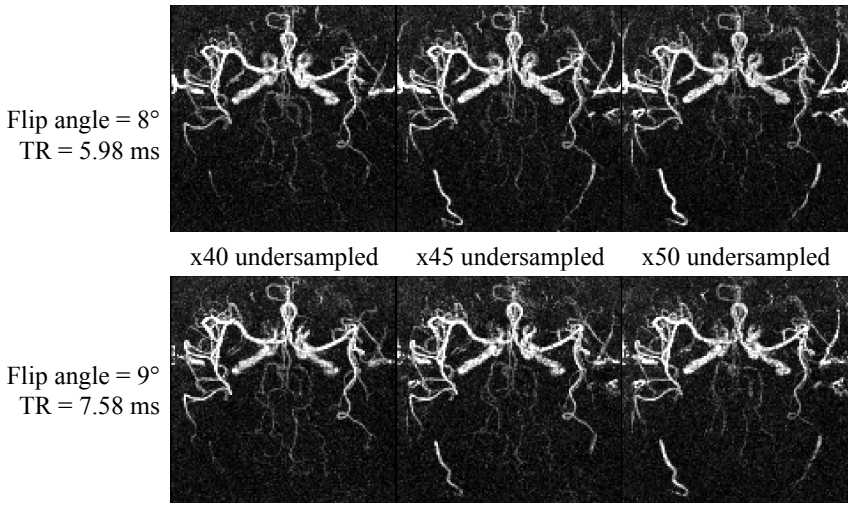


Figure 7.14: Axial MIP images for the first time frame of acquisitions with matched signal attenuation (rows) and varying undersampling factor (columns).

of signal for a higher undersampling factor could be due to the inclusion of more aliased signal, as there will be more artefact present with increased undersampling.

The differences between undersampling by a factor of 45 or 50 (versus a baseline undersampling of 40) for either flip angle are small, but the decrease in scan time for a factor of 50 versus 45 is about 30 seconds. For an 8 cycle VEPCASL acquisition this would result in a time saving of approximately two minutes. When compared to an undersampling factor of 40, the total scan time is reduced by four minutes. As the image quality for the two sets of scans is similar, future acquisitions make use of an 8° flip angle, in order to benefit from the faster scan time offered by the shorter TR. Similarly, the higher undersampling factors tested here allow decreases in the scan time without a visible change in image quality and are adopted in later scans.

7.4 Dynamic 3D VEPCASL subject scans

To assess the applicability of the optimised 3D radial angiography sequence to VEPCASL subject data were acquired for undersampling factors of 45 and 50, in an effort to reduce total scan times.

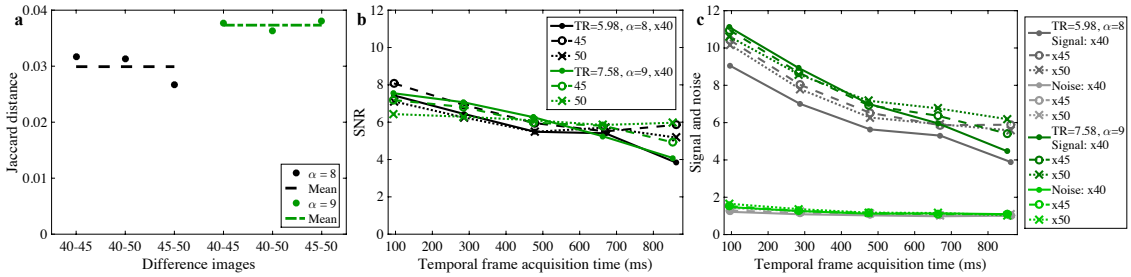


Figure 7.15: **a**: Jaccard distances between images with different undersampling factors for an 8° flip angle (black) and a 9° flip angle (green). **b**: Mean SNR, **c**: signal and noise of the vascular signal across time frames for subject scans with matched signal attenuation and a range of undersampling factors.

7.4.1 Methods

Acquisition protocol

Data for a healthy female subject (34 years) were acquired. A field map of the labelling plane (voxel size = 0.9 x 0.9 x 2.0 mm, TR = 200 ms, TE1 = 5.19 ms, TE2 = 6.19 ms, acquisition time = 1 minute) was acquired and a set of optimised encodings calculated for the four main brain-feeding arteries, including a correction for any phase offsets in the labelling plane (Chapter 5). Two VEPCASL scans were acquired, with undersampling factors of 45 (acquisition time $\approx$ 17'53 s) and 50 (acquisition time $\approx$ 16 minutes), flip angle = 8°, TR = 5.98 ms, temporal resolution = 191.36 ms, matrix size = 128 x 128 x 128 and image FOV = 150 x 150 x 150 mm. Labelling pulse train parameters as in Okell *et al.* [8] were used in conjunction with unipolar VEPCASL and a labelling duration of 800 ms.

Image analysis

VEPCASL images were analysed using a Bayesian maximum *a posteriori* (MAP) method [75], as used in Chapters 4 and 5, to separate out vessel specific information. SNR in the vessel-selective images was calculated similarly to Section 7.2. Vessel specific signal masks were created according to the dominant feeding artery of each voxel meeting the signal threshold (99^{th} percentile) in data averaged across acquisitions. These signal masks were also used to aid in generating images of the angiographic data that can give an idea of the vessel structure from all angles. Voxels containing signal above the designated threshold in each acquisition, as opposed to signal only common to both, were assigned a

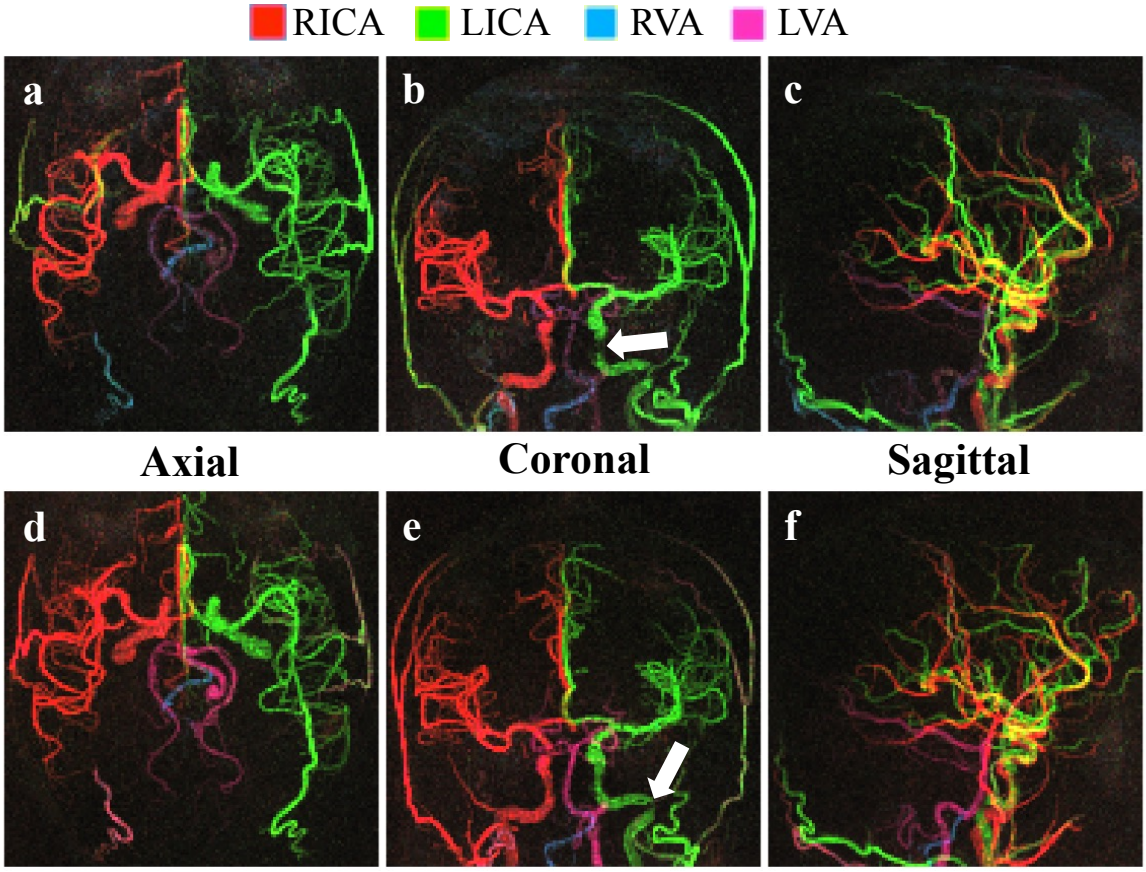


Figure 7.16: Time averaged vessel-selective MIP angiograms of the cerebral vasculature for undersampling factors of 45 (top row) and 50 (bottom row). Voxels are coloured according to the labelled feeding arteries (RICA/LICA = right/left internal carotid artery, RVA/LVA = right/left vertebral artery). White arrows indicate stretches of vascular signal dropout. NB: yellow colouring is a result of the image view point, where arteries containing blood from the RICA and LICA overlap. It is not a result of mixed blood supply.

single point in a 3D Matlab plot and colour coded according to the dominant feeding vessel (mixed signal is not shown).

7.4.2 Results

Dynamic vessel-selective images were acquired for both undersampling factors. Figure 7.16 shows time averaged MIP vessel-selective images for both undersampling factors, whilst Figure 7.17 displays the axial MIPs for each time frame. The vessel definition and assignment of vascular signal to the different feeding arteries by the MAP analysis is similar between the acquisitions. There are some small regions of vascular signal dropout

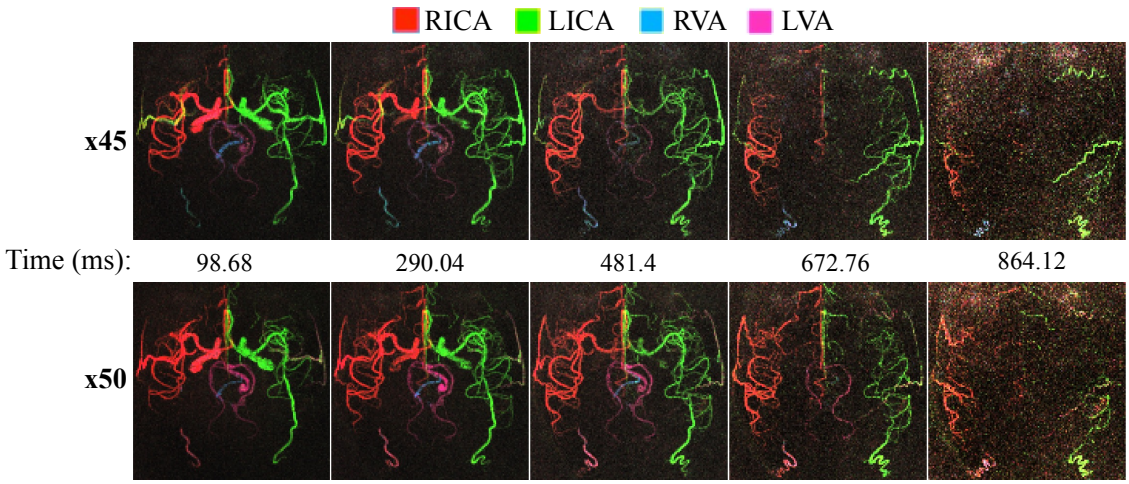


Figure 7.17: Vessel-selective axial MIP angiograms for each time frame of the undersampled acquisitions.

(white arrows, Figure 7.16.b and e) and signal in the extracranial arteries has been assigned to different feeding vessels. Notably signal in the right superficial temporal artery is attributed to the left internal carotid artery in the x45 undersampled acquisition, but to the right internal carotid in the x50 undersampled scan. Likewise, signal in the left superficial temporal artery has been assigned to the left internal carotid in the x45 undersampled images, but to the left vertebral artery in the x50 acquisition. The degree of signal mixing in the vertebral arteries in Figures 7.16.a and d, as denoted by the more or less purple colour, is different between the two acquisitions. The yellow colouring seen around arteries fed by the internal carotid arteries is not a result of mixed supply, it is due to the image viewpoint – where arteries fed by the carotids overlap but do not contain mixed supply. In Figure 7.17 the delayed arrival of labelled blood to more distal cerebral arteries and the extracranial arteries is evident in the later time frames, although the background noise is also increasingly apparent.

The precise allocation of signal to the labelled vessels is clearer in the time-resolved coronal MIP images for each vessel in Figures 7.18 and 7.19. The flow of blood over time through the vascular network into the peripheral arteries can clearly be seen for each feeding artery. However, in the analysis of both acquisitions some signal from the right internal carotid has been assigned to the right vertebral artery (red arrows).

The 3D vessel-selective images in Figure 7.20 only display information about the dominant feeding vessels in arteries for the first time frame. They confirm that the dominant feeding vessel for the posterior circulation appears to be the left vertebral artery. Regions of signal dropout seen in Figure 7.16 (white arrows) are circled in Figures 7.20.b and d and correspond to sections where less voxels met the signal threshold.

The SNR for the two VEPCASL acquisitions was calculated using two different noise sources. Firstly, noise measurements from ROIs in the vessel-selective angiograms generated by the MAP analysis and, secondly, from ROIs in the label/control all subtracted data. SNR calculations were averaged across vessels for each time frame and are shown in Figure 7.21.a. When the SNR is calculated using the noise ROIs from the MAP results the values for the more heavily undersampled acquisition are higher in earlier time frames. The SNR using noise from the label/control all subtraction images is similar between acquisitions and much flatter across time frames. From examination of the noise values in Figure 7.21.b, the noise across time frames in the MAP results is much lower and only decreases very gradually over time. The noise from the label/control all subtraction images follows the same pattern seen in earlier scans, with higher initial values. The MAP analysis has helped reduce noise in the resulting artery specific images, as compared to the values seen in the non-selective subtraction images.

7.4.3 Discussion

Time-resolved vessel-selective angiograms have been acquired in 3D by combining VEPCASL with an undersampled radial k-space trajectory. The 3D angiograms constructed here (Figure 7.20) offer a somewhat different view of the vasculature versus the MIP images (Figures 7.16 – 7.19).

The VEPCASL images acquired with different undersampling factors assign vascular signal to the labelled feeding arteries slightly differently. This is most evident in the different levels of signal mixing of the vertebral arteries in the axial MIP images (Figures 7.16.a and d) and the differing assignment of the source artery for signal in the superficial temporal

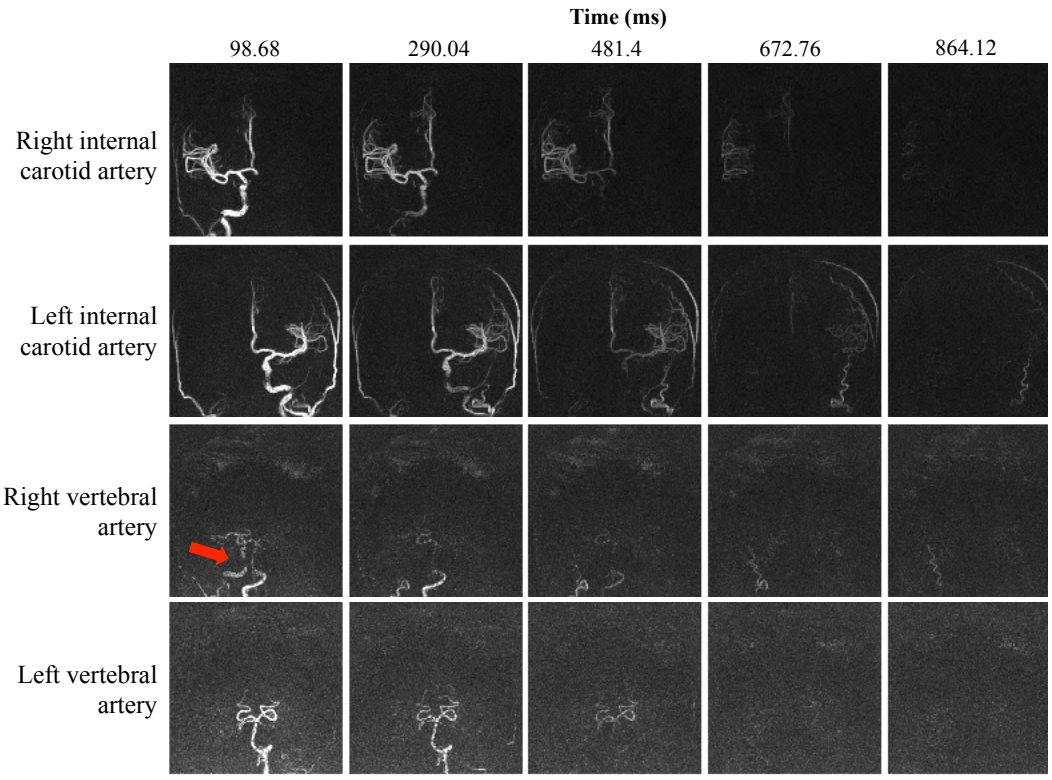


Figure 7.18: Vessel-selective coronal MIP images across time frames for an undersampling factor of 45. The red arrow indicates right internal carotid signal that has been assigned to the right vertebral artery.

arteries. These differences are likely due to shifts in the location of the labelling plane as a result of subject movement between the two VEPCASL scans. The labelling plane was not reassessed between the scans, so there is over 30 minutes between the start and end of the VEPCASL imaging.

Additionally, signal from the right internal carotid was misassigned to the right vertebral artery in the analysis of both VEPCASL scans (Figures 7.18 and 7.19, red arrows). This could be due to the presence of extracranial artery signal, which may have skewed the assignment of the vascular signal. Within the MAP analysis it is possible to choose the region of the images used to estimate labelling efficiencies achieved in different arteries, and so better calculate both the encoding matrix and whether the vessel locations in the labelling plane have shifted. In theory, if a region where there is little or no mixed artery signal is used, the calculation of the labelling efficiencies should be more robust and help prevent misassignment of vascular signal. However, when the analysis was re-performed

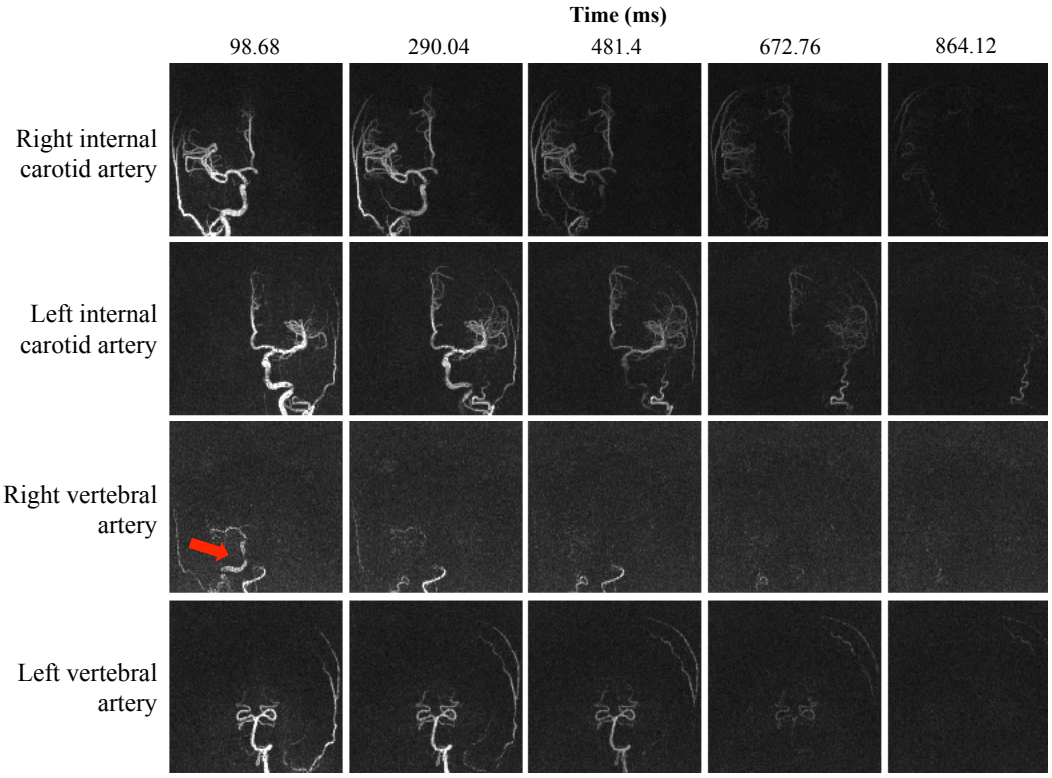


Figure 7.19: Vessel-selective coronal MIP images across time frames for an undersampling factor of 50. The red arrow indicates right internal carotid signal that has been assigned to the right vertebral artery.

here, using a reduced region of data to calculate the labelling efficiencies, the results remained as in Figures 7.16 – 7.21. One way in which these issues could be mitigated in future scans would be to identify the external carotid arteries in the labelling plane and so be able to assign extracranial artery signal to these as their true feeding vessels. Six vessels can be efficiently labelled using an 8 cycle encoding scheme based on a Hadamard matrix, so inclusion of the external carotid arteries would not necessitate an increase in scan time. The total acquisition times of the current scans still remains relatively long but, for an undersampling factor of 50, scan times of approximately 16 minutes for vessel-selective information on four vessels are achievable.

Another feature of note in the vessel-selective angiograms is signal dropout in certain vessel regions (white arrows, Figure 7.16). This loss in signal could be due to regions of turbulent flow and therefore mitigated by using flow compensation and/or a shorter TE. The higher SNR reported for the x50 undersampled scan in Figure 7.21, however, appears to be driven

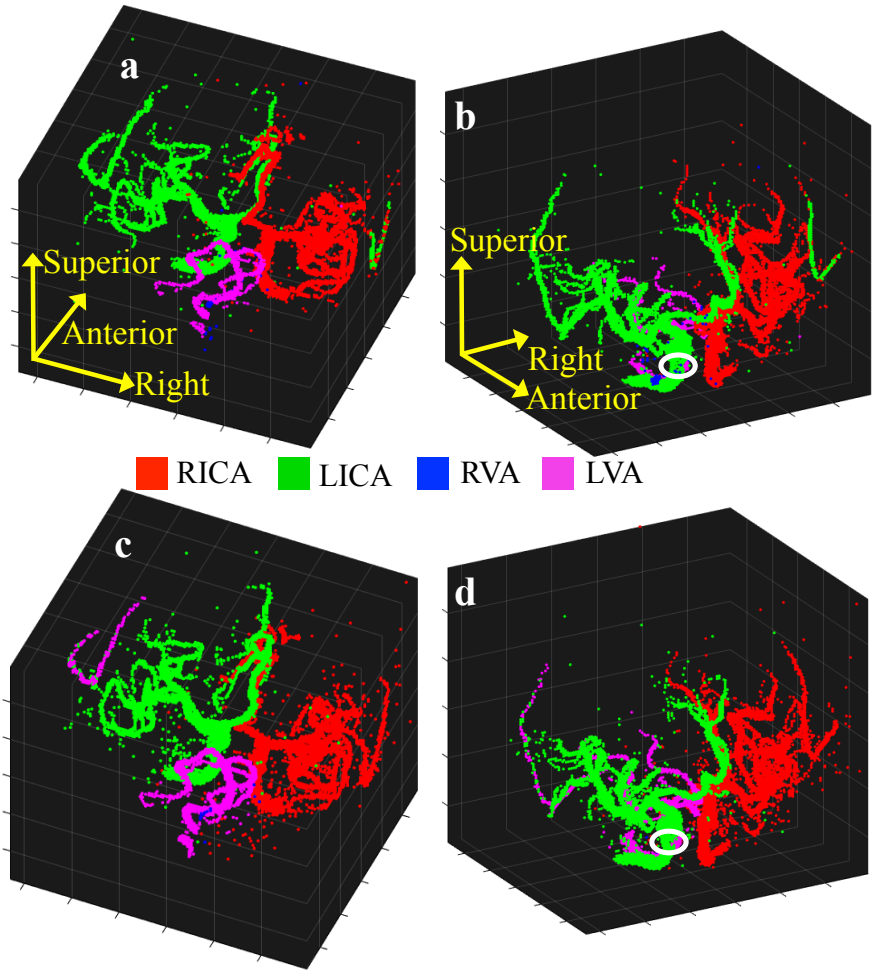


Figure 7.20: Signal thresholded, single time point, 3D vessel-selective angiograms from different viewpoints of the cerebral vasculature, for undersampling factors of 45 (top row) and 50 (bottom row). White circles indicate regions where vascular signal dropout is seen in Figure 7.16.

by the inclusion of aliasing artefact in the vascular signal. The MAP analysis has more successfully reduced the background noise than simple subtraction of the images. Consequently the resulting SNR for the x50 undersampled case is elevated, where we might have expected the SNR across acquisitions to have been similar, as in Figure 7.15.

7.5 General discussion

The optimisation process detailed in Section 7.3 enabled the development of the 3D, dynamic, vessel-selective sequence. However, there are certain combinations of parameters

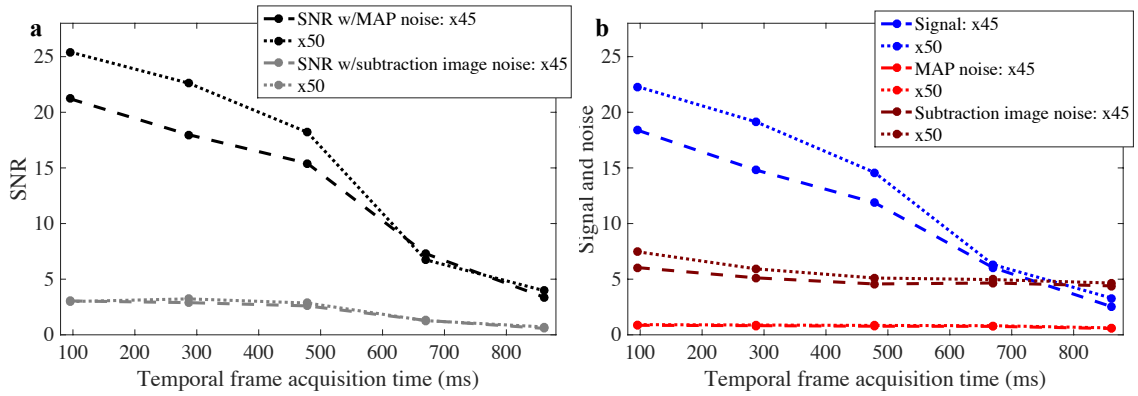


Figure 7.21: **a**: Mean SNR, **b**: signal and noise, over all arteries and across time frames, for two undersampling factors. MAP noise refers to noise taken from ROIs in vessel-selective images generated by the MAP analysis. Subtraction noise refers to noise taken from label/control all subtraction images.

that could benefit from further investigation. For example, a longer TR was initially chosen to deal with rapid signal attenuation across time frames (Figure 7.8). In later steps of the optimisation process no major gains were found, in terms of vessel definition, by using a larger flip angle for scans with an acceptable level of signal attenuation over time (Figure 7.12). Consequently, it might be possible to use a smaller flip angle, and so a shorter TR, to further reduce the scan time without compromising image quality. The effect of the increased bandwidth, and so inclusion of more noise, this would necessitate would need to be established.

The method used to assess the SNR in angiograms here is not infallible. It inherently includes aliased signal present in the images. However, across scans these calculations show elevated noise signal in earlier time frames. It thus appears that streak artefacts, whose magnitude is larger when the signal in the images is stronger, predominantly drive the noise values. If this is the case then the reconstruction strategy used here would benefit from the inclusion of a technique such as compressed sensing. Compressed sensing has already been combined with angiography [130] and its combination with other acceleration methods, such as undersampling, has in general been shown to improve angiographic image quality [85]. When acquiring angiograms compressed sensing can take advantage of their sparsity in the image and temporal frequency domains. In order to use compressed sensing the aliasing artefacts in the image must be incoherent – or noise like – as in undersampled

radial acquisitions [131]. Compressed sensing has the potential to help reduce noise in the final reconstructed images and also allow reconstruction of high quality angiograms from further undersampled data.

Three-dimensional time-resolved VEPCASL angiograms, labelling four arteries, were acquired here in approximately 16 minutes. A PCASL based method for selecting single arteries in the labelling plane [62] has recently been combined with a keyhole acquisition to generate 3D time-resolved vessel-selective angiograms [97]. The acquisition of data for each labelled artery took approximately 5 minutes, so they were only able to acquire information on three vessels in 15 minutes. As discussed in Chapter 2, VEPCASL is inherently more time and SNR-efficient than single-artery selective methods. Other 3D angiography studies that have combined a PCASL labelling scheme with radial trajectories [39, 95] have achieved a higher spatial resolution. As stated in Section 7.3, a certain amount of spatial resolution was sacrificed here in order to reduce acquisition times. Increased spatial resolution would require increased scan times if the same image quality is to be maintained with the current sequence.

As compared to the 2D dynamic VEPCASL angiograms acquired in Chapter 6, the angiograms seen in this chapter offer a much more comprehensive view of the entire cerebral vasculature. In terms of image analysis, the 3D images contain many more voxels fed by each artery, which are used to better inform the MAP analysis. The 3D angiograms provide a compliment to the accelerated 2D images. They would be suitable in cases where a more detailed examination of the vascular tree is required and where the ability to view vessels from all directions is of benefit. For example, arteriovenous malformations have been successfully viewed in 3D PCASL angiograms [95] and the usefulness of 3D angiograms in the diagnosis and treatment of cerebrovascular disease, in particular cerebral aneurysms, has been expounded [9, 10]. In these last two studies x-ray DSA was used to generate 3D images. In particular for x-ray DSA, a range of reconstruction techniques is commonly available, such as MIP images and volume and surface rendering techniques [9, 10]. An extension of this work would be to consider the use of volume and surface rendering methods for VEPCASL angiograms to improve vessel visualisation. The alternative images to

the MIPs in Figure 7.20 are relatively crude and only designed to give basic information on the success of the imaging strategy.

Further assessment of the vessel-selective 3D angiograms would involve acquisition of data from a greater number of healthy subjects and an additional optimisation process to reduce acquisition times. A scan time of 16 minutes is prohibitively long in many settings, but there are a number of options that could be incorporated here to reduce scan duration. As mentioned above, the inclusion of compressed sensing in the reconstruction could help to mitigate the effects of increasing the undersampling factor. Additionally, the temporal resolution of the scheme could be reduced or fewer encodings could be acquired. Artery specific information for four vessels can still be extracted from a six cycle encoding scheme, although the SNR efficiency is somewhat reduced. Moreover, the inclusion of individual coil information could be used to better condition the reconstruction and therefore facilitate higher undersampling factors.

The technique as described above could be applied to alternative labelling planes higher up in the brain, to assess the vascular network fed by the cerebral arteries above the circle of Willis for example. However, this would require a greatly increased number of encodings, potentially up to 24 (Section 5.2.4). The scan times would then be in excess of 45 minutes. In order to be able to acquire angiograms in a sensible time frame, whilst labelling more than four vessels, the 3D acquisition here needs to be further accelerated.

7.6 Conclusions

The 3D time-resolved VEPCASL angiograms acquired here allow vessel specific, dynamic 3D information to be acquired non-invasively. These angiograms have the potential to contribute to research, diagnosis and treatment of cerebrovascular disease. However, a reduction in acquisition times would make this method useful in a greater variety of settings, and enable further information on the vasculature to be gleaned by labelling more than four vessels.

Chapter 8

Summary and future work

The work in this thesis aimed to optimise perfusion imaging and angiography for use in the treatment and diagnosis of cerebrovascular disease. This was done, firstly, through the development of optimised encoding schemes for vessel-encoded pseudocontinuous arterial spin labelling (VEPCASL), and PCASL, that are automated, applicable to any number of arteries and able to correct for B_0 inhomogeneities in the labelling plane. Following on from optimising the encodings, work was done on the development of fast two-dimensional (2D) and optimised three-dimensional (3D) dynamic VEPCASL angiography.

8.1 Summary of results

8.1.1 Optimisation of VEPCASL encoding

An automated method for calculating optimised encodings for any number of vessels has been developed (Chapter 4) and extended to incorporate a correction for off-resonance in the labelling plane (Chapter 5), which is also applicable to PCASL scans. The technique was shown to work well in both simulations and phantom scans for any number or arrangement of arteries in the labelling plane. Healthy subject scans confirmed the optimised encoding scheme works well for four vessels, both without the inclusion of phase offset corrections, when the labelling plane is relatively homogeneous, and for cases where off-resonances are present. Optimised encodings were able to efficiently label arteries in

non-typical vessel arrangements (Figure 4.7) and to recover perfusion signal that would otherwise have been lost due to inefficient labelling caused by inhomogeneities in the labelling plane (Figures 5.7 and 5.8). The ability to correct for phase offsets at artery locations in the labelling plane could be particularly useful for PCASL at higher field strengths, where B_0 homogeneity is more difficult to establish.

The optimisation of encodings to label more than four vessels in labelling planes above the circle of Willis has been more difficult to assess *in vivo*. The method as it stands offers a way of calculating a minimal number of encodings necessary to efficiently label any number of arteries, and has been shown to work well in simulations and phantom scans. As such it has the potential to be of particular use in scenarios where acquisition time is at a premium. However, the results of perfusion imaging in healthy subjects for more than four vessels have been somewhat variable, affected by the given vessel geometry and the labelling of arteries outside the brain.

8.1.2 Development of dynamic vessel-selective angiography

Both a fast 2D radial (Chapter 6) and an optimised 3D radial (Chapter 7) readout have been developed for the acquisition of time-resolved vessel-selective angiograms. The two methods are to a certain extent complementary – providing information useful in different scenarios. Additionally, these two chapters make use of the optimised encodings developed in Chapter 5.

Vessel-selective, 2D time-resolved angiograms were acquired in approximately one minute. A radial readout scheme was found to provide both better vessel definition (Figure 6.10) and significantly higher signal-to-noise ratio (SNR) than a time-matched Cartesian readout (Figure 6.11). Initial optimisation of the readout scheme demonstrated that angiograms acquired in this time frame benefited from the increased SNR efficiency of a balanced steady-state free precession (bSSFP) readout (Figure 6.6), without which identification of the peripheral vessels and posterior circulation was difficult. However, the angiograms acquired in healthy subjects had a tendency to suffer from central artefacts that affected

vessel definition at the centre of the brain, these were assumed to be a result of pulsatile motion around the brain stem. Consequently, to make the acquisition strategy more robust, further assessment of the best regions in the brain to benefit from this kind of fast imaging is needed.

The combination of VEPCASL with a 3D radial readout has produced vessel-selective time-resolved angiograms of a high quality (Figures 7.18 and 7.19), similar to combinations of non-selective PCASL and 3D radial acquisitions seen before [39, 40, 95], although with a reduced level of spatial resolution that was chosen to decrease scan times. Additionally, in a comparable time frame to a 3D PCASL based vessel-selective method providing information on three vessels [97], information on four arteries in the labelling plane was acquired. The acquisitions only considered the four main brain-feeding arteries in the neck – the right and left internal carotid and vertebral arteries. However, on inspection of the resulting angiograms, signal from the extracranial arteries is clearly in evidence and a refinement of the current technique would be their inclusion in the encoding scheme. An eight-cycle scheme is currently used to acquire information about four vessels in the most SNR-efficient way. It is possible to extend an eight-cycle scheme, however, to label six vessels without compromising SNR efficiency; the columns of a Hadamard matrix will always provide an SNR optimal encoding matrix [30]. Although bSSFP has been used to acquire 3D angiograms [39], optimisation of the 3D radial scheme here, for use with VEPCASL, found a spoiled gradient echo readout to provide more robust vessel information over the longer scan times and less homogeneous magnetic field required by the 3D acquisition (Figure 7.5).

High undersampling factors were tested in the optimisation of the 3D protocol and were not found to affect the quality of angiograms. However, of particular interest was the finding that noise levels in the 3D angiograms were strongly driven by the presence of aliasing artefacts. In general, the higher the undersampling factor, the higher the noise levels. As a result the extraction of any quantitative results from the data would be improved by reconstruction methods that help to reduce aliasing artefacts, such as compressed sensing [85].

8.2 Future work

The work described in this thesis can be loosely divided into optimisation of the encoding process and development of radial imaging techniques for VEPCASL angiography. There are a number of directions that could further develop these techniques and validate their usefulness in a range of scenarios.

The optimised encoding scheme and accompanying correction for off-resonance developed across Chapters 4 and 5 could benefit from further inclusion of the true encoding functions. At the moment the choice of optimised encodings implicitly assumes they are sinusoidal. A more accurate representation would be to choose optimised encoding functions from a set based on simulations of the real encodings. Additionally, in order to improve the robustness of encoding more than four vessels, an adaptation of the ideal encoding scheme, which initialises the calculation of the optimised encodings, to better consider the pattern of the arteries to be labelled could be developed. This would follow on from the alternate Hadamard matrices considered in Chapter 5.

It is difficult to find a labelling plane above the circle of Willis where the arteries of interest are all (approximately) perpendicular to the labelling plane. A further extension of this work would be to develop a more sophisticated way of choosing the labelling plane, potentially through an automated vessel segmentation protocol that selects arteries, and so the best labelling plane, to target from time-of-flight data. The vessel anatomy could also be incorporated into the calculation of the encodings, so functions can be chosen that help to mitigate artery tortuosity in the labelling plane and maximise the efficiency of the encodings. The inclusion of all arteries in the labelling plane, both the cerebral and extracranial arteries, could also help to better condition the encodings and avoid contamination from arteries that are inadvertently labelled.

Although some 2D angiograms were acquired above the circle of Willis in Chapter 5 (Figure 5.11), the next stage of this work would be to combine the optimised encoding scheme for more than four vessels with the best possible angiographic readout. It would then be possible to acquire high quality images of the vascular network stemming from the cerebral

arteries. In order to make this possible in 3D, which would offer the greatest detail for disease diagnosis and treatment planning, the 3D acquisition times need to be reduced. This would allow labelling of greater numbers of arteries in reasonable scan times. As discussed in Chapter 7, there are a number of options to do this, such as increasing the acceleration factor, incorporating compressed sensing into the reconstruction and adjusting parameters such as the repetition time and temporal resolution to further accelerate acquisition.

Alongside acquiring 3D angiograms for an increased number of vessels, the utility of the angiograms in situations such as surgical planning could be increased by the use of a different type of image reconstruction. Volume rendering has been used with 3D vessel-selective x-ray digital subtraction angiography (DSA) to produce detailed angiograms used in surgical planning and assessment [10]. The incorporation of a reconstruction of this type into VEPCASL angiography could improve the information they provide clinicians.

The subject data acquired for this thesis has all involved healthy subjects. In order to validate the clinical applicability of this work the next step would be to trial the techniques in patient populations. This validation step would also benefit from comparison of the VEPCASL based methods proposed here with already existing techniques, such as CT perfusion imaging and vessel-selective x-ray DSA angiograms.

The optimised encoding schemes, including corrections for off-resonance in the labelling plane, could provide more robust PCASL and VEPCASL perfusion images for subjects with non-regular vessel arrangements in the neck and where information on more than four feeding vessels is of interest. VEPCASL angiography has previously required lengthy scan times [8, 100], not always viable in a clinical setting. The inclusion into a patient protocol of the optimised 2D radial acquisition described in Chapter 6, however, would only require approximately three minutes (if a field map is also acquired). This would provide information on both the cerebral vasculature of the whole brain above the circle of Willis and on the artery in the neck feeding each part of the vascular tree. The acquisition of 3D VEPCASL angiograms in patient populations would give a true idea of how much more detail they could provide for diagnosis and treatment planning. Cerebrovascular diseases such as arteriovenous malformations and other lesions in the brain could benefit particularly

from this type of imaging. The vessels that feed, and then form them, can be extremely convoluted, so understanding their exact size, shape and source of blood supply would benefit greatly from 3D vessel specific images.

Bibliography

[1] W. J. Powers, "Cerebral hemodynamics in ischemic cerebrovascular disease," *Annals of Neurology*, vol. 29, pp. 231–240, 1991.

[2] D. S. Liebeskind, "Collateral circulation," *Stroke*, vol. 34, no. 9, pp. 2279–84, 2003.

[3] D. Setyowati and K. Jeyaseelan, "Stroke," 2014.

[4] P. Mergenthaler, U. Dirnagl, and A. Kunz, *Ischemic Stroke: Basic Pathophysiology and Clinical Implication*, book section 97, pp. 2543–2563. Springer New York, 2013.

[5] R. Khan, K. Nael, and W. Erly, "Acute stroke imaging: what clinicians need to know," *Am J Med*, vol. 126, no. 5, pp. 379–86, 2013.

[6] G. W. Albers, "Impact of recanalization, reperfusion, and collateral flow on clinical efficacy," *Stroke*, vol. 44, no. 6 Suppl 1, pp. S11–2, 2013.

[7] M. Castillo and H. Alvarez, "Acute stroke: basic concepts and use of imaging for clinicians," *JBR-BTR*, vol. 96, pp. 3–9, 2013.

[8] T. W. Okell, M. A. Chappell, M. W. Woolrich, M. Gunther, D. A. Feinberg, and P. Jezzard, "Vessel-encoded dynamic magnetic resonance angiography using arterial spin labeling," *Magn Reson Med*, vol. 64, no. 3, pp. 698–706, 2010.

[9] T. Abe, M. Hirohata, N. Tanaka, Y. Uchiyama, K. Kojima, K. Fujimoto, A. M. Norbash, and N. Hayabuchi, "Clinical benefits of rotational 3D angiography in endovascular treatment of ruptured cerebral aneurysm," *American Journal of Neuroradiology*, vol. 23, no. 4, pp. 686–688, 2002.

[10] A. Jalali, V. M. Srinivasan, P. Chinnadurai, P. Kan, A. Arthur, and E. A. Duckworth, "Two-color 3D-3D fusion of selective rotational cerebral angiograms: a novel approach to imaging in cerebrovascular neurosurgery," *J Neurointerv Surg*, 2015.

[11] M. van Vliet, C. F. van Dijke, P. A. Wielopolski, T. L. M. ten Hagen, J. F. Veenland, A. Preda, A. J. Loeve, A. M. M. Eggermont, and G. P. Krestin, "MR angiography of tumor-related vasculature: From the clinic to the micro-environment," *RadioGraphics*, vol. 25, no. suppl1, pp. S85–S97, 2005.

[12] M. R. Jaff, B. L. Mintz, and J. Mintz, *Atlas of Clinical Vascular Medicine*. John Wiley & Sons, 2013.

[13] P. H. Kuo, E. Kanal, A. K. Abu-Alfa, and S. E. Cowper, "Gadolinium-based MR contrast agents and nephrogenic systemic fibrosis," *Radiology*, vol. 242, pp. 647–649, 2007.

[14] M. Bendszus, M. Koltzenburg, R. Burger, M. Warmuth-Metz, E. Hofmann, and L. Solymosi, "Silent embolism in diagnostic cerebral angiography and neurointerventional procedures: a prospective study," *The Lancet*, vol. 354, no. 9190, pp. 1594–1597, 1999.

[15] R. E. Latchaw, M. J. Alberts, M. H. Lev, J. J. Connors, R. E. Harbaugh, R. T. Higashida, R. Hobson, C. S. Kidwell, W. J. Koroshetz, V. Mathews, P. Villablanca, S. Warach, and B. Walters, "Recommendations for imaging of acute ischemic stroke: a scientific statement from the american heart association," *Stroke*, vol. 40, no. 11, pp. 3646–78, 2009.

[16] D. C. Alsop, J. A. Detre, X. Golay, M. Gunther, J. Hendrikse, L. Hernandez-Garcia, H. Lu, B. J. Macintosh, L. M. Parkes, M. Smits, M. J. van Osch, D. J. Wang, E. C. Wong, and G. Zaharchuk, "Recommended implementation of arterial spin-labeled perfusion MRI for clinical applications: A consensus of the ISMRM perfusion study group and the european consortium for ASL in dementia," *Magn Reson Med*, 2014.

[17] H. Jahanian, D. C. Noll, and L. Hernandez-Garcia, "B_0 field inhomogeneity considerations in pseudo-continuous arterial spin labeling (pCASL): effects on tagging efficiency and correction strategy," *NMR Biomed*, vol. 24, no. 10, pp. 1202–9, 2011.

[18] M. A. Bernstein, K. F. King, and X. J. Zhou, *Imaging gradients*, book section 8, pp. 243–273. Elsevier Academic Press, 2004.

[19] F. Bloch, "Nuclear induction," *Physical Review*, vol. 70, pp. 460–474, 1946.

[20] R. A. de Graaf, *In Vivo NMR Spectroscopy - 2nd Edition Principles and Techniques*. John Wiley & Sons, Ltd, 2007.

[21] E. M. Haacke, R. W. Brown, M. R. Thompson, and R. Venkatesan, *Magnetic Resonance Imaging: Physical Principles and Sequence Design*, book section 2, pp. 17–34. John Wiley & Sons, Inc., 1999.

[22] A. Webb, *Magnetic resonance imaging*, book section 4, pp. 157–219. Wiley, 2002.

[23] M. Gunther, "Perfusion imaging," *J Magn Reson Imaging*, vol. 40, no. 2, pp. 269–79, 2014.

[24] R. B. Buxton, L. R. Frank, E. C. Wong, B. Siewert, S. Warach, and R. R. Edelman, "A general kinetic model for quantitative perfusion imaging with arterial spin labeling," *Magn Reson Med*, vol. 40, pp. 383–396, 1998.

[25] S. D. Wolff and R. S. Balaban, "Magnetization transfer contrast (MTC) and tissue water proton relaxation in vivo," *Magn Reson Med*, vol. 10, no. 1, pp. 135–144, 1989.

[26] E. T. Petersen, I. Zimine, Y. C. Ho, and X. Golay, "Non-invasive measurement of perfusion: a critical review of arterial spin labelling techniques," *Br J Radiol*, vol. 79, no. 944, pp. 688–701, 2006.

[27] W. C. Wu, M. Fernandez-Seara, J. A. Detre, F. W. Wehrli, and J. Wang, "A theoretical and experimental investigation of the tagging efficiency of pseudocontinuous arterial spin labeling," *Magn Reson Med*, vol. 58, no. 5, pp. 1020–7, 2007.

[28] D. C. Alsop and J. A. Detre, "Multisection cerebral blood flow MR imaging with continuous arterial spin labeling," *Radiology*, vol. 208, no. 2, pp. 410–416, 1998.

[29] W. Y. Dai, D. Garcia, C. de Bazelaire, and D. C. Alsop, "Continuous flow-driven inversion for arterial spin labeling using pulsed radio frequency and gradient fields," *Magn Reson Med*, vol. 60, no. 6, pp. 1488–1497, 2008.

[30] E. C. Wong, "Vessel-encoded arterial spin-labeling using pseudocontinuous tagging," *Magn Reson Med*, vol. 58, no. 6, pp. 1086–1091, 2007.

[31] W. C. Wu, S. F. Jiang, S. C. Yang, and S. H. Lien, "Pseudocontinuous arterial spin labeling perfusion magnetic resonance imaging–a normative study of reproducibility in the human brain," *Neuroimage*, vol. 56, no. 3, pp. 1244–50, 2011.

[32] D. M. Garcia, C. de Bazelaire, and D. Alsop, "Pseudo-continuous flow driven adiabatic inversion for arterial spin labeling," in *Proceedings of the 13th Annual Meeting of ISMRM*, vol. 13, 2005.

[33] E. C. Wong and J. Guo, "Blind detection of vascular sources and territories using random vessel encoded arterial spin labeling," *MAGMA*, vol. 25, no. 2, pp. 95–101, 2012.

[34] M. Vidorreta, E. Balteau, Z. Wang, E. De Vita, M. A. Pastor, D. L. Thomas, J. A. Detre, and M. A. Fernandez-Seara, "Evaluation of segmented 3D acquisition schemes for whole-brain high-resolution arterial spin labeling at 3 T," *NMR Biomed*, vol. 27, no. 11, pp. 1387–96, 2014.

[35] M. A. Bernstein, K. F. King, and X. J. Zhou, *Echo train pulse sequences*, book section 16, pp. 702–801. Elsevier Academic Press, 2004.

[36] M. Vidorreta, Z. Wang, I. Rodriguez, M. A. Pastor, J. A. Detre, and M. A. Fernandez-Seara, "Comparison of 2D and 3D single-shot ASL perfusion fMRI sequences," *Neuroimage*, vol. 66, pp. 662–71, 2013.

[37] T. W. Okell, M. A. Chappell, M. E. Kelly, and P. Jezzard, "Cerebral blood flow quantification using vessel-encoded arterial spin labeling," *J Cereb Blood Flow Metab*, vol. 33, no. 11, pp. 1716–24, 2013.

[38] L. Yan, N. Salamon, and D. J. Wang, "Time-resolved noncontrast enhanced 4-D dynamic magnetic resonance angiography using multibolus TrueFISP-based spin tagging with alternating radiofrequency (TrueSTAR)," *Magn Reson Med*, vol. 71, no. 2, pp. 551–60, 2014.

[39] I. Koktzoglou, J. R. Meyer, W. J. Ankenbrandt, S. Giri, D. Piccini, M. O. Zenge, O. Flanagan, T. Desai, N. Gupta, and R. R. Edelman, "Nonenhanced arterial spin labeled carotid MR angiography using three-dimensional radial balanced steady-state free precession imaging," *J Magn Reson Imaging*, vol. 41, no. 4, pp. 1150–6, 2015.

[40] H. Wu, W. F. Block, P. A. Turski, C. A. Mistretta, and K. M. Johnson, "Noncontrast-enhanced three-dimensional (3D) intracranial MR angiography using pseudocontinuous arterial spin labeling and accelerated 3D radial acquisition," *Magn Reson Med*, vol. 69, no. 3, pp. 708–15, 2013.

[41] M. A. Bernstein, K. F. King, and X. J. Zhou, *Basic pulse sequences*, book section 14, pp. 579–647. Elsevier Academic Press, 2004.

[42] E. M. Haacke, R. W. Brown, M. R. Thompson, and R. Venkatesan, *Magnetic Resonance Imaging: Physical Principles and Sequence Design*, book section 18, pp. 451–512. John Wiley & Sons, Inc., 1999.

[43] K. Scheffler and S. Lehnhardt, "Principles and applications of balanced SSFP techniques," *Eur Radiol*, vol. 13, no. 11, pp. 2409–18, 2003.

[44] J. Hennig, O. Speck, and K. Scheffler, "Optimization of signal behavior in the transition to driven equilibrium in steady-state free precession sequences," *Magn Reson Med*, vol. 48, no. 5, pp. 801–9, 2002.

[45] P. Schmitt, P. Speier, X. Bi, P. Weale, and E. Mueller, "Non-contrast-enhanced 4D intracranial MR angiography: Optimizations using a variable flip angle approach," in *Proceedings of the 18th Annual Meeting of ISMRM*, p. 402, 2010.

[46] G. H. Glover and J. M. Pauly, "Projection reconstruction techniques for reduction of motion effects in mri," *Magn Reson Med*, vol. 28, no. 2, pp. 275–289, 1992.

[47] D. G. Nishimura, J. I. Jackson, and J. M. Pauly, "On the nature and reduction of the displacement artifact in flow images," *Magn Reson Med*, vol. 22, no. 2, pp. 481–492, 1991.

[48] M. A. Bernstein, K. F. King, and X. J. Zhou, *Advanced pulse sequence techniques*, book section 17, pp. 802–954. Elsevier Academic Press, 2004.

[49] M. A. Bernstein, K. F. King, and X. J. Zhou, *Common image reconstruction techniques*, book section 13, pp. 491–571. Elsevier Academic Press, 2004.

[50] M. Blaimer, F. Breuer, M. Mueller, R. M. Heidemann, M. A. Griswold, and P. M. Jakob, "SMASH, SENSE, PILS, GRAPPA. how to choose the optimal method," *Top Magn Reson Imaging*, vol. 15, pp. 223–236, 2004.

[51] M. A. Bernstein, K. F. King, and X. J. Zhou, *Signal acquisition and k-space sampling*, book section 11, pp. 367–442. Elsevier Academic Press, 2004.

[52] M. A. Griswold, R. M. Heidemann, and P. M. Jakob, "Direct parallel imaging reconstruction of radially sampled data using GRAPPA with relative shifts," in *Proceedings of the 11th Annual Meeting of ISMRM*, p. 2349, 2003.

[53] C. A. Mistretta, "Undersampled radial MR acquisition and highly constrained back projection (HYPR) reconstruction: potential medical imaging applications in the post-Nyquist era," *J Magn Reson Imaging*, vol. 29, no. 3, pp. 501–16, 2009.

[54] D. C. Peters, F. R. Korosec, T. M. Grist, W. F. Block, J. E. Holden, K. K. Vigen, and C. A. Mistretta, "Undersampled projection reconstruction applied to MR angiography," *Magn Reson Med*, vol. 43, pp. 91–101, 2000.

[55] C. A. Mistretta, O. Wieben, J. Velikina, W. Block, J. Perry, Y. Wu, K. Johnson, and Y. Wu, "Highly constrained backprojection for time-resolved MRI," *Magn Reson Med*, vol. 55, pp. 30–40, 2006.

[56] J. Song, Y. Liu, S. L. Gewalt, G. Cofer, G. A. Johnson, and Q. H. Liu, "Least-square NUFFT methods applied to 2-D and 3-D radially encoded MR image reconstruction," *IEEE Transactions on Biomedical Engineering*, vol. 56, no. 4, pp. 1134–1142, 2009.

[57] J. A. Fessler and B. P. Sutton, "Nonuniform fast Fourier transforms using min-max interpolation," *IEEE Transactions on Signal Processing*, vol. 51, no. 2, pp. 560–574, 2003.

[58] M. Wintermark, M. Sesay, E. Barbier, K. Borbely, W. P. Dillon, J. D. Eastwood, T. C. Glenn, C. B. Grandin, S. Pedraza, J. F. Soustiel, T. Nariai, G. Zaharchuk, J. M. Caille, V. Dousset, and H. Yonas, "Comparative overview of brain perfusion imaging techniques," *Stroke*, vol. 36, no. 9, pp. e83–99, 2005.

[59] W. Dai, P. M. Robson, A. Shankaranarayanan, and D. C. Alsop, "Modified pulsed continuous arterial spin labeling for labeling of a single artery," *Magn Reson Med*, vol. 64, no. 4, pp. 975–982, 2010.

[60] N. P. Davies and P. Jezzard, "Selective arterial spin labeling (SASL): perfusion territory mapping of selected feeding arteries tagged using two-dimensional radiofrequency pulses," *Magn Reson Med*, vol. 49, no. 6, pp. 1133–42, 2003.

[61] M. Gunther, "Efficient visualization of vascular territories in the human brain by cycled arterial spin labeling MRI," *Magn Reson Med*, vol. 56, no. 3, pp. 671–5, 2006.

[62] M. Helle, D. G. Norris, S. Rufer, K. Alfke, O. Jansen, and M. J. van Osch, "Superselective pseudocontinuous arterial spin labeling," *Magn Reson Med*, vol. 64, no. 3, pp. 777–86, 2010.

[63] J. Hendrikse, J. van der Grond, H. Lu, P. C. M. van Zijl, and X. Golay, "Flow territory mapping of the cerebral arteries with regional perfusion MRI," *Stroke*, vol. 35, no. 4, pp. 882–887, 2004.

[64] R. Werner, D. G. Norris, K. Alfke, H. M. Mehdorn, and O. Jansen, "Continuous artery-selective spin labeling (CASSL)," *Magn Reson Med*, vol. 53, no. 5, pp. 1006–12, 2005.

[65] I. Zimine, E. T. Petersen, and X. Golay, "Dual vessel arterial spin labeling scheme for regional perfusion imaging," *Magn Reson Med*, vol. 56, no. 5, pp. 1140–1144, 2006.

[66] R. R. Edelman, B. Siewert, D. G. Darby, V. Thangaraj, A. C. Nobre, M. M. Mesulam, and S. Warach, "Qualitative mapping of cerebral blood flow and functional localization with echo-planar MR imaging and signal targeting with alternating radio frequency," *Radiology*, vol. 192, no. 2, pp. 513–520, 1994.

[67] R. R. Edelman and Q. Chen, "EPISTAR MRI: multislice mapping of cerebral blood flow," *Magnetic resonance in medicine*, vol. 40, no. 6, pp. 800–805, 1998.

[68] S. Kim, "Quantification of relative cerebral blood flow change by flowsensitive alternating inversion recovery (FAIR) technique: Application to functional mapping," *Magn Reson Med*, vol. 34, no. 3, pp. 293–301, 1995.

[69] K. K. Kwong, D. A. Chesler, R. M. Weisskoff, K. M. Donahue, T. L. Davis, L. Ostergaard, T. A. Campbell, and B. R. Rosen, "MR perfusion studies with T_1-weighted echo planar imaging," *Magn Reson Med*, vol. 34, no. 6, pp. 878–887, 1995.

[70] E. C. Wong, R. B. Buxton, and L. R. Frank, "Quantitative imaging of perfusion using a single subtraction (QUIPSS and QUIPSS II)," *Magn Reson Med*, vol. 39, no. 5, pp. 702–8, 1998.

[71] J. D. Eastwood, C. A. Holder, P. A. Hudgins, and A. W. Song, "Magnetic resonance imaging with lateralized arterial spin labeling," *Magn Reson Imaging*, vol. 20, pp. 583–586, 2002.

[72] J. Guo and E. C. Wong, "Optimization of the encoding scheme for improved snr efficiency in vessel encoded pseudo-continuous ASL," in *Proceedings of the 17th Annual Meeting of ISMRM*, p. 1522, 2009.

[73] S. Gevers, R. P. Bokkers, J. Hendrikse, C. B. Majoie, D. A. Kies, W. M. Teeuwisse, A. J. Nederveen, and M. J. van Osch, "Robustness and reproducibility of flow territories defined by planning-free vessel-encoded pseudocontinuous arterial spin-labeling," *AJNR Am J Neurorad*, vol. 33, pp. E21–E25, 2012.

[74] M. A. Chappell, T. W. Okell, P. Jezzard, and M. W. Woolrich, "A general framework for the analysis of vessel encoded arterial spin labeling for vascular territory mapping," *Magn Reson Med*, vol. 64, pp. 1529–1539, 2010.

[75] M. A. Chappell, T. W. Okell, S. J. Payne, P. Jezzard, and M. W. Woolrich, "A fast analysis method for non-invasive imaging of blood flow in individual cerebral arteries using vessel-encoded arterial spin labelling angiography," *Medical Image Analysis*, vol. 16, no. 4, pp. 831–839, 2012.

[76] B. J. MacIntosh, E. Sideso, M. J. Donahue, M. A. Chappell, M. Gnther, A. Handa, J. Kennedy, and P. Jezzard, "Intracranial hemodynamics is altered by carotid artery disease and after endarterectomy: A dynamic magnetic resonance angiography study," *Stroke*, vol. 42, no. 4, pp. 979–984, 2011.

[77] T. J. Kaufmann and D. F. Kallmes, "Diagnostic cerebral angiography: archaic and complication-prone or here to stay for another 80 years?," *AJR Am J Roentgenol*, vol. 190, no. 6, pp. 1435–7, 2008.

[78] T. J. Kaufmann, J. Huston III, J. N. Mandrekar, C. D. Schleck, K. R. Thielen, and D. F. Kallmes, "Complications of diagnostic cerebral angiography: Evaluation of 19 826 consecutive patients," *Radiology*, vol. 243, pp. 812–819, 2007.

[79] M. M. Lell, K. Anders, M. Uder, E. Klotz, H. Ditt, F. Vega-Higuera, T. Boskamp, W. A. Bautz, and B. F. Tomandl, "New techniques in CT angiography," *RadioGraphics*, vol. 26, pp. S45–S62, 2006.

[80] T. J. Kaufmann and D. F. Kallmes, "Utility of MRA and CTA in the evaluation of carotid occlusive disease," *Seminars in Vascular Surgery*, vol. 18, no. 2, pp. 75–82, 2005.

[81] M. T. Karamessini, G. C. Kagadis, T. Petsas, D. Karnabatidis, D. Konstantinou, G. C. Sakellaropoulos, G. C. Nikiforidis, and D. Siablis, "CT angiography with three-dimensional techniques for the early diagnosis of intracranial aneurysms. comparison with intra-arterial DSA and the surgical findings," *European Journal of Radiology*, vol. 49, no. 3, pp. 212–223, 2004.

[82] I. R. van den Wijngaard, J. Boiten, G. Holswilder, A. Algra, D. W. J. Dippel, B. K. Velthuis, M. J. H. Wermer, and M. A. A. van Walderveen, "Impact of collateral status evaluated by dynamic computed tomographic angiography on clinical outcome in patients with ischemic stroke," *Stroke*, vol. 46, no. 12, pp. 3398–3404, 2015.

[83] N. Tomura, M. Hashimoto, R. Sashi, H. Hirano, M. Kobayashi, Y. Hirano, K. Satoh, J. Watarai, and M. Kowada, "Superselective angio-CT of brain tumors," *American Journal of Neuroradiology*, vol. 17, no. 6, pp. 1073–80, 1996.

[84] F. R. Korosec, R. Frayne, T. M. Grist, and C. A. Mistretta, "Time-resolved contrast-enhanced 3D MR angiography," *Magn Reson Med*, vol. 36, pp. 345–351, 1996.

[85] T. M. Grist, C. A. Mistretta, C. M. Strother, and P. A. Turski, "Time-resolved angiography: Past, present, and future," *J Magn Reson Imaging*, vol. 36, no. 6, pp. 1273–86, 2012.

[86] H. Zhang, J. H. Maki, and M. R. Prince, "3D contrast-enhanced MR angiography," *J Magn Reson Imaging*, vol. 25, no. 1, pp. 13–25, 2007.

[87] M. Miyazaki and V. S. Lee, "Nonenhanced MR angiography," *Radiology*, vol. 248, pp. 20–43, 2008.

[88] C. L. Dumoulin, S. P. Souza, M. F. Walker, and W. Wagle, "Three-dimensional phase contrast angiography," *Magn Reson Med*, vol. 9, pp. 139–149, 1989.

[89] T. Gu, F. R. Korosec, W. F. Block, S. B. Fain, Q. Turk, D. Lum, Y. Zhou, T. M. Grist, V. Haughton, and C. A. Mistretta, "PC VIPR: A high-speed 3D phase-contrast method for flow quantification and high-resolution angiography," *AJNR Am J Neurorad*, vol. 26, pp. 743–749, 2005.

[90] F. Sallustio, R. Kern, M. Gunther, K. Szabo, M. Griebe, S. Meairs, M. Hennerici, and A. Gass, "Assessment of intracranial collateral flow by using dynamic arterial spin labeling MRA and transcranial color-coded duplex ultrasound," *Stroke*, vol. 39, no. 6, pp. 1894–7, 2008.

[91] D. Kopeinigg and R. Bammer, "Time-resolved angiography using inflow subtraction (TRAILS)," *Magn Reson Med*, vol. 72, no. 3, pp. 669–78, 2014.

[92] X. Bi, P. Weale, P. Schmitt, S. Zuehlsdorff, and R. Jerecic, "Non-contrast-enhanced four-dimensional (4D) intracranial MR angiography: a feasibility study," *Magn Reson Med*, vol. 63, no. 3, pp. 835–41, 2010.

[93] L. Yan, S. Wang, Y. Zhuo, R. L. Wolf, M. F. Stiefel, J. An, Y. Ye, Q. Zhang, E. R. Melhem, and D. J. J. Wang, "Unenhanced dynamic MR angiography: High spatial and temporal resolution by using true FISP-based spin tagging with alternating radiofrequency," *Radiology*, vol. 256, no. 1, pp. 270–279, 2010.

[94] H. K. Song, L. Yan, R. X. Smith, Y. Xue, S. Rapacchi, S. Srinivasan, D. B. Ennis, P. Hu, N. Pouratian, and D. J. Wang, "Noncontrast enhanced four-dimensional dynamic MRA with golden angle radial acquisition and k-space weighted image contrast (KWIC) reconstruction," *Magn Reson Med*, vol. 72, no. 6, pp. 1541–51, 2014.

[95] H. Wu, W. F. Block, P. A. Turski, C. A. Mistretta, D. J. Rusinak, Y. Wu, and K. M. Johnson, "Noncontrast dynamic 3D intracranial MR angiography using pseudo-continuous arterial spin labeling (PCASL) and accelerated 3D radial acquisition," *J Magn Reson Imaging*, vol. 39, no. 5, pp. 1320–6, 2014.

[96] P. M. Robson, W. Dai, A. Shankaranarayanan, N. M. Rofsky, and D. C. Alsop, "Time-resolved vessel-selective digital subtraction MR angiography of the cerebral vasculature with arterial spin labeling," *Radiology*, vol. 257, pp. 507–515, 2010.

[97] T. Lindner, U. Jensen-Kondering, M. J. van Osch, O. Jansen, and M. Helle, "3D time-resolved vessel-selective angiography based on pseudo-continuous arterial spin labeling," *Magn Reson Imaging*, vol. 33, no. 6, pp. 840–6, 2015.

[98] M. J. P. van Osch, J. Hendrikse, X. Golay, C. J. G. Bakker, and J. van der Grond, "Non-invasive visualization of collateral blood flow patterns of the circle of willis by dynamic MR angiography," *Medical Image Analysis*, vol. 10, no. 1, pp. 59–70, 2006.

[99] M. Nakamura, M. Yoneyama, T. Tabuchi, A. Takemura, M. Obara, S. Tatsuno, and S. Sawano, "Vessel-selective, non-contrast enhanced, time-resolved mr angiography with vessel-selective arterial spin labeling technique (cinema-select) in intracranial arteries," *Radiol Phys Technol*, vol. 6, no. 2, pp. 327–34, 2013.

[100] T. W. Okell, P. Schmitt, X. Bi, M. A. Chappell, R. H. Tijssen, F. Sheerin, K. L. Miller, and P. Jezzard, "Optimization of 4D vessel-selective arterial spin labeling angiography using balanced steady-state free precession and vessel-encoding," *NMR Biomed*, 2016.

[101] L. Aldo Ferrara, M. Mancini, R. Iannuzzi, T. Marotta, I. Gaeta, F. Pasanisi, A. Postiglione, and L. Guida, "Carotid diameter and blood flow velocities in cerebral circulation in hypertensive patients," *Stroke*, vol. 26, pp. 418–421, 1995.

[102] G. J. Stanisz, E. E. Odrobina, J. Pun, M. Escaravage, S. J. Graham, M. J. Bronskill, and R. M. Henkelman, "T_1, T_2 relaxation and magnetization transfer in tissue at 3T," *Magn Reson Med*, vol. 54, no. 3, pp. 507–512, 2005.

[103] R. Bammer, T. A. Hope, M. Aksoy, and M. T. Alley, "Time-resolved 3D quantitative flow MRI of the major intracranial vessels: initial experience and comparative evaluation at 1.5T and 3.0T in combination with parallel imaging," *Magn Reson Med*, vol. 57, no. 1, pp. 127–40, 2007.

[104] Y. Zhang, M. Brady, and S. Smith, "Segmentation of brain MR images through a hidden Markov random field model and the expectation-maximization algorithm," *IEEE Trans Med Imag*, vol. 20(1), pp. 45–57, 2001.

[105] M. Jenkinson, P. Bannister, J. M. Brady, and S. M. Smith, "Improved optimisation for the robust and accurate linear registration and motion correction of brain images," *NeuroImage*, vol. 17(2), pp. 825–841, 2002.

[106] Y. Jung, E. C. Wong, and T. T. Liu, "Multiphase pseudocontinuous arterial spin labeling (MP-PCASL) for robust quantification of cerebral blood flow," *Magn Reson Med*, vol. 64, no. 3, pp. 799–810, 2010.

[107] D. D. Shin, T. T. Liu, E. C. Wong, A. Shankaranarayanan, and Y. Jung, "Pseudocontinuous arterial spin labeling with optimized tagging efficiency," *Magn Reson Med*, vol. 68, no. 4, pp. 1135–44, 2012.

[108] W. M. Luh, S. L. Talagala, T. Q. Li, and P. A. Bandettini, "Pseudo-continuous arterial spin labeling at 7 T for human brain: estimation and correction for off-resonance effects using a prescan," *Magn Reson Med*, vol. 69, no. 2, pp. 402–10, 2013.

[109] E. S. K. Berry, P. Jezzard, and T. W. Okell, "An optimized encoding scheme for planning vessel-encoded pseudocontinuous arterial spin labeling," *Magn Reson Med*, vol. 74, pp. 1248–1256, 2015.

[110] M. Jenkinson, C. F. Beckmann, T. E. J. Behrens, M. W. Woolrich, and S. M. Smith, "FSL," *NeuroImage*, vol. 62, no. 2, pp. 782–790, 2012.

[111] T. W. Okell, *Assessment of collateral blood flow in the brain using magnetic resonance imaging*. Thesis, University of Oxford, 2011.

[112] T. W. Okell, P. Schmitt, X. Bi, M. A. Chappell, R. H. Tijssen, K. L. Miller, and P. Jezzard, "4D vessel-encoded arterial spin labeling angiography," in *Proceedings of the 19th Annual Meeting of ISMRM*, p. 4034, 2011.

[113] J. A. Fessler, "Image Reconstruction Toolbox," 2002.

[114] M. L. Lauzon and B. K. Rutt, "Effects of polar sampling in k-space," *Magn Reson Med*, vol. 36, pp. 940–949, 1996.

[115] P. B. Roemer, W. A. Edelstein, C. E. Hayes, S. P. Souza, and O. M. Mueller, "The NMR phase array," *Magn Reson Med*, vol. 16, pp. 192–225, 1990.

[116] D. C. Peters, J. A. Derbyshire, and E. R. McVeigh, "Centering the projection reconstruction trajectory: reducing gradient delay errors," *Magn Reson Med*, vol. 50, no. 1, pp. 1–6, 2003.

[117] J. J. Sepkoski, "Quantified coefficients of association and measurement of similarity," *Journal of the International Association for Mathematical Geology*, vol. 6, no. 2, pp. 135–152, 1974.

[118] K. L. Miller, "Asymmetries of the balanced SSFP profile. part i: Theory and observation," *Magn Reson Med*, vol. 63, pp. 385–395, 2010.

[119] O. Bieri and K. Scheffler, "Flow compensation in balanced SSFP sequences," *Magnetic Resonance in Medicine*, vol. 54, no. 4, pp. 901–907, 2005.

[120] T. W. Okell, M. A. Chappell, U. G. Schulz, and P. Jezzard, "A kinetic model for vessel-encoded dynamic angiography with arterial spin labeling," *Magn Reson Med*, vol. 68, no. 3, pp. 969–979, 2012.

[121] M. Markl, M. T. Alley, C. J. Elkins, and N. J. Pelc, "Flow effects in balanced steady state free precession imaging," *Magn Reson Med*, vol. 50, no. 5, pp. 892–903, 2003.

[122] B. J. MacIntosh, N. Filippini, M. A. Chappell, M. W. Woolrich, C. E. Mackay, and P. Jezzard, "Assessment of arterial arrival times derived from multiple inversion time pulsed arterial spin labeling MRI," *Magn Reson Med*, vol. 63, no. 3, pp. 641–7, 2010.

[123] P. M. Robson, A. K. Grant, A. J. Madhuranthakam, R. Lattanzi, D. K. Sodickson, and C. A. McKenzie, "Comprehensive quantification of signal-to-noise ratio and g-factor for image-based and k-space-based parallel imaging reconstructions," *Magn Reson Med*, vol. 60, no. 4, pp. 895–907, 2008.

[124] C. Kirbas and F. Quek, "A review of vessel extraction techniques and algorithms," *ACM Comput. Surv.*, vol. 36, no. 2, pp. 81–121, 2004.

[125] E. A. Rakhmanov, E. B. Saff, and Y. M. Zhou, "Minimal discrete energy on the sphere," *Mathematical Research Letters*, vol. 1, pp. 647–662, 1994.

[126] A. V. Barger, W. F. Block, Y. Toropov, T. M. Grist, and C. A. Mistretta, "Time-resolved contrast-enhanced imaging with isotropic resolution and broad coverage using an undersampled 3D projection trajectory," *Magn Reson Med*, vol. 48, no. 2, pp. 297–305, 2002.

[127] S. M. Smith, "Fast robust automated brain extraction," *Hum Brain Mapp*, vol. 17, no. 3, pp. 143–55, 2002.

[128] G. B. Chavhan, P. S. Babyn, B. G. Jankharia, H. M. Cheng, and M. M. Shroff, "Steady-state MR imaging sequences: Physics, classification, and clinical applications," *RadioGraphics*, vol. 28, pp. 1147–1160, 2008.

[129] B. Battal, M. Kocaoglu, N. Bulakbasi, G. Husmen, H. Tuba Sanal, and C. Tayfun, "Cerebrospinal fluid flow imaging by using phase-contrast MR technique," *Br J Radiol*, vol. 84, no. 1004, pp. 758–65, 2011.

[130] T. Cukur, M. Lustig, and D. G. Nishimura, "Improving non-contrast-enhanced steady-state free precession angiography with compressed sensing," *Magn Reson Med*, vol. 61, no. 5, pp. 1122–31, 2009.

[131] M. Lustig, D. Donoho, and J. M. Pauly, "Sparse MRI: The application of compressed sensing for rapid MR imaging," *Magn Reson Med*, vol. 58, no. 6, pp. 1182–95, 2007.